

**Scoping Estimates
of the
LDEF Satellite Induced Radioactivity**



by
T. W. Armstrong
B. L. Colborn

Work Performed for
NASA Marshall Space Flight Center
Space Science Laboratory, Astrophysics Division
Huntsville, AL.

Contract No. NAS8 - 38427

September 1990

Route 2, Prospect, Tennessee 38477

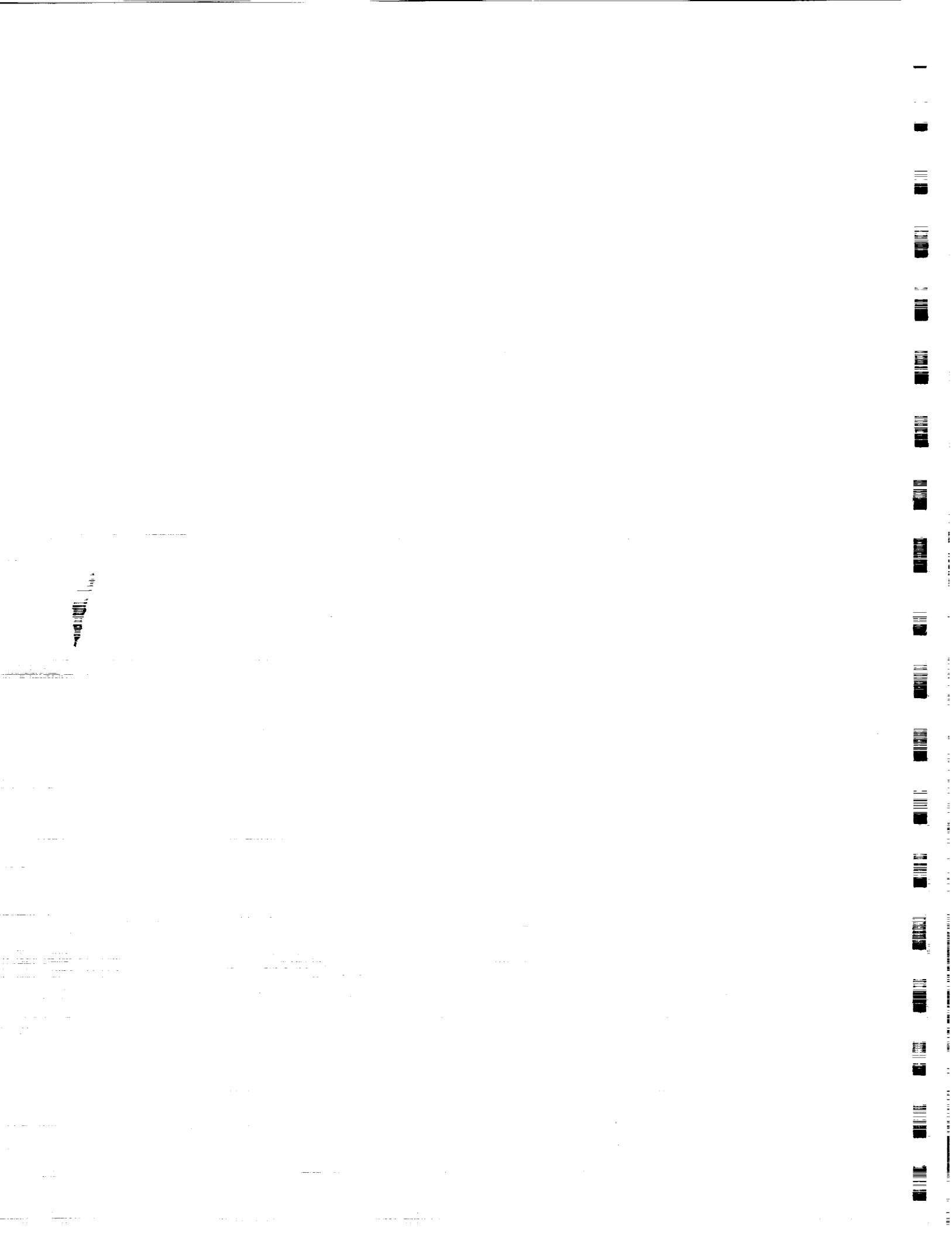
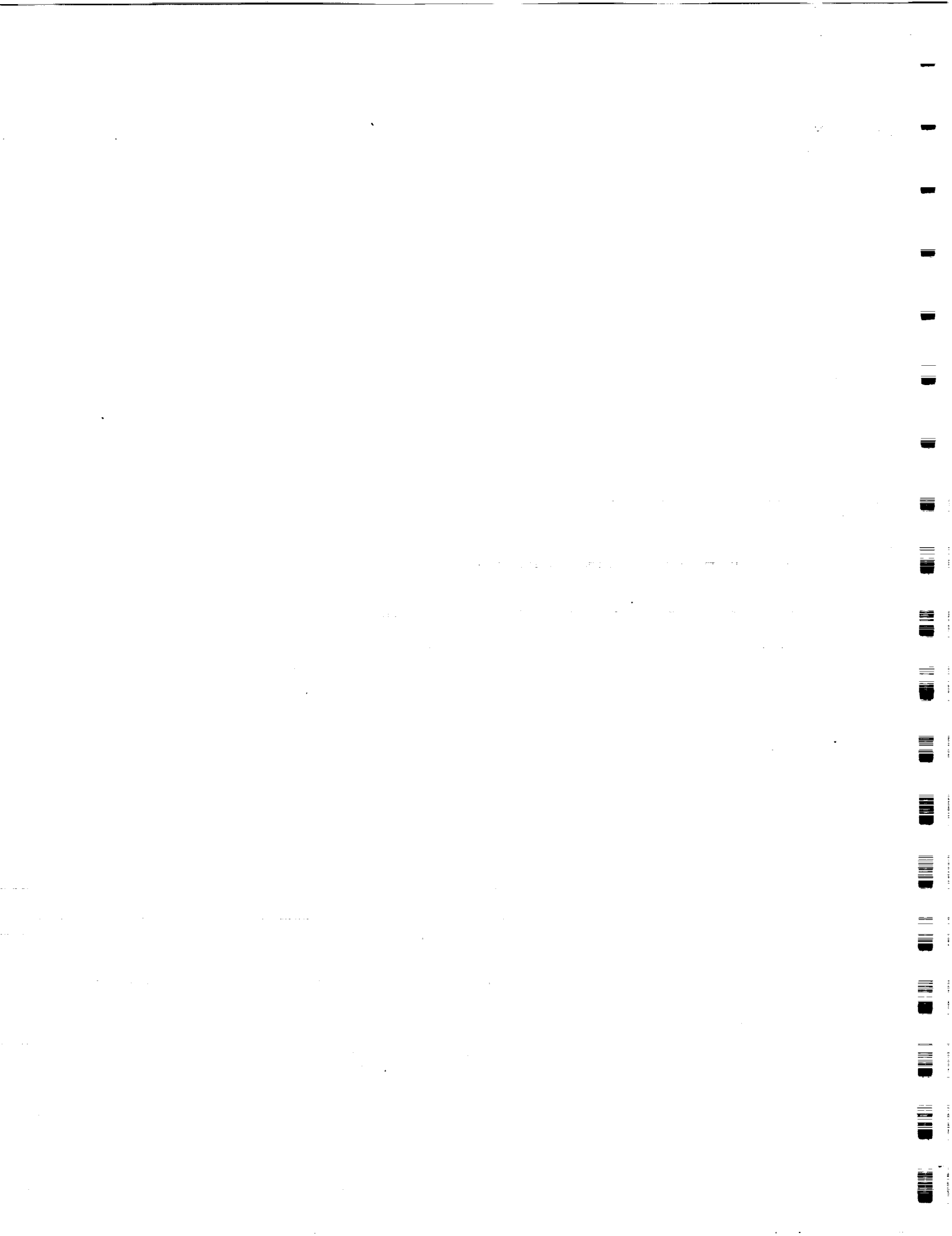


Table of Contents

1. Introduction.....	1
2. Calculational Method.....	6
3. Results of Transport Calculations	12
4. Approximate Estimate of Activation Anisotropy and Comparison with LDEF Data	18
5. References.....	22
Appendix A Sources of LDEF Ionizing Radiation Exposure	
Appendix B Dose Response Functions	
Appendix C Activation Cross Sections	
Appendix D Additional Fluence Results	
Appendix E Additional Dose Results	
Appendix F Results for Radioisotope Production from Stainless Steel	



1. Introduction

The Long Duration Exposure Facility (LDEF) satellite was recovered in January 1990 after almost six years in space. LDEF was well-instrumented with ionizing radiation dosimeters, including thermoluminescent dosimeters (TLD's), plastic nuclear track detectors (PNTD's), and a variety of metal foil samples for measuring nuclear activation products.¹ In addition, the induced radioactivity produced in various spacecraft components provides information on the radiation exposure.² Analysis of these LDEF data by several groups is in progress under coordination of the LDEF Ionizing Radiation Special Investigation Group.³

The extensive LDEF radiation measurements (Fig. 1) provide the type of radiation environments and effects data needed to evaluate and help resolve uncertainties in present ionizing radiation models and calculational methods (Fig. 2). The LDEF data are particularly important to improving models for addressing radiation issues associated with Space Station Freedom since LDEF had the same altitude range ($\approx 350 - 500$) and orbit inclination (28.5°) as planned for the Space Station. In conjunction with the LDEF data analysis, a calculational program has been established at the NASA MSFC to provide calculational support to aid in LDEF data interpretation and to utilize LDEF data for assessing the accuracy of current models. A summary of the calculational approach is given in Fig. 3. The present report describes some initial results from this LDEF calculational study.

The purpose of the calculations reported here is to provide some initial results to aid in the LDEF data interpretation -- namely, to obtain a general indication of: (a) the importance of different space radiation sources (trapped protons, galactic protons, albedo protons, and albedo neutrons), (b) the importance of secondary particles, and (c) the spatial dependence of the radiation environments and effects expected within the spacecraft. These are only scoping estimates because several important approximations have been made in this initial work -- e.g., a one-dimensional (aluminum slab) model of the LDEF spacecraft is used, and the angular variation of the incident radiation (particularly the trapped proton anisotropy) is not accurately simulated. Subsequent calculations are planned which will remove these approximations.

The calculational method (described in Sec. 2) uses the High Energy Transport Code (HETC)⁴ to estimate the importance of different sources and secondary particles in terms

Fig. 1. Ionizing radiation measurements aboard the LDEF satellite.

Radiation Quantity	Dosimeters Employed
Total Absorbed Dose	TLD's(a)
Dose in Microscopic Volumes	Microspheres
LET Spectra	PNTD(b)
Neutron Fluence & Spectra	Fission Foils, Activation(c)
Heavy Ion Fluence & Spectra	PNTD
Proton Fluence & Spectra	PNTD, Activation(c)
Trapped Proton Directionality	TLD's, Activation(c)

(a) Thermoluminescent Dosimeters

(b) Passive Nuclear Track Detectors

(c) Activation materials include specific metal samples for activation measurements (e.g., Ni, Co, V, Ta) and selected spacecraft components (e.g., Al structure, stainless steel trunions)

Unique Features of LDEF Mission	Importance to Ionizing Radiation Data Collection	Importance to Model/Code Validation	Importance to Future LEO Missions
<ul style="list-style-type: none"> • Well-instrumented for ionizing radiation measurements 	<ul style="list-style-type: none"> • Extensive radiation dosimetry - 6 different types of dosimetry provide data on numerous radiation effects <ul style="list-style-type: none"> - multiple dosimeters of each type (e.g., ~ 200 TLD's, > 500 PNDT's, > 400 activation samples) provide high-confidence in measurement results - multiple dosimetry locations (in 16 different experimental trays) provide results vs. shielding thickness 	<ul style="list-style-type: none"> • Data sufficiently extensive and detailed for definitive model uncertainty assessments - e.g.: <ul style="list-style-type: none"> - absorbed dose - proton and heavy ion fluence - energy spectra - LET spectra - secondary neutron fluence and spectra 	<ul style="list-style-type: none"> • Allows benchmarking and improvements of predictive methods for addressing ionizing radiation issues - e.g.: <ul style="list-style-type: none"> - crew dose - electronics upset - materials damage - backgrounds to sensitive instrumentation
<ul style="list-style-type: none"> • Long mission duration 	<ul style="list-style-type: none"> • High statistical accuracy of dosimetry results 	<ul style="list-style-type: none"> • Unprecedented accuracy of data for checking model predictions of high-LET radiation from high-Z cosmic rays and nuclear recoils 	<ul style="list-style-type: none"> • High-LET radiation component of key importance in assessing "single-hit" phenomena: <ul style="list-style-type: none"> - biological damage - Single-Event-Upsets to electronics - sensor noise
<ul style="list-style-type: none"> • Fixed orientation (<1° wobble during mission) 	<ul style="list-style-type: none"> • Allows measurement of trapped proton anisotropy 	<ul style="list-style-type: none"> • Unprecedented data for testing recently-developed MSFC model of trapped proton anisotropy 	<ul style="list-style-type: none"> • Trapped proton anisotropy important consideration for LEO, fixed orientation spacecraft (such as Space Station Freedom) with potential impact on: <ul style="list-style-type: none"> - best location for workstations, experimental packages, etc. - placement/design of radiation monitors - utilization of on-board mass to counteract anisotropy effects

Fig. 2. Significance of LDEF satellite data for validation of ionizing radiation models and predictive methods.

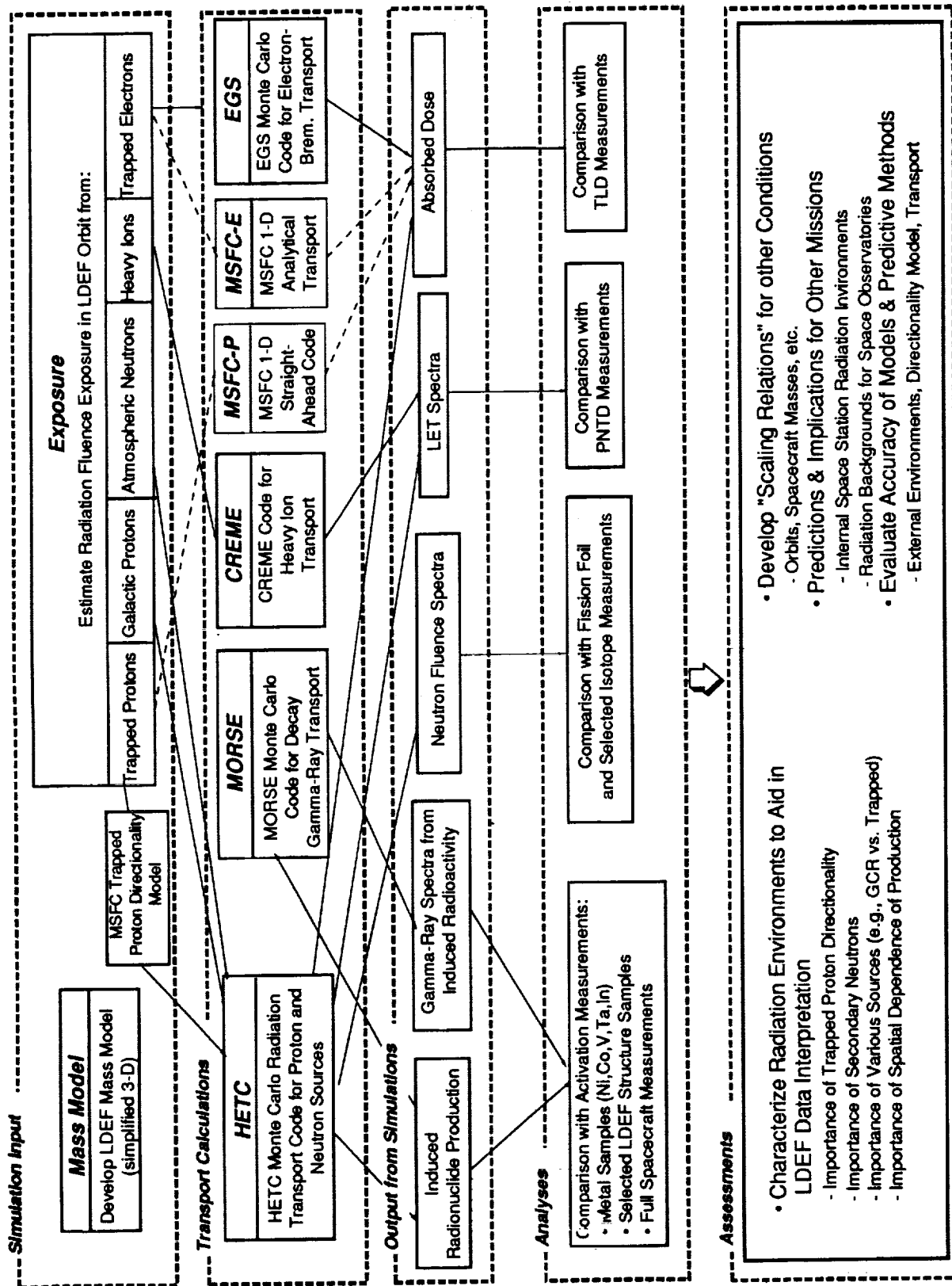
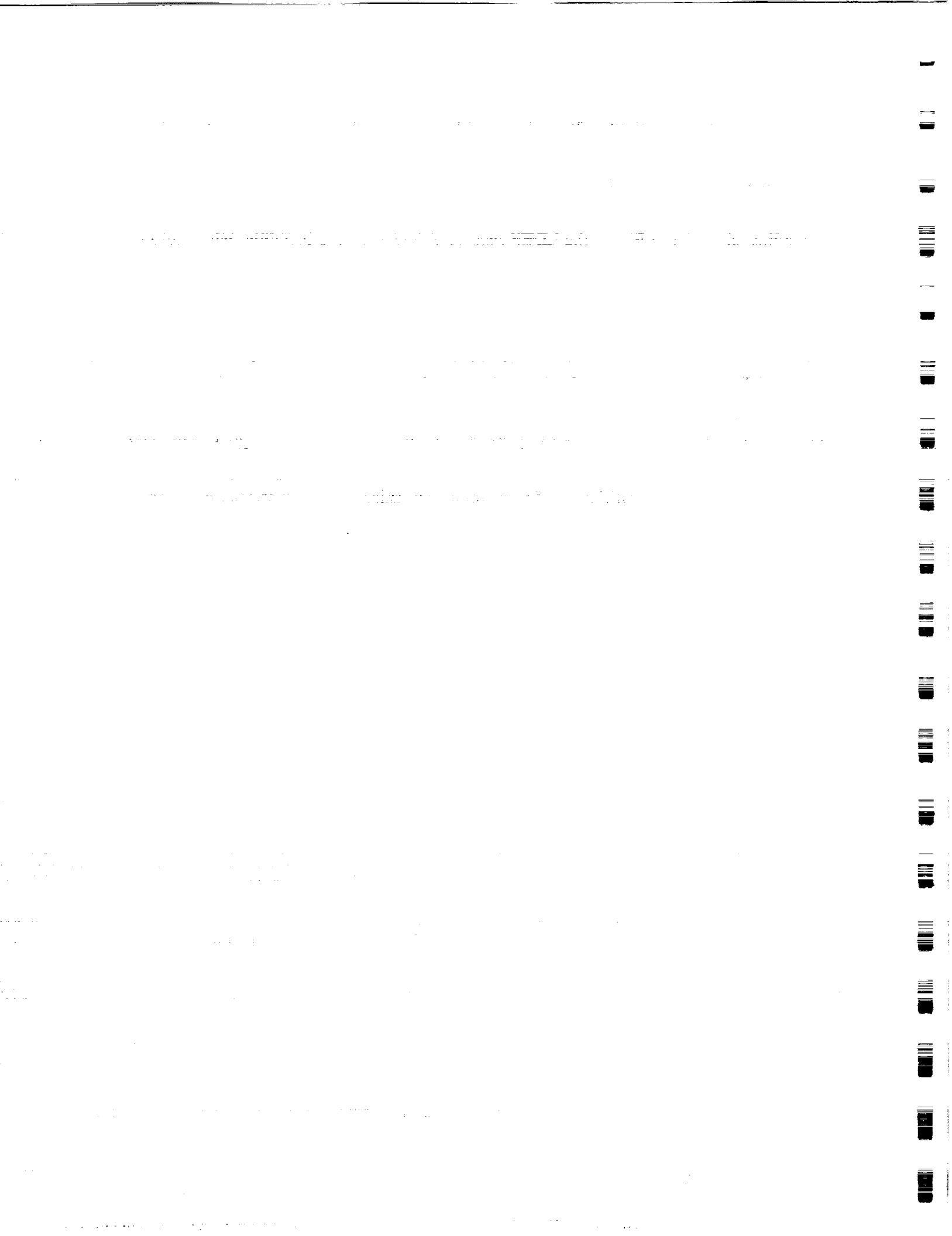


Fig. 3. Approach for calculational program in support of LDEF satellite ionizing radiation assessments.

of fluence, absorbed dose in tissue and silicon, and induced radioactivity as a function of depth in aluminum. Radioisotope production from aluminum and stainless steel is computed for varying aluminum shielding thicknesses. Results from these transport calculations are given in Sec. 3.

As indicated earlier in Fig. 2, the LDEF spacecraft had a fixed orientation, which allows measurement of the trapped proton anisotropy in the South Atlantic Anomaly region because the anisotropy is not "averaged out" by spacecraft motion as is usually the case. A model describing this anisotropy has been developed recently by Watts, et al. at MSFC.⁵ LDEF data should enable a definitive test of the model, and detailed transport calculations using a 3-D spacecraft model and anisotropic trapped proton spectra are planned to compare with the LDEF data. However, the induced radioactivity very near the spacecraft surface should be relatively insensitive to spacecraft geometry, and some approximate 1-D calculations have been made of the anisotropy of near-surface activation and comparisons made with preliminary LDEF data. These preliminary anisotropy comparisons are given in Sec. 4.



2. Calculational Method

Radiation transport calculations have been performed to obtain scoping estimates of the depth dependence of fluence, dose, and induced radioactivity produced in the LDEF spacecraft due to ionizing radiation exposure.

The radiation sources considered are trapped (Van Allen belt) protons, galactic protons, and "albedo" neutrons and protons emanating from the earth's atmosphere due to cosmic ray bombardment. The source spectra used as input for the transport calculations are shown in Fig. 4, and the procedure used in estimating these spectra is described in Appendix A. (The trapped electron spectrum is shown in Fig. 4 for comparison only. Since the trapped electrons are of low energy and produce effects very near the spacecraft surface, they are not considered in the transport calculations here.)

Spectra for the different sources were assumed incident isotropically on one side of a slab of aluminum 100 g/cm² in thickness. This is, of course, an important approximation, not only because it neglects the 3-D shielding effects of the spacecraft but also because the actual angular distribution of the incident radiation is very different for the different sources, as illustrated in Fig. 5.

The transport calculations were carried out using the SAIC version⁶ of the HETC code.⁴ This code uses Monte Carlo methods to obtain a detailed simulation of the radiation transport (Fig. 6). At each nuclear collision during the transport process, a calculation of particle transport inside the nucleus is performed using a high-energy intranuclear-cascade-evaporation (ICE) model⁷ to obtain the multiplicity, direction, and energy of all secondary particles (Fig. 7). For low-energy neutron (< 20 MeV) transport the high-energy ICE model is not applicable, but various experimental data libraries and transport codes are available in this low-energy region. For the calculations here, the low energy neutron source computed by HETC is coupled to the MORSE Monte Carlo⁸ code for low-energy neutron transport (Fig. 8).

The main output obtained from the transport calculations is depth-dependent fluence spectra. These spectra are folded with the response functions given in Appendix B to estimate the absorbed dose in tissue and silicon as a function of aluminum shielding thickness. While HETC provides radionuclide production directly as a natural outcome of

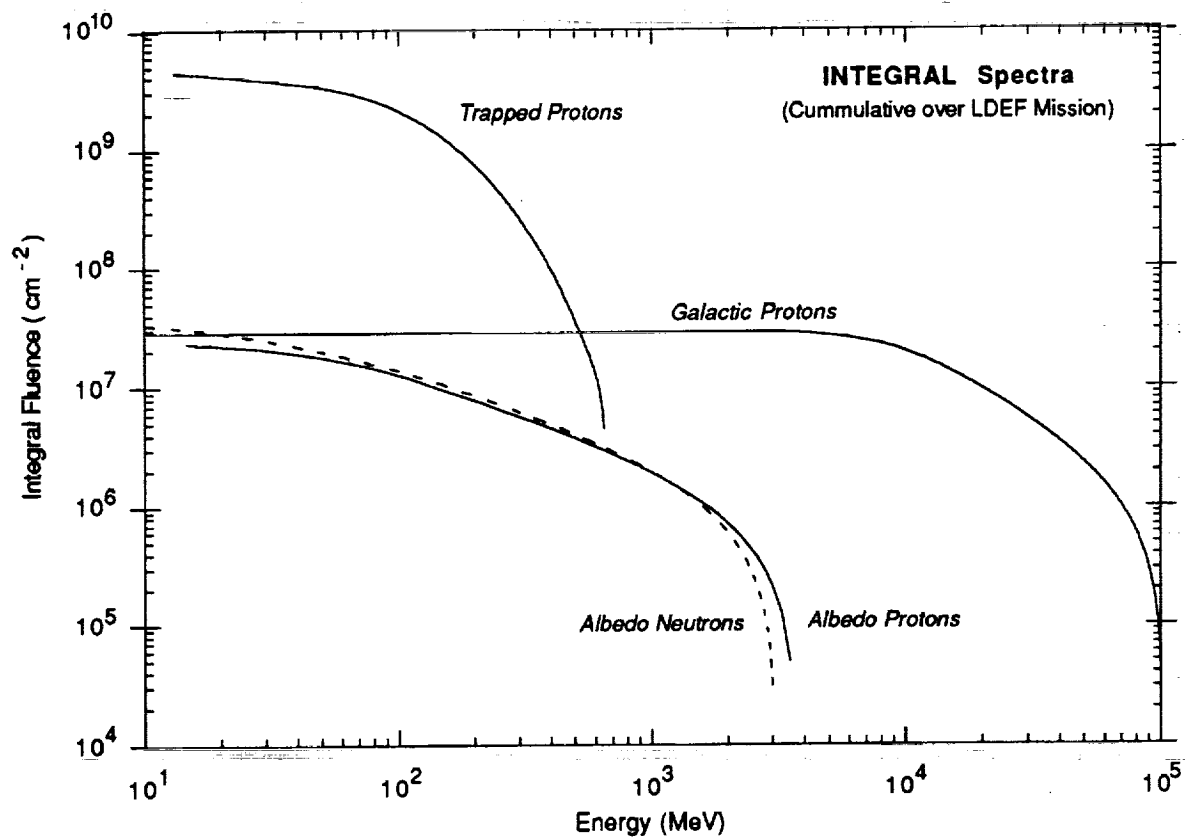
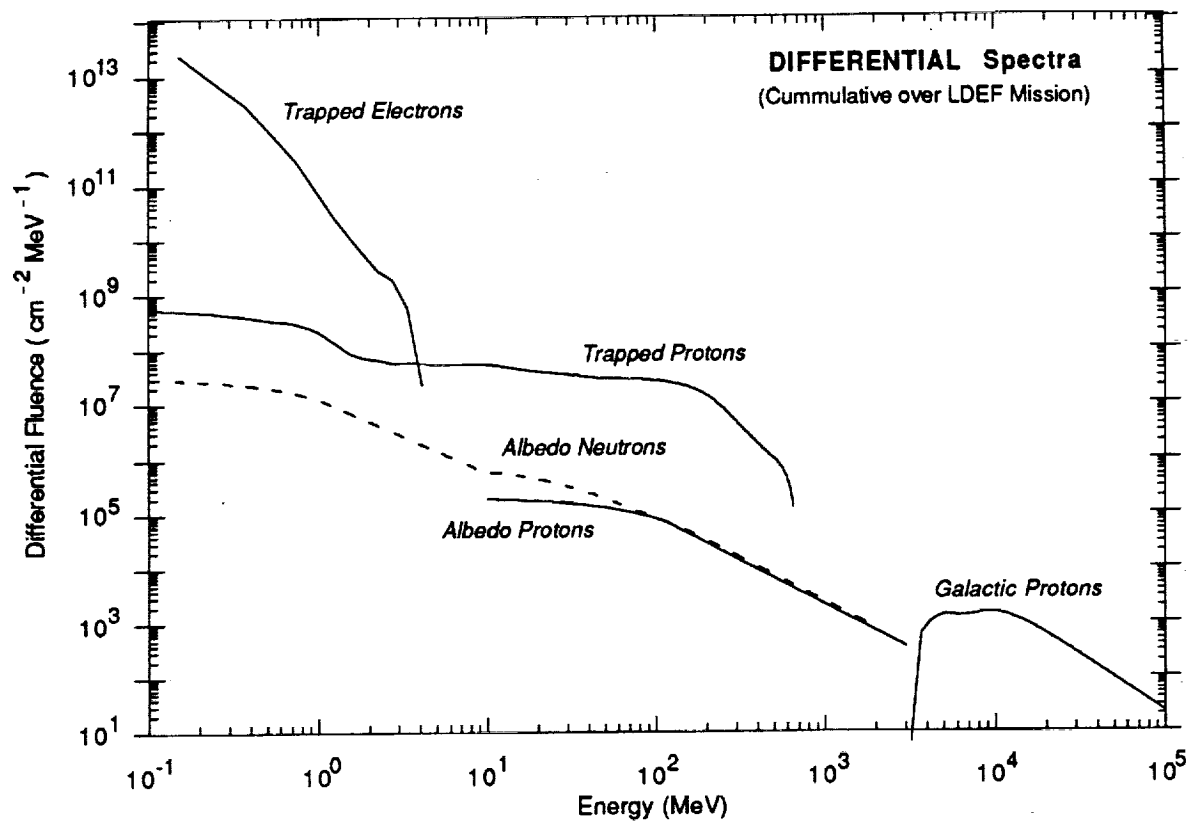


Fig. 4. LDEF exposure to ionizing radiation. Shown are cumulative, orbit-average differential and integral fluence spectra over the 5.8 yr. duration of the LDEF mission.

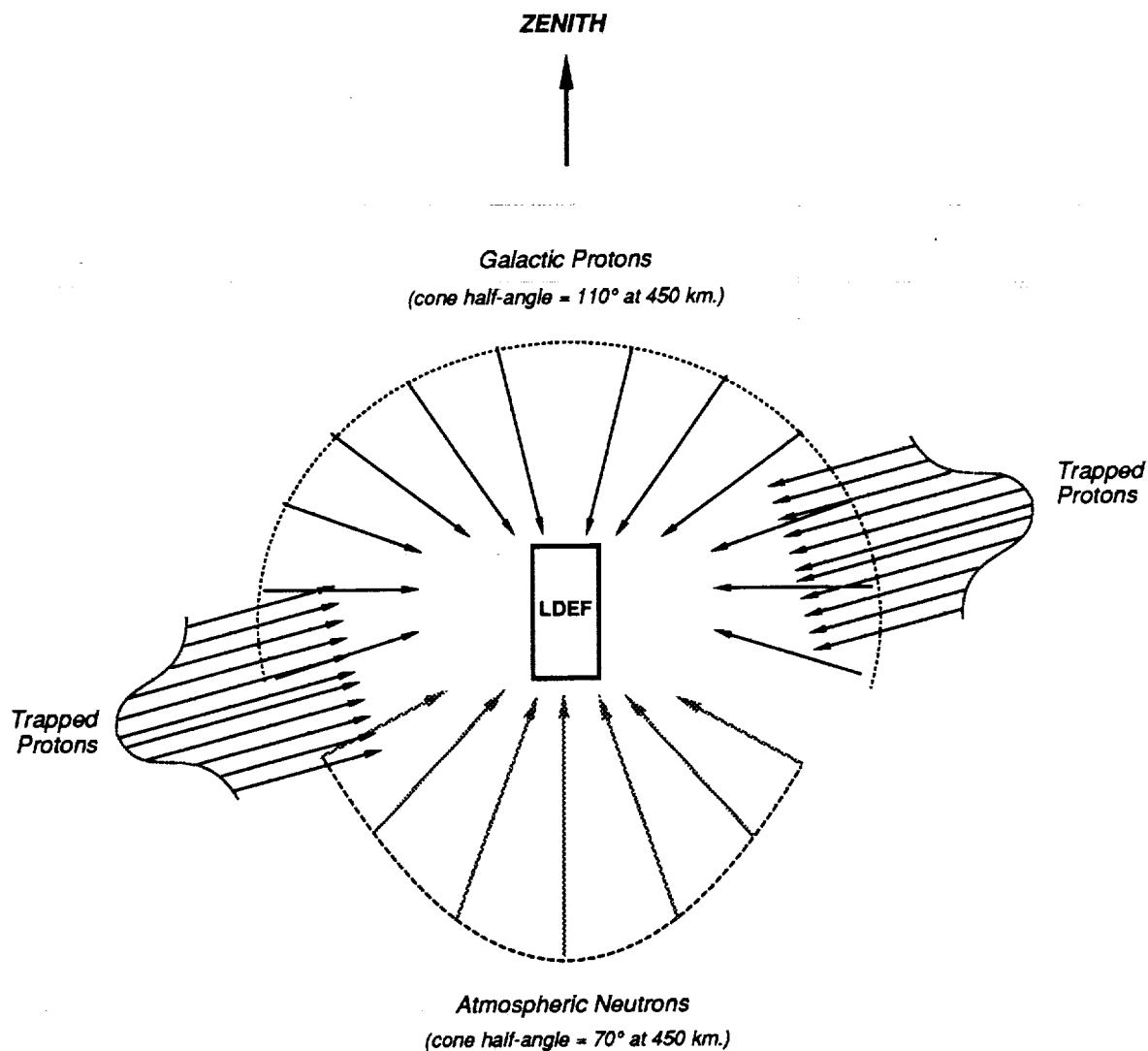


Fig. 5. Illustration of the nonuniform angular variation of LDEF exposure to ionizing radiation. Trapped proton exposure occurs in the South Atlantic Anomaly region where the flux is highly anisotropic at LDEF altitudes, with protons confined mainly in planes perpendicular to magnetic field lines and with in-plane asymmetry due to the East-West effect. Galactic protons are blocked out from below by the shielding effect of the earth. The angular distribution of albedo neutrons emanating from the earth's atmosphere is also geometrically constrained due to earth shielding.

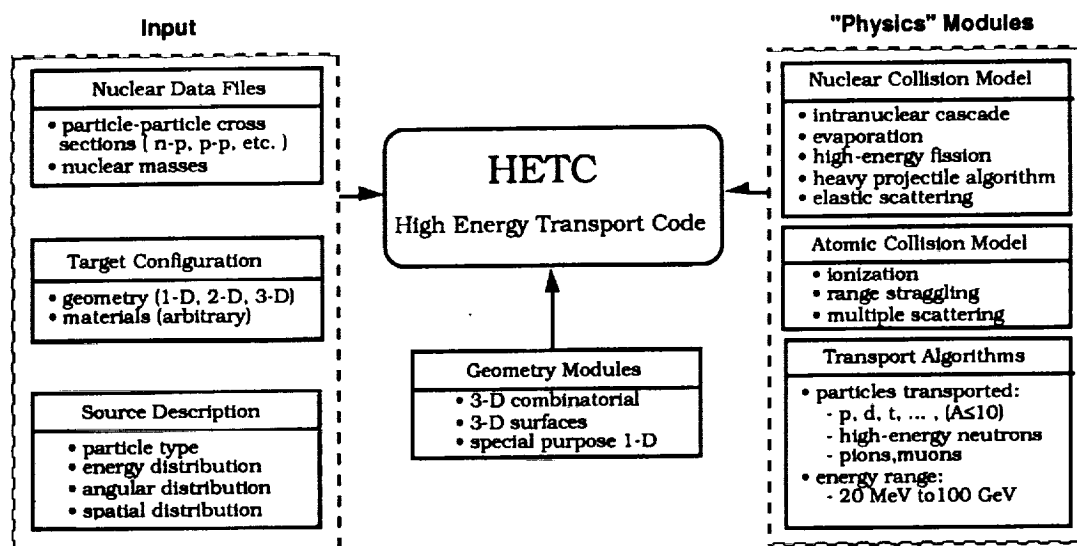


Fig. 6. Overview of the High Energy Transport Code (HETC).

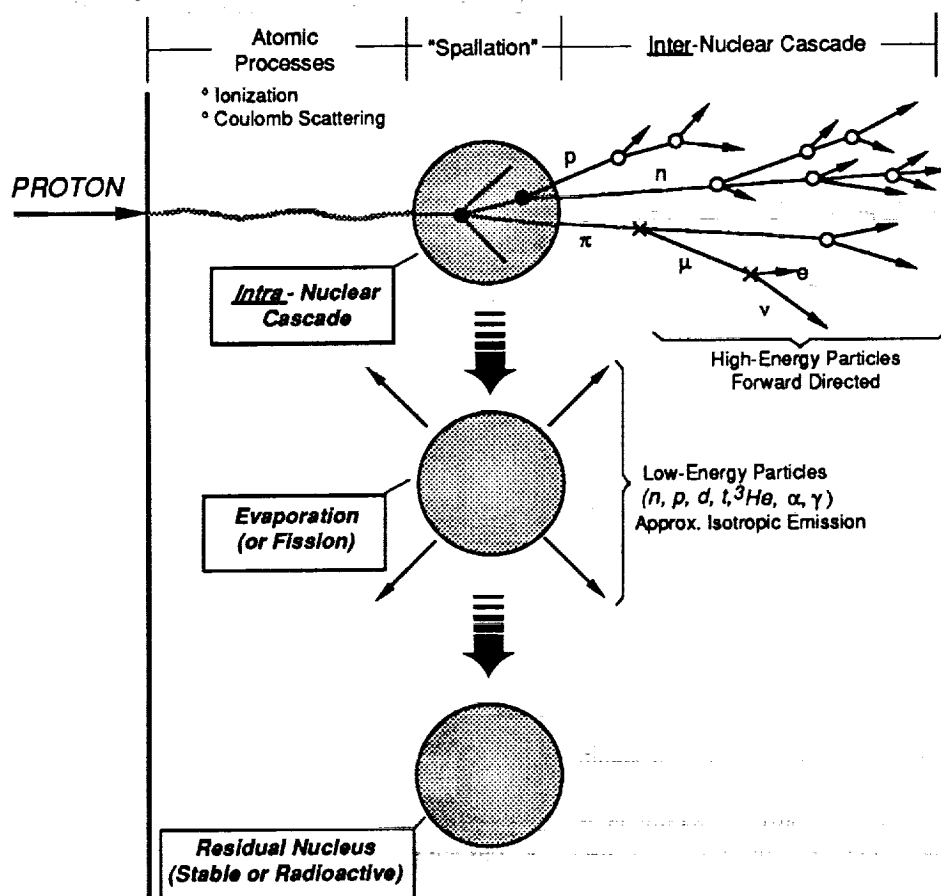


Fig. 7. Illustration of the two-step intranuclear-cascade-evaporation model used in the HETC transport code for computing secondary particles from high-energy ("spallation") nuclear collisions.

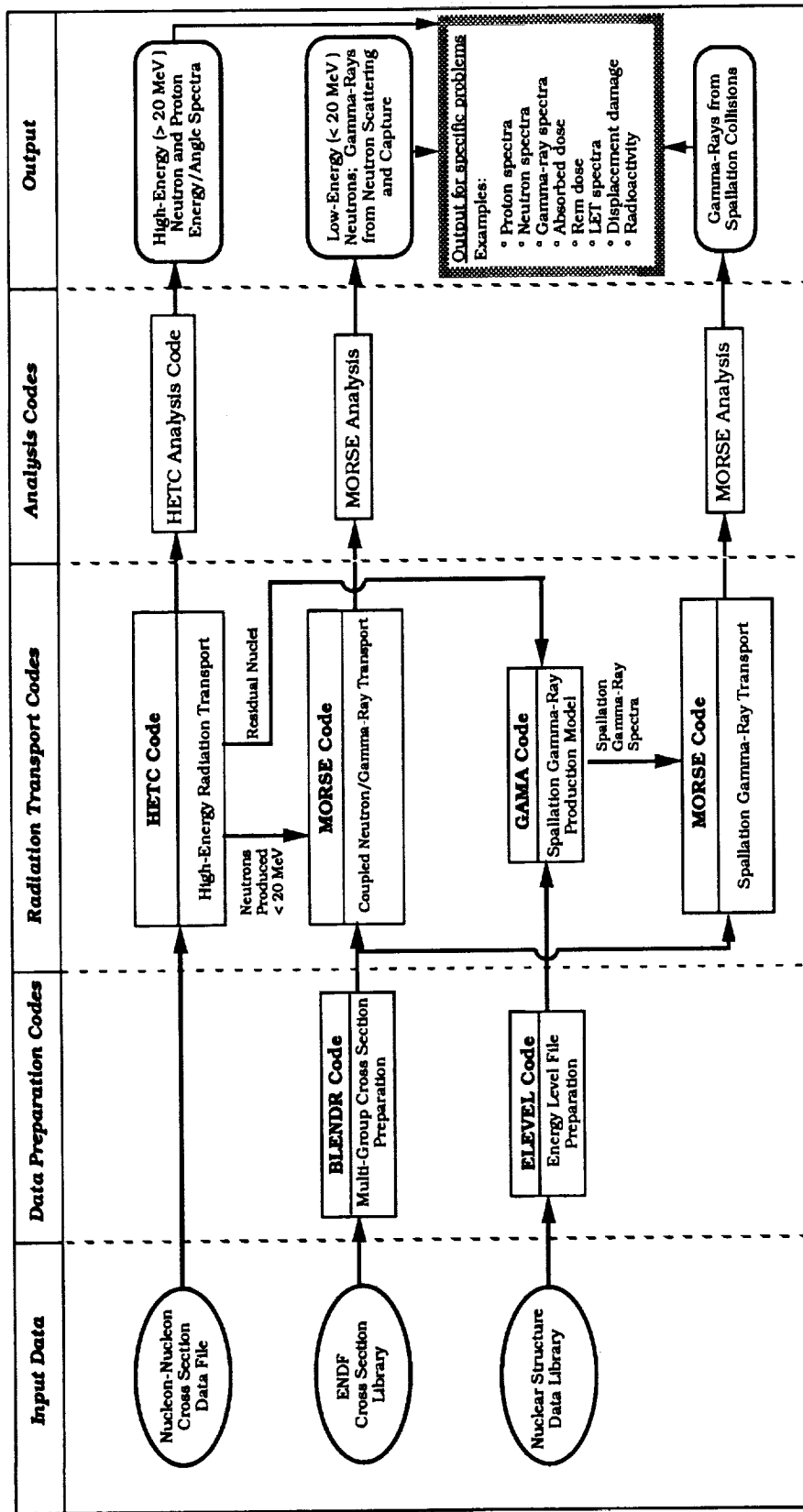


Fig. 8. SAIC version of the HETC code system, which includes high-energy proton and neutron transport, low-energy neutron transport, and gamma-ray transport.

the ICE model calculation, the statistical accuracy is generally poor when the product nucleus mass is far removed from the target nuclear mass. Since large target-product mass differences are of interest in the present problem (e.g., ^7Be from Fe in stainless steel), we have used an alternate procedure in which the HETC (and MORSE) computed fluence spectra are folded with available activation cross sections to estimate radionuclide production. Radioisotope production from aluminum and stainless steel were calculated using the cross sections given in Appendix C.

3. Results of Transport Calculations

Results from the transport calculations are arranged to show the contributions of different radiation sources and the contribution of secondary particles in terms of various effects. A summary of the results are given in this section, with additional results given in Appendixes D-F. The table below is a guide to the location of various results in the report.

	<u>Fluence</u>	<u>Fluence Spectra</u>	<u>Tissue Dose</u>	<u>Silicon Dose</u>	<u>Aluminum Activation</u>	<u>S. Steel Activation</u>
• Radiation Source Contribution	Fig. 9	App. D	Fig. 10	Fig. 10	Fig. 11	App. F
• Secondary Particle Contribution	App. D	App. D	App. E	--	Fig. 12	App. F

The spatial dependence of the results are in terms of the areal density depth in aluminum from 0 to 100 g/cm². To roughly relate these thicknesses to LDEF, the spacecraft diameter is 32 g/cm², and the length is 68 g/cm². (This is based on an average density obtained from the overall dimensions of 14 ft. diameter x 30 ft. long, a spacecraft structure weight of 8,000 lb., and a weight of 13,400 lb. for the experiments¹.)

Fluence

Figure 9 compares the proton and neutron fluences (over all energies) for all sources. For the trapped proton environment, the fluence from secondary neutrons exceed the proton fluence for penetration depths ≥ 10 g/cm². The magnitude, and spatial dependence, of secondary neutrons from galactic protons is comparable to the secondary neutrons from trapped protons.

Dose

Figure 10 compares the importance of different sources in terms of the absorbed dose in tissue and in silicon. The trapped proton source dominates for penetration depths ≤ 50 g/cm². The albedo sources contribute at most a few percent. Additional results for secondary particle contributions to the absorbed dose are given in Appendix E.

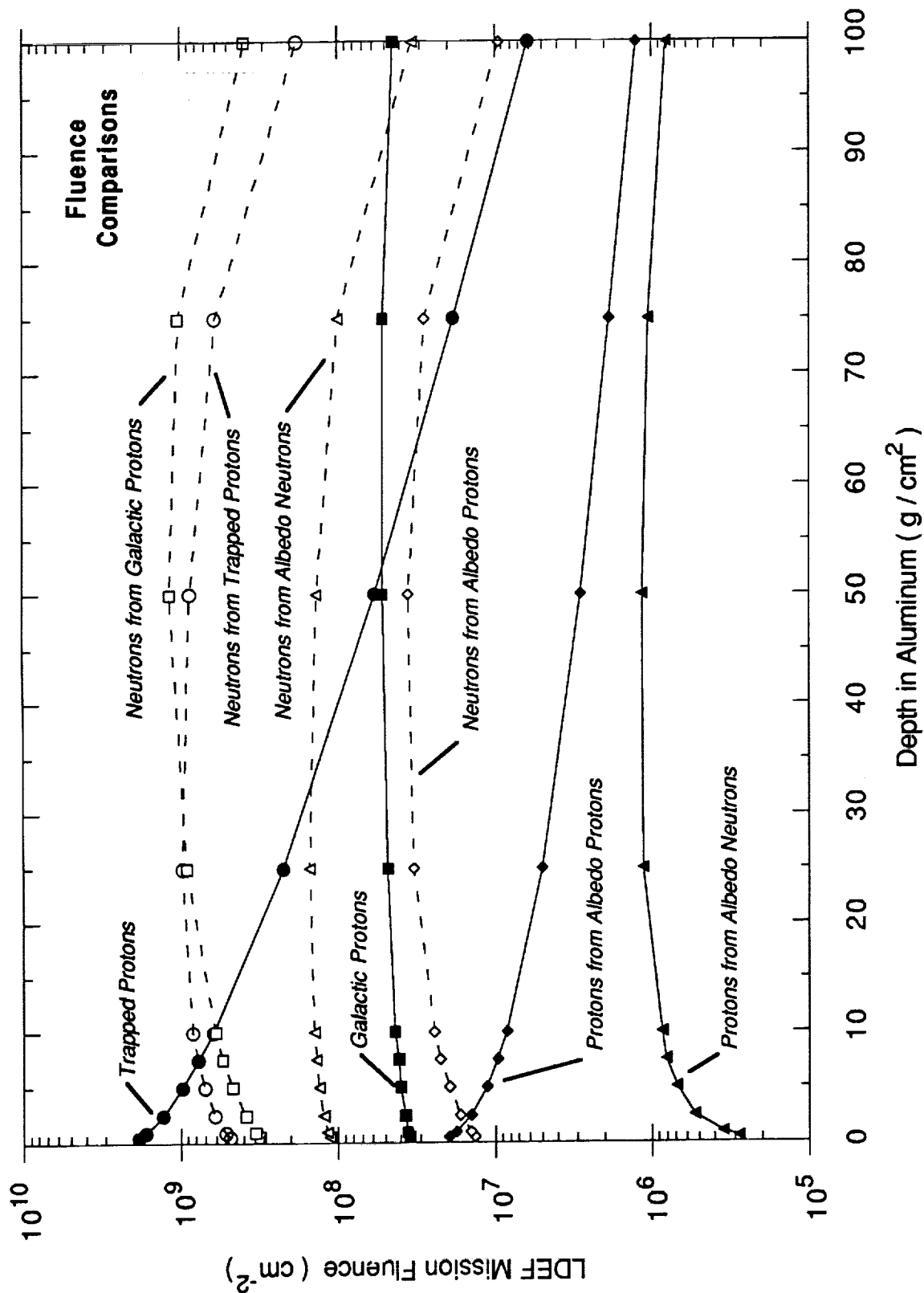


Fig. 9. Depth dependence of proton (primary and secondary proton contributions) and neutron fluences over all energies produced by trapped proton, galactic proton, albedo proton, and albedo neutron environments during the LDEF mission time. The different environments are all assumed incident isotropically on one side (0 depth) of an aluminum slab 100 g/cm² in thickness.

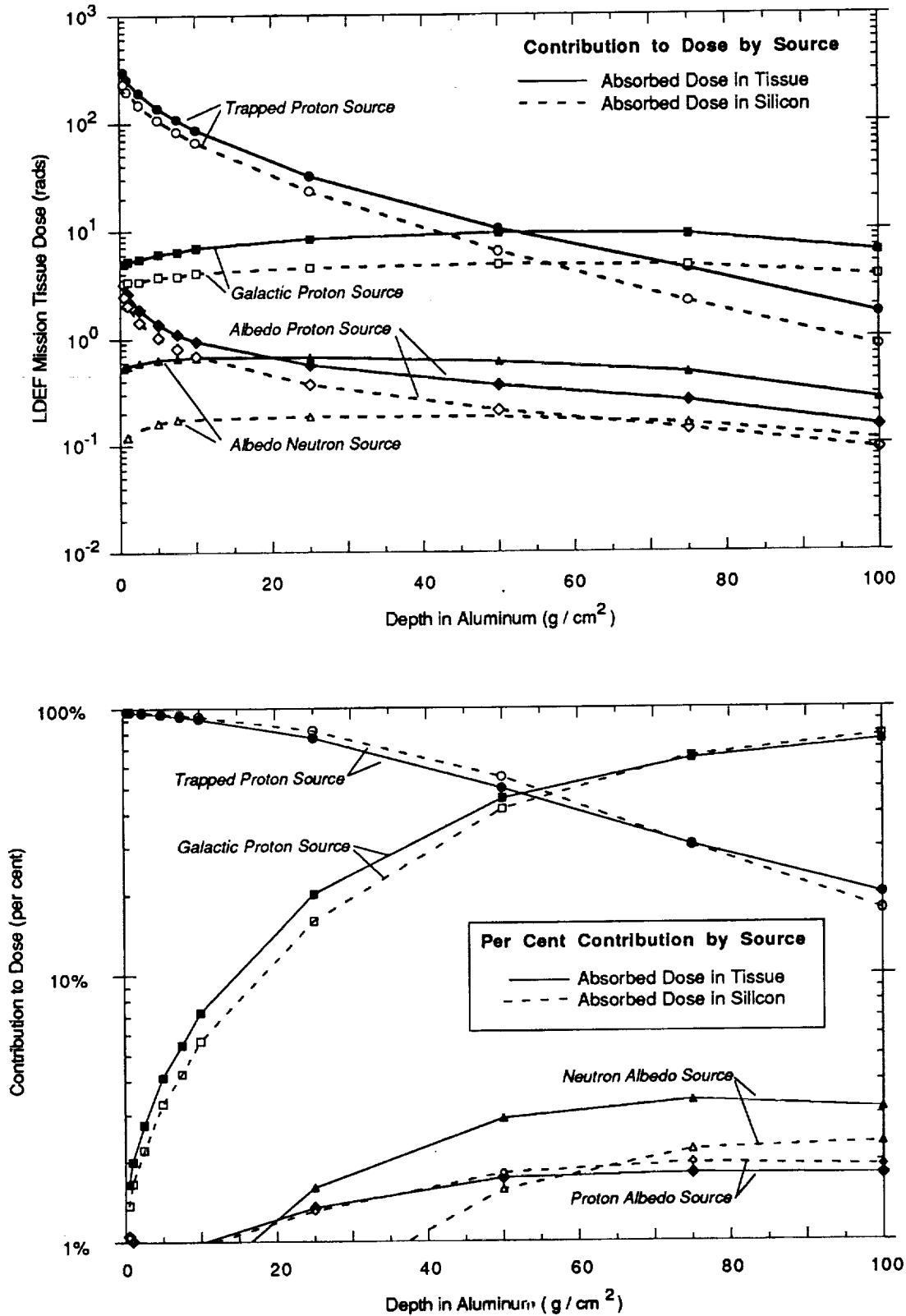


Fig. 10. Importance of various radiation sources in terms of absorbed dose in tissue and silicon for the total dose over the duration of the LDEF mission (top graph) and as a per cent of the total dose at each depth from all sources (bottom graph).

Activation

Figure 11 compares the contribution of different sources to ^{22}Na and to ^7Be production from aluminum. The galactic source contribution exceeds the trapped source contribution for depths $\geq 50 \text{ g/cm}^2$ for ^{22}Na production and $\geq 25 \text{ g/cm}^2$ for ^7Be production. The relative importance of the galactic source, which has a harder spectrum, is expected to be higher for the higher threshold activation products, which is consistent with these ^7Be vs. ^{22}Na results. Figure 12 shows that for the trapped proton source and the case of ^{22}Na production the secondary neutron contribution becomes important at depths $\geq 30 \text{ g/cm}^2$.

Results from calculations of radioisotope production in stainless steel are given in Appendix F.

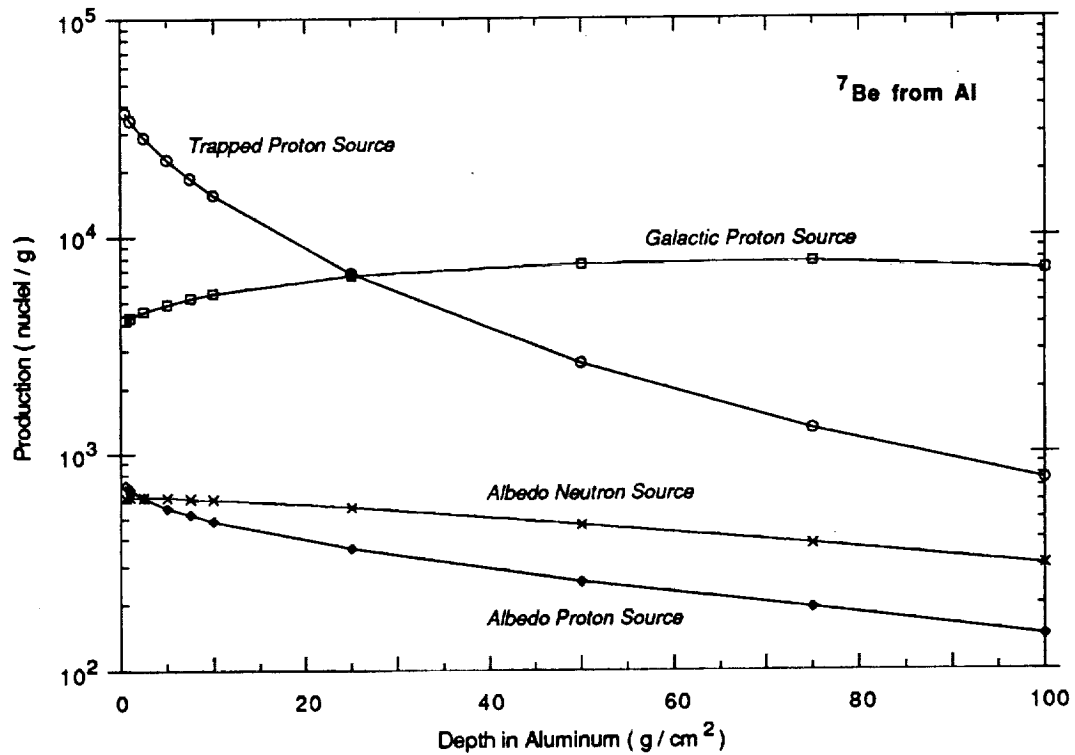
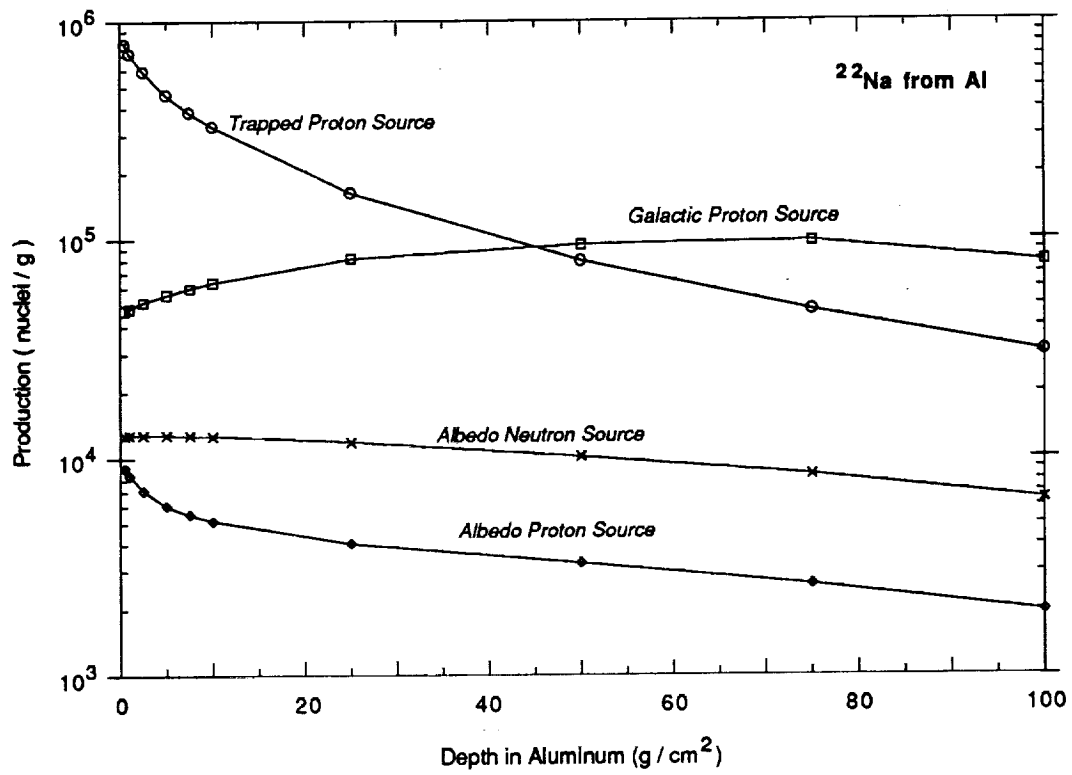


Fig. 11. Importance of different sources in terms of ^{22}Na and ^7Be production from aluminum. The production is normalized for the total lifetime of the LDEF mission.

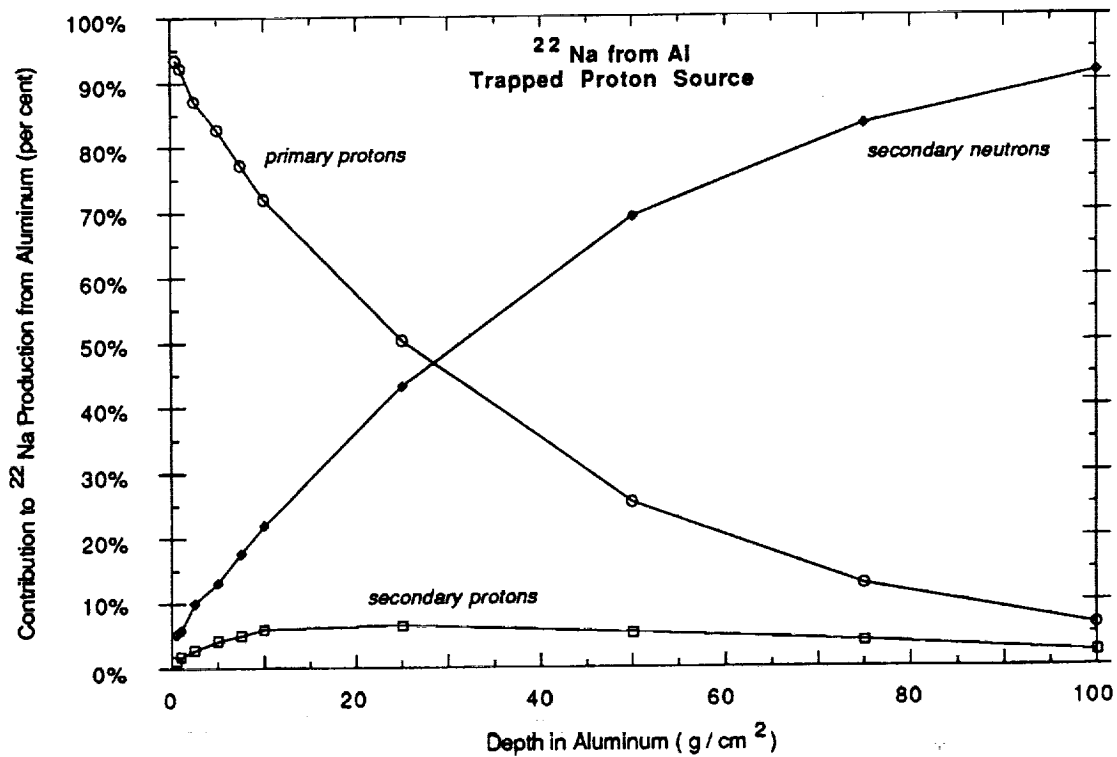
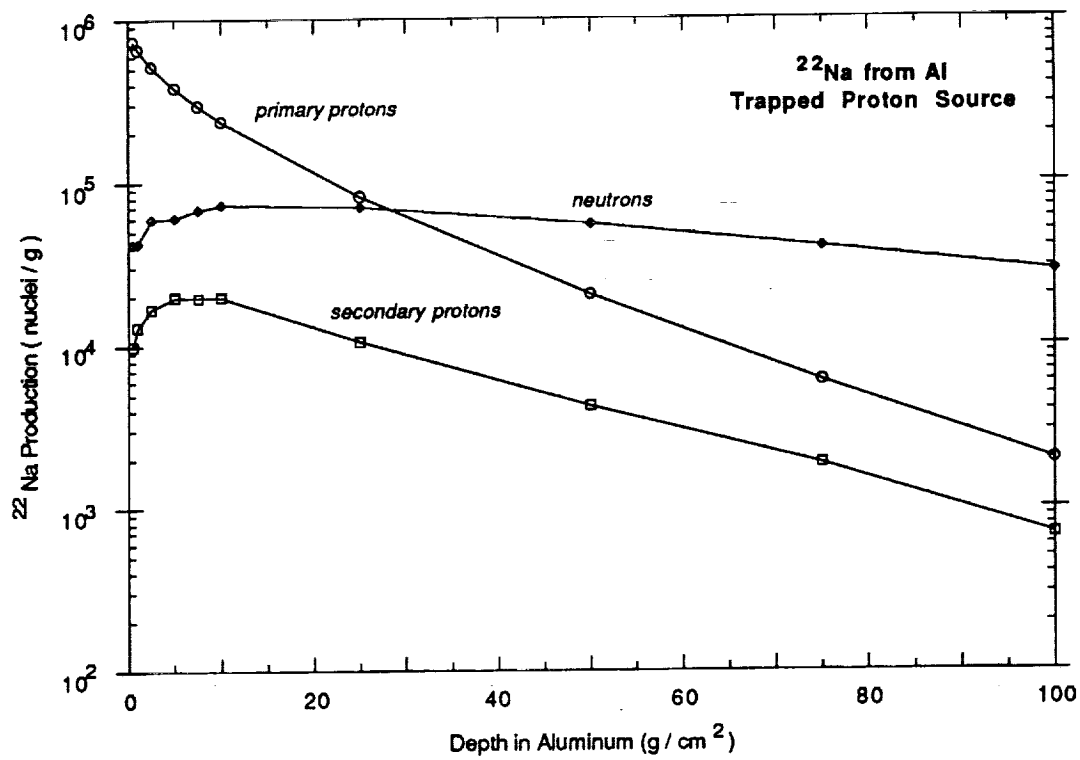


Fig. 12. Contribution of secondary particles in producing ²²Na from aluminum by incident trapped protons; top graph for production over LDEF mission, bottom graph as percentage of total production from primary and secondary particles by trapped protons.

4. Approximate Estimate of Activation Anisotropy and Comparison with LDEF Data

We consider here the directional dependence of induced radioactivity near the LDEF spacecraft surface due to anisotropy of the trapped proton exposure.

The results for ^{22}Na production from aluminum shown previously (Figs. 11 and 12) based on a 1-D geometry (with irradiation from one side) indicate that the dominate production mode near the surface is from primary trapped protons. While for the actual spacecraft geometry there may be some contribution from radiation entering the "opposite side", we neglect this contribution for now and assume a 1-D geometry model of effectively infinite thickness.

We have used anisotropic trapped proton spectra based on the Watts, et al.⁵ model (Fig. 13) and modified the 1-D MSFC straight-ahead proton transport code of Burrell¹¹ to compute activation products (using the activation cross sections of Appendix C) and to estimate the anisotropy of ^{22}Na production at small depths in aluminum. The results (Fig. 14) show a West/East anisotropy ratio for ^{22}Na production that varies from about a factor of 2 near the surface to a factor of 3.5 at 10 g/cm^2 depth.

These results are compared in Fig. 15 with recent preliminary measurements by Harmon, et al.¹⁰ for the ^{22}Na activation of LDEF aluminum clamp plates. (These plates are relatively thin, 1.29 g/cm^2 , and located on the surface of the spacecraft.) Based on an approximate fit we have made to the data points (Fig. 15), the measured West/East anisotropy is 1.8 compared to a calculated ratio of 2.0. In comparing absolute magnitudes, the calculations are higher than the measurements by about 30% for directions in the vicinity of East, and higher by about 50% for directions in the vicinity of West.

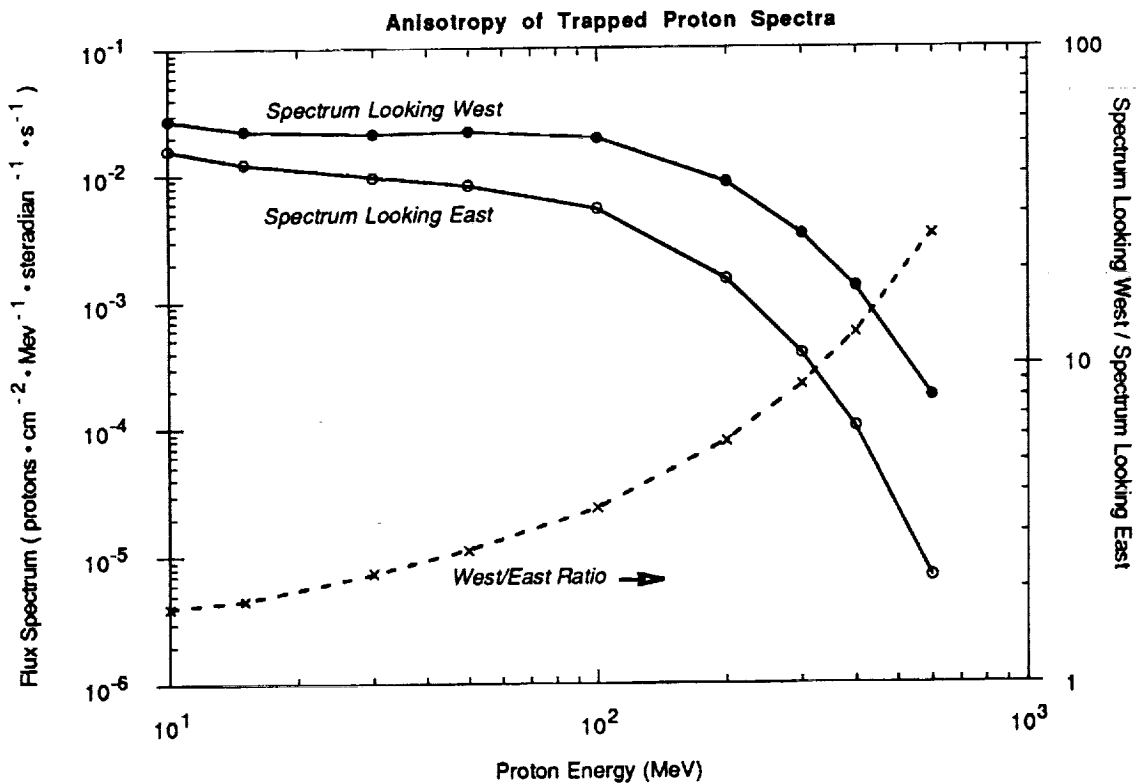
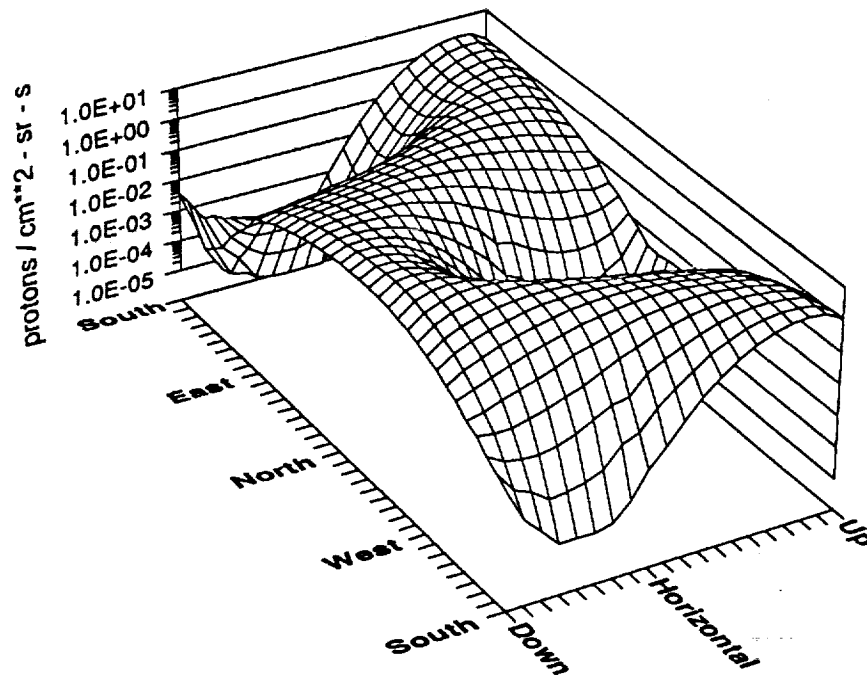


Fig. 13. (Top) Predicted anisotropy of trapped proton flux > 100 MeV, from Ref. 9, using the anisotropy model of Watts, et al ⁵. (Bottom) Trapped proton spectra in a differential solid angle looking West and looking East and the West/East ratio of the two spectra. Both graphs for orbit-average spectra (28.5° inclination, 450 km. altitude, solar minimum).

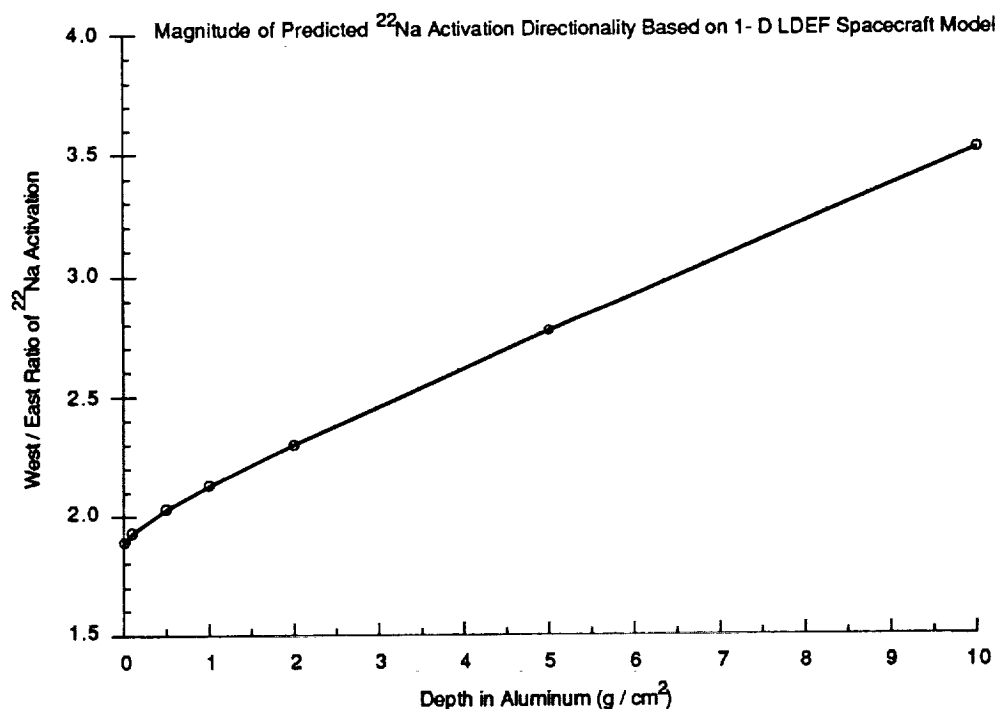
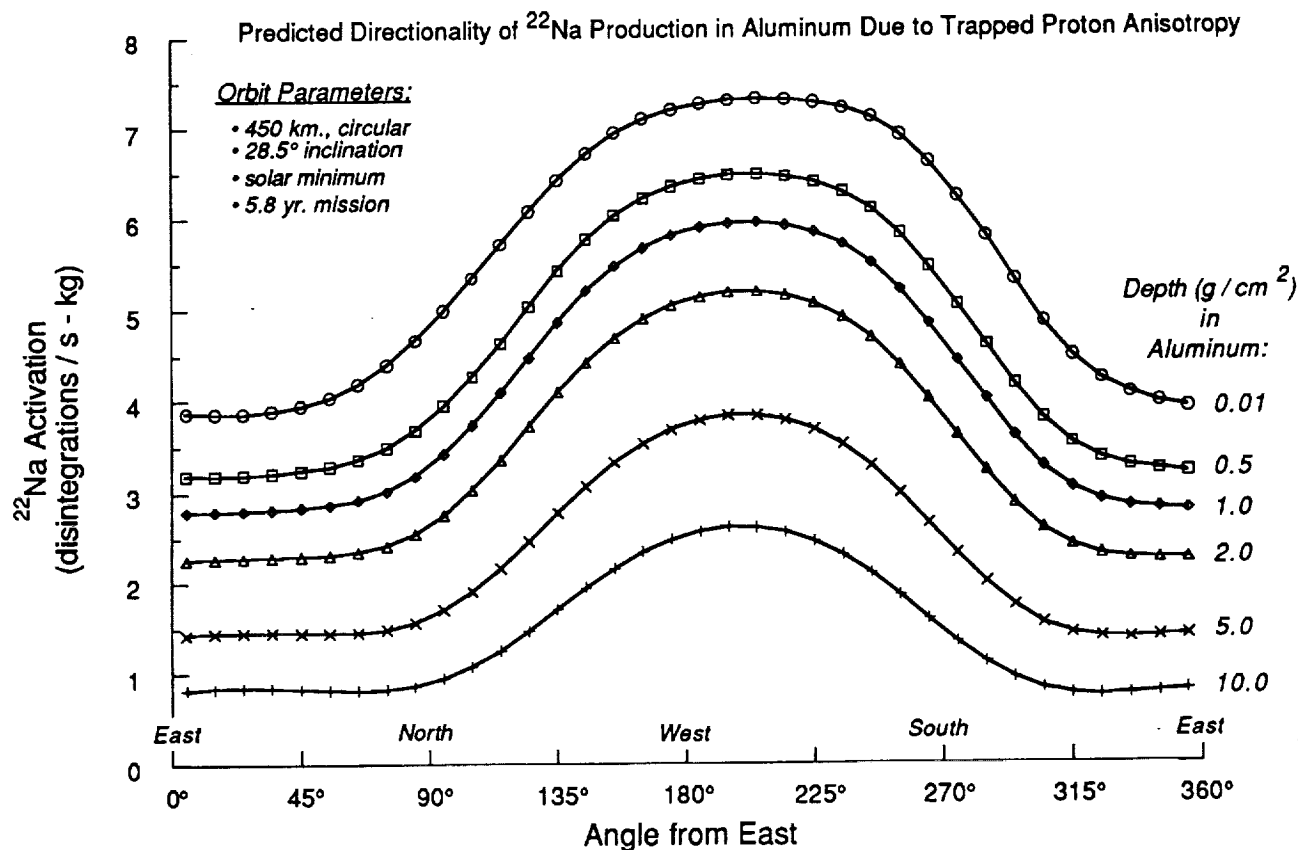


Fig. 14. Approximate calculation of ^{22}Na activation of aluminum from LDEF exposure to trapped protons in the South Atlantic Anomaly using a 1-D spacecraft model. The anisotropy of the trapped proton spectra is taken into account using the model of Watts, et al⁵. The top graph shows the depth dependence of the activation as a function of angle in the horizontal plane (90° from zenith) perpendicular to the spacecraft axis. The bottom graph shows the predicted increase in directionality with depth in terms of the activation on the West vs. East side of the spacecraft.

^{22}Na Activation of LDEF Aluminum Clamp Plates

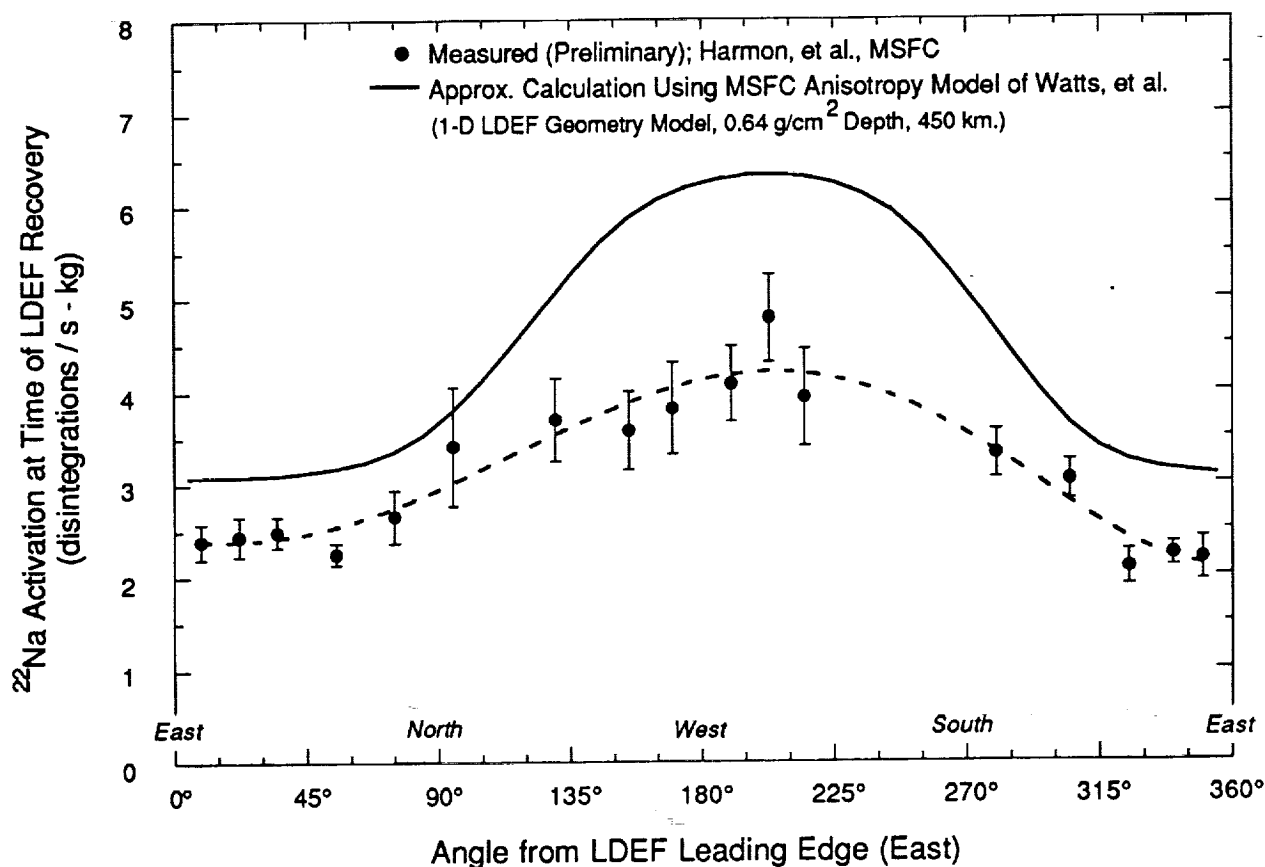


Fig. 15. Comparison of approximate calculations for ^{22}Na activation of LDEF aluminum clamp plates (used on outer surface of spacecraft to secure experimental trays) with the preliminary measurements of Harmon, et al.¹⁰ The calculated activation is at the mid-depth (0.64 g/cm²) of the clamp and based on a 1-D model of the spacecraft. The measured anisotropy (activation on West vs. East side of spacecraft) based on the approximate data fit shown is 1.8; the calculated anisotropy at this depth is 2.0.

5. References

1. Lenwood G. Clark, William H. Kinard, David J. Carter, Jr., and James L. Jones, Jr., "The Long Duration Exposure Facility (LDEF), Mission 1 Experiments", NASA SP-473, 1984.
2. G. J. Fishman, T. A. Parnell, and B. A. Harmon, "Long Duration Exposure Facility (LDEF) - Induced Radioactivity Analysis Plan", Proc. LDEF Ionizing Radiation Special Investigation Group Meeting, NASA Marshall Space Flight Center, December 1989.
3. T. A. Parnell, "Overview of LDEF Ionizing Radiation SIG", Proc. LDEF Ionizing Radiation Special Group Meeting, NASA Marshall Space Flight Center, December 1989.
4. T. W. Armstrong and K. C. Chandler, "The High-Energy Transport Code HETC", Nucl. Sci. Engr. 49, 110 (1972).
5. J. W. Watts, T. A. Parnell, and H. H. Heckman, "Approximate Angular Distribution and Spectra for Geomagnetically Trapped Protons in Low-Earth Orbit"; Sanibel Island, FL 1987 Conf.: "High-Energy Radiation Backgrounds in Space", A. C. Rester, Jr., and J. I. Trombka (Eds.), AIP Conf. Proc. 186, Am. Inst. Phys., New York, 1989.
6. T. W. Armstrong and B. L. Colborn, "A Thick-Target Radiation Transport Code for Low Mass Heavy Ion Beams, HETC/LHI", Nucl. Instr. Meth. 169, 161 (1980).
7. T. W. Armstrong, "The Intranuclear-Cascade-Evaporation Model", Chapter 20 in Computer Techniques in Radiation Transport and Dosimetry, Walter R. Nelson and Theodore M. Jenkins (Eds.), Plenum Press, New York, 1980.
8. E. A. Straker, P. N. Stevens, D. C. Irving, and V. R. Cain, "The MORSE Code - A Multigroup Neutron and Gamma-Ray Monte Carlo Transport Code", ORNL-4585, September, 1970.
9. T. W. Armstrong, B. L. Colborn, and J. W. Watts, "Trapped Proton Anisotropy", Minutes of SSF Ionizing Radiation Working Group Meeting, NASA Marshall Space Flight Center, May 1-3, 1990.
10. B. A. Harmon, G. J. Fishman, and T. A. Parnell, "LDEF Induced Radioactivity Analysis", Proc. LDEF Ionizing Radiation Special Investigation Group Meeting, NASA Marshall Space Flight Center, July 1990.
11. Martin O. Burrell, "The Calculation of Proton Penetration and Dose Rates", NASA TM X-53063, August 1964.

THE UNIVERSITY OF CHICAGO PRESS

CHICAGO, ILLINOIS

1963

THE UNIVERSITY OF CHICAGO PRESS

CHICAGO, ILLINOIS

1963

THE UNIVERSITY OF CHICAGO PRESS

CHICAGO, ILLINOIS

1963

THE UNIVERSITY OF CHICAGO PRESS

CHICAGO, ILLINOIS

1963

THE UNIVERSITY OF CHICAGO PRESS

CHICAGO, ILLINOIS

1963

THE UNIVERSITY OF CHICAGO PRESS

CHICAGO, ILLINOIS

1963

Appendix A

Sources of LDEF Ionizing Radiation Exposure

Trapped Protons (Omnidirectional)

The omnidirectional trapped proton spectrum calculated by Watts¹ was used as the trapped proton source for the HETC transport calculations. These spectra are based on the AP8MIN and AP8MAX trapped proton environment models² and the IGRF 1965.0 80-term magnetic field model projected to 1964, the epoch of the proton models. The cumulative flux over the duration of the LDEF mission was estimated by Watts by performing orbit average calculations (28.5° inclination, circular) at altitudes of 258.5, 255.0, 249.9, 230.0, and 172 nautical miles, which took place on mission days 0, 550, 1450, 1950, and 2105. A linear variation is assumed between time points. At altitudes of 230 and 170 nautical miles, the solar maximum model (AP8MAX) was used, with the solar minimum model (AP8MIN) used for other altitudes.

The resulting omnidirectional, altitude-average differential and integral cumulative trapped proton flux spectra over the duration of the LDEF mission are shown in Fig. A-1. For the one-dimensional transport calculation, one-half of this fluence was assumed to be incident isotropically on one side of the slab of material. While isotropy is a reasonable compromise for use in a one-dimensional approximation, the actual angular distribution is, as shown in the Sec. 4, highly anisotropic.

Trapped Electrons

The trapped electrons are of such low energy that they contribute significantly to the dose only at small penetration depths (≤ 0.5 g/cm²) (Ref. 1) and do not contribute at all to radionuclide production. Thus, transport calculations for trapped electrons have not been made here, but the trapped electron spectra are given in Fig. A-2 for comparison with trapped protons. These trapped electron spectra were computed by Watts¹ using the AE8MIN and AE8MAX trapped electron environment models^{3,4} and the same mission-averaged method as for the trapped protons given above.

Galactic Protons

For the galactic proton spectrum we start with the analytic fit given by Adams, et al.⁵ for the exomagnetospheric, time-dependent spectrum, which at solar minimum and solar maximum reduces to

$$F(E) = 10^m (E/117500)^a$$

where

$$m = 6.52 \exp\{-0.8 (\log_{10} E)^2\} - 4.0$$

$$a = -2.2\{1 - \exp[-b (\log_{10} E)^{2.75}]\}$$

$b = 0.117$ at solar minimum and $b = 0.079$ at solar maximum. Here F has units of protons $m^{-2} \text{ steradian}^{-1} \text{ MeV}^{-1}$ and E is in MeV. This fit to the galactic spectrum (multiplied by 4π steradians, converted to cm^{-2} , and multiplied by the LDEF mission duration of 2114 days) is shown as the "exomagnetosphere" spectrum in Fig. A-3.

To take into account the effect of geomagnetic shielding at the LDEF orbit, we have used the geomagnetic field "transmittance fraction" given in Adams, et al.⁶ for 30° inclination at 400 km altitude, which is based on the cosmic ray trajectory tracing calculations of Shea and Smart for effective geomagnetic cutoffs over a world-wide, longitude-latitude grid at 400 km altitude and the orbit averaging method of Heinrich and Spill⁷. This fraction of the exoatmospheric galactic protons transmitted through the geomagnetic field is shown in Fig. A-4, and the result of applying this transmission factor to the exomagnetospheric spectrum gives the curves labeled "LDEF orbit" in Fig. A-3.

Another factor influencing LDEF's exposure to galactic protons is the shielding effect of the earth's "shadow". The solid angle occultation is

$$\Delta \Omega = 2\pi \{1 - [(R_e + h)^2 - R_e^2]^{1/2} / (R_e + h)\}$$

where R_e is the earth's radius (6371 km) and h is the orbit altitude. For an average LDEF altitude of about 450 km, $\Delta \Omega / 4\pi = 0.32$. Thus, 32% of the 4π solid angle is blocked by the earth, and the incident proton directions are within $\pm 110^\circ$ about the zenith direction. In the transport calculations, the incident galactic proton flux was assumed incident isotropically over $\pm 90^\circ$ about the target surface normal.

The galactic proton integral and differential energy spectra over the LDEF mission duration are given in Fig. A-5.

*Albedo Protons**

Secondary protons produced in the earth's atmosphere by cosmic rays can escape upward as "splash albedo" and become trapped in the earth's magnetic field when the proton energy is below the geomagnetic cutoff. These protons are guided by the field to impact with the atmosphere in the hemisphere opposite to their formation, providing a "re-entrant" albedo.

The splash albedo spectrum has been measured by several balloon flights at different latitudes. In particular, Wenzel, et al.⁸ and Pennypacker, et al.⁹ measured the albedo spectrum in the 4 MeV to 1 GeV energy range at about 4 g/cm² residual atmosphere over Palestine, TX (42° N geomagnetic latitude, 4.5 GV geomagnetic cutoff). Measurements of the proton albedo by the Cosmos-721 satellite (polar orbit, 210-240 km) have been reported by Kuznetsov, et al.¹⁰ For a 4.5 GV cutoff they find a similar spectral shape as for the balloon flights but a factor of 4 higher intensity, which Kuznetsov, et al. attribute as possibly due to the different angular distribution of albedo protons at satellite vs. balloon altitudes.

For the splash albedo calculations in the present work we have used a fit to these satellite and balloon measurements, with the magnitude of the balloon data increased by a factor of 4 and the reported measurements per steradian multiplied by 2π to obtain an omnidirectional flux. These data and the fit used are shown in Fig. A-6, with the fit being

$$\phi = 0.00113 \exp(-0.0095E), \quad 10 \leq E \leq 115 \text{ MeV}$$

$$= 0.79 E^{-1.61}, \quad 115 < E \leq 2000 \text{ MeV}$$

where ϕ has units cm⁻² s⁻¹ MeV⁻¹. This differential flux multiplied by the LDEF mission duration, together with the corresponding integral fluence, is shown in Fig. A-7.

* We wish to thank J. Adams, Naval Research Laboratory, for providing background material on albedo proton measurements.

Some of the neutrons produced in the earth's atmosphere by cosmic-ray bombardment escape the top of the atmosphere to constitute a neutron albedo. Several measurements and calculations of the neutron albedo near the top of the atmosphere have been made -- e.g., Fig. A-8. The results of Fig. A-8 are for the upward moving flux at 45 km altitude, 42° N geomagnetic longitude, and solar minimum. We have fit the calculated spectrum as:

$$\begin{aligned}
 \phi(E) &= 0.047E^{-2.88}, & 10^{-5} \leq E < 0.1 \\
 &= 0.40 \exp(-0.97E), & 0.1 \leq E < 1.0 \\
 &= 0.15 E^{-1.34}, & 1.0 \leq E < 10 \\
 &= 0.0086 \exp(-0.045E), & \\
 &\quad + 0.0021 \exp(-0.0085E), & 10 \leq E < 200 \\
 &= 1.95 E^{-1.61}, & 200 \leq E \leq 3000
 \end{aligned}$$

where ϕ has units $\text{cm}^{-2} \text{ s}^{-1} \text{ MeV}^{-1}$ and E is in MeV.

The analytic fit of Fig. A-7 is scaled as follows to obtain an estimate of LDEF exposure to albedo neutrons. The maximum geomagnetic latitude reached by the LDEF orbit is $\lambda_m \approx 40^\circ$, which is approximately the latitude corresponding to the spectrum of Fig. A-7. From measurements of the 1-10 MeV albedo flux dependence on magnetic latitude, the variation of the albedo flux over LDEF orbits (ratio of flux at $\lambda_m = 40^\circ$ to flux at $\lambda_m = 0^\circ$) is about a factor of 3, and the ratio of the maximum albedo flux to the 28° inclination orbit-average flux is estimated to be a factor of ≈ 2 . Thus, while a detailed orbit integration has not been carried out to obtain the average LDEF exposure to albedo neutrons, the $\lambda_m = 42^\circ$ spectrum of Fig. A-7 is multiplied by 0.5 as an estimate of the orbit-average exposure. To take into account altitude differences, $1/r^2$ scaling is assumed and the 45 km spectrum of Fig. A-7 is multiplied by 0.88 to obtain the spectrum at 450 km, which is approximately the average LDEF altitude. Finally, the flux of Fig. A-7 is multiplied by the LDEF on-orbit time (2114 days) to obtain the albedo neutron fluence over the duration of the LDEF mission. The product of these scale factors (8×10^7) times the analytic fit curve of Fig. A-7 gives the estimate used for LDEF exposure to albedo neutrons (Fig. A-9).

At altitudes of about 450 km the albedo neutron directions are restricted within a cone half-angle of 70° about the zenith because the earth shields neutrons of other directions. Thus, in the transport calculations only neutron directions within $\pm 70^\circ$ about the slab normal were allowed.

Summary

Table A-1 below summarizes the energy range and normalization for the different sources used as input for the transport calculations. Also indicated is the angular distribution range assumed in computing the source spectra per unit solid angle.

Table A-1. Source parameters used for transport calculations.

Source	Minimum Incident Energy	Maximum Incident Energy	Omnidirectional Integral Fluence above E_{\min} (cm^{-2} , over LDEF Mission)	Range of Angular Distribution (steradians)
Trapped Protons	15 MeV	600 MeV	4.3×10^9	4π
Galactic Protons	3.2 GeV	100 GeV	2.8×10^7	2π
Albedo Protons	15 MeV	3.5 GeV	2.3×10^7	4π
Albedo Neutrons	1 keV	3.0 GeV	7.4×10^7	1.3π

References for Appendix A

1. J. W. Watts, "LDEF Dose Predictions and Measurement", LDEF Ionizing Radiation Special Investigation Group Meeting, NASA/MSFC, July 1990.
2. Donald M. Sawyer and James I. Vette, "AP-8 Trapped Proton Environment for Solar Maximum and Solar Minimum", National Science Data Center, Goddard Space Flight Center, NSSDC/WDC-A-R&S 76-06, 1976.
3. Michale J. Teague and James I. Vette, "A Model of the Trapped Electron Population for Solar Minimum", National Science Data Ceter, Goddard Space Flight Center, NSSDC 74-03, 1974.
4. Michael J. Teague, King W. Chan, and J. I. Vette, "AE6: A Model Environment of the Trapped Electrons for Solar Maximum", National Science Data Center, Goddard Space Flight Center, NSSDC/WDC-A-R&S 76-04, 1976.
5. J. H. Adams, Jr., R. Silberberg, and C. H. Tsao, "Cosmic Ray Effects on Microelectronics, Part I: The Near Earth Environment", NRL Memorandum Report 4506, August 1981.
6. J. H. Adams, Jr., J. R. Letaw, and D. F. Smart, "Cosmic Ray Effects on Microelectronics, Part II: The Geomagnetic Cutoff Effects", NRL Memorandum Report 5099, May 1983.
7. W. Heinrich and A. Spill, "Geomagnetic Shielding of Cosmic Rays for Different Satellite Orbits", J. Geophys. Res. 84, 4401 (1979).

8. K. P. Wenzel, E. C. Stone, and R. E. Vogt, "Splash Albedo Protons Between 4 and 315 MeV at High and Low Geomagnetic Latitudes", J. Geophys. Res. **80**, 3580 (1975).
9. C. R. Pennypacker, G. F. Smoot, A. Buffington, R. A. Mu, H. Smith, "Measurement of Geomagnetic Cutoff Near Palestine, Texas", J. Geophys. Res. **78**, 1515 (1973).
10. S. N. Kuznetsov, Yu I. Logachev, S. P. Ryumin, and G. A. Trebuckhovskaya, "Albedo of Galactic cosmic Rays from the COSMOS-721 Data", MG-28, p.161.
11. T. W. Armstrong, K. C. Chandler, and J. Barish, "Calculations of Neutron Flux Spectra Induced in the Earth's Atmosphere by Galactic Cosmic Rays", J. Geophys. Res. **78**, 2715 (1973).
12. A. M. Preszler, G. M. Simnett, and R. S. White, "Earth Albedo Neutrons from 10 to 100 MeV", Phys. Rev. Lett. **28**, 982 (1972).
13. R. S. White, S. Moon, A. M. Preszler, and G. M. Simnett, "Earth Albedo and Solar Neutrons", Rept. IGPP-UCR-72-16, U.C. Riverside, 1972.

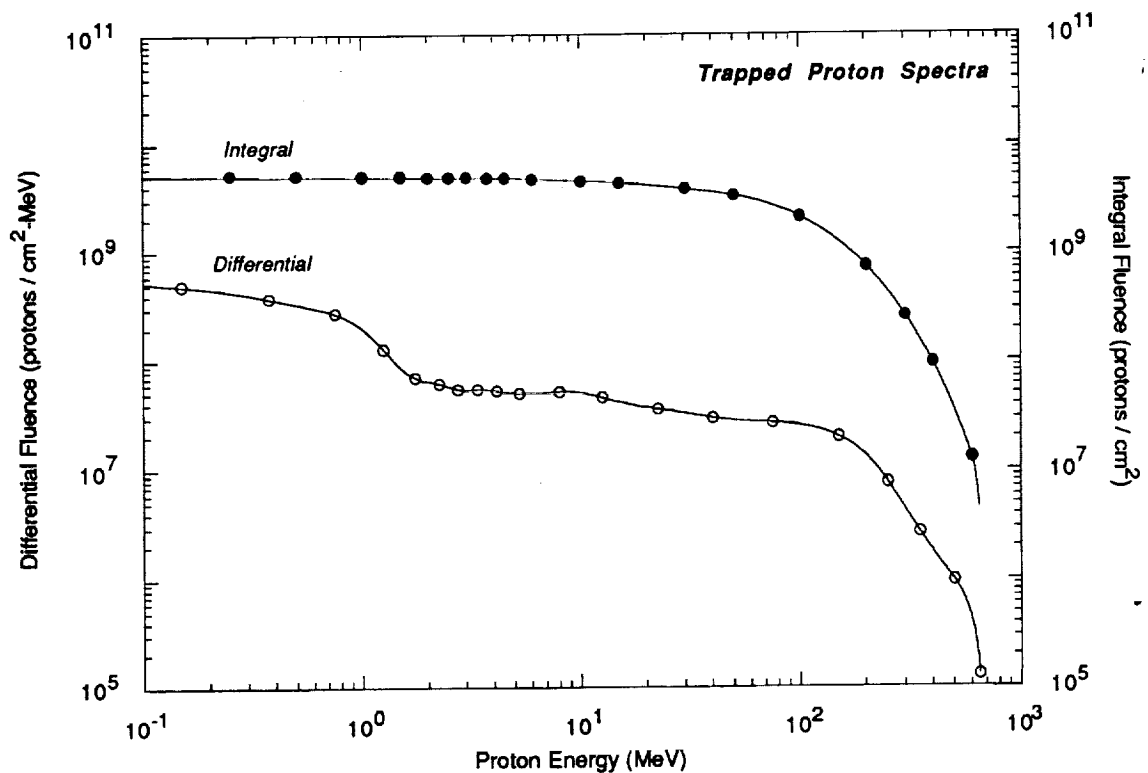


Fig. A-1. LDEF exposure to trapped protons, averaged over LDEF altitudes and cumulative over the LDEF mission duration, calculated by Watts¹ using the AP8MAX and AP8MIN environment models.² Shown here are *omnidirectional* spectra; as discussed in the text, the trapped proton spectra at the LDEF altitude and orbit inclination are actually highly anisotropic.

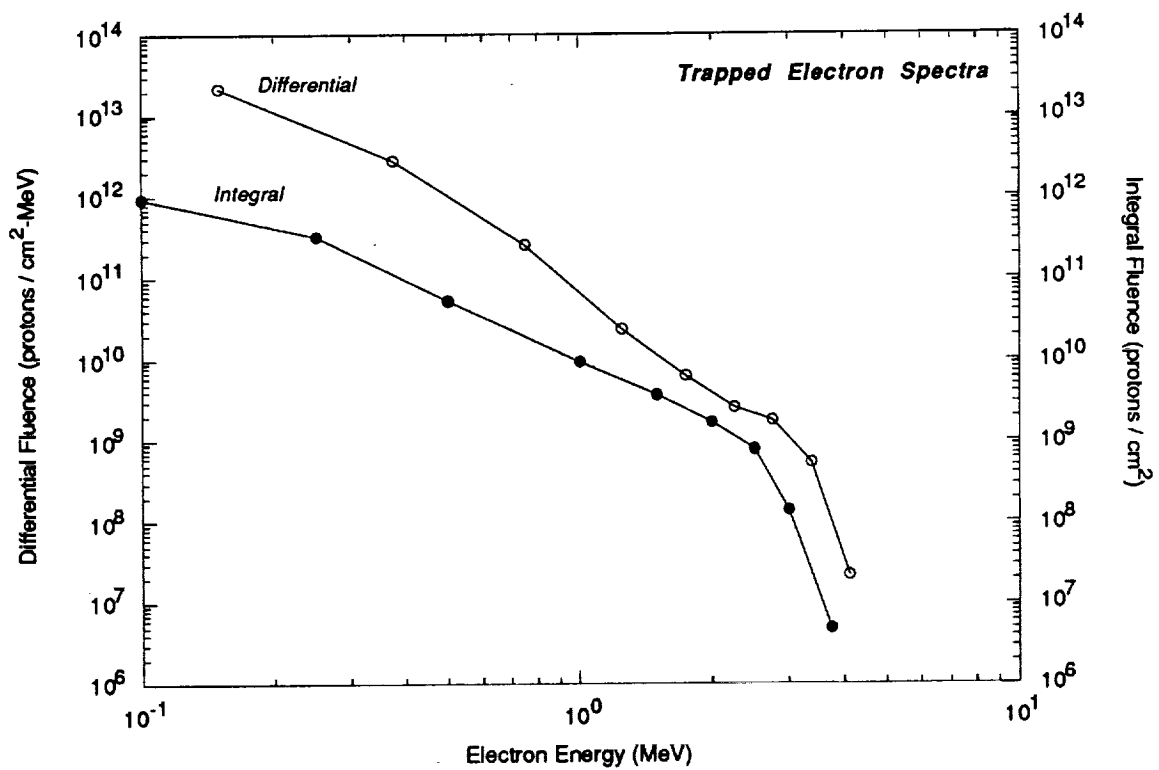


Fig. A-2. LDEF exposure to trapped electrons, averaged over LDEF altitudes and cumulative over the LDEF mission duration, calculated by Watts¹ using the AE8MIN and AEMAX environment models.^{3,4}

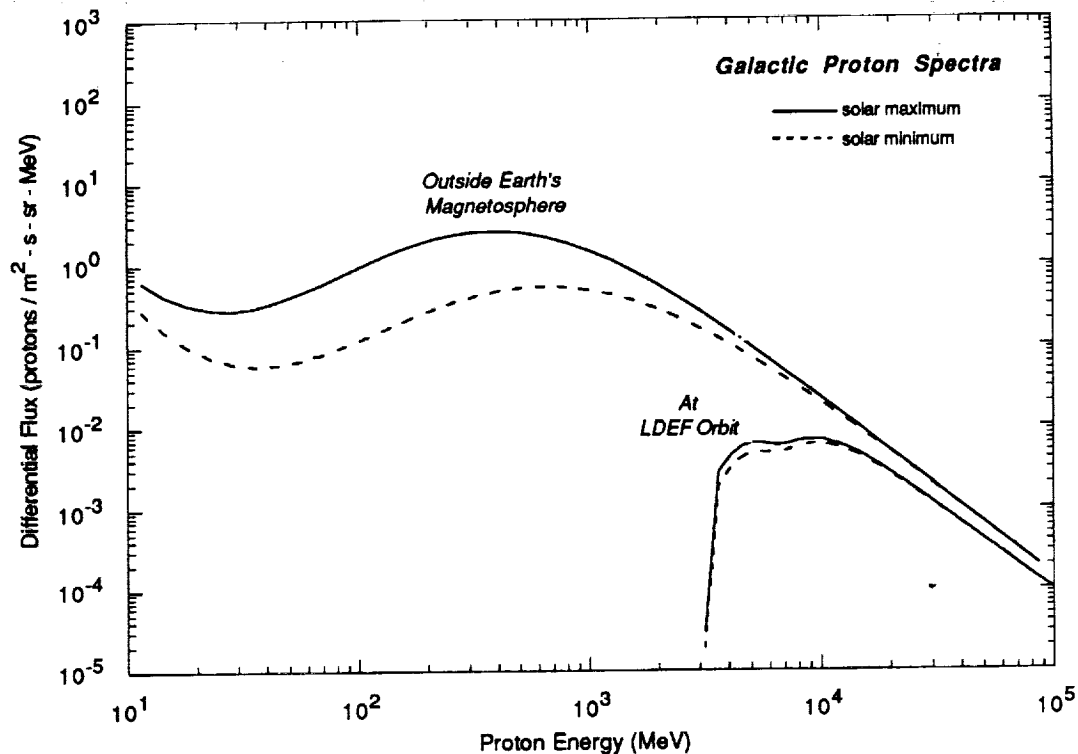


Fig. A-3. Galactic proton spectra in interplanetary space (from Adams, et al.⁵) and at LDEF orbit after attenuation by geomagnetic field.

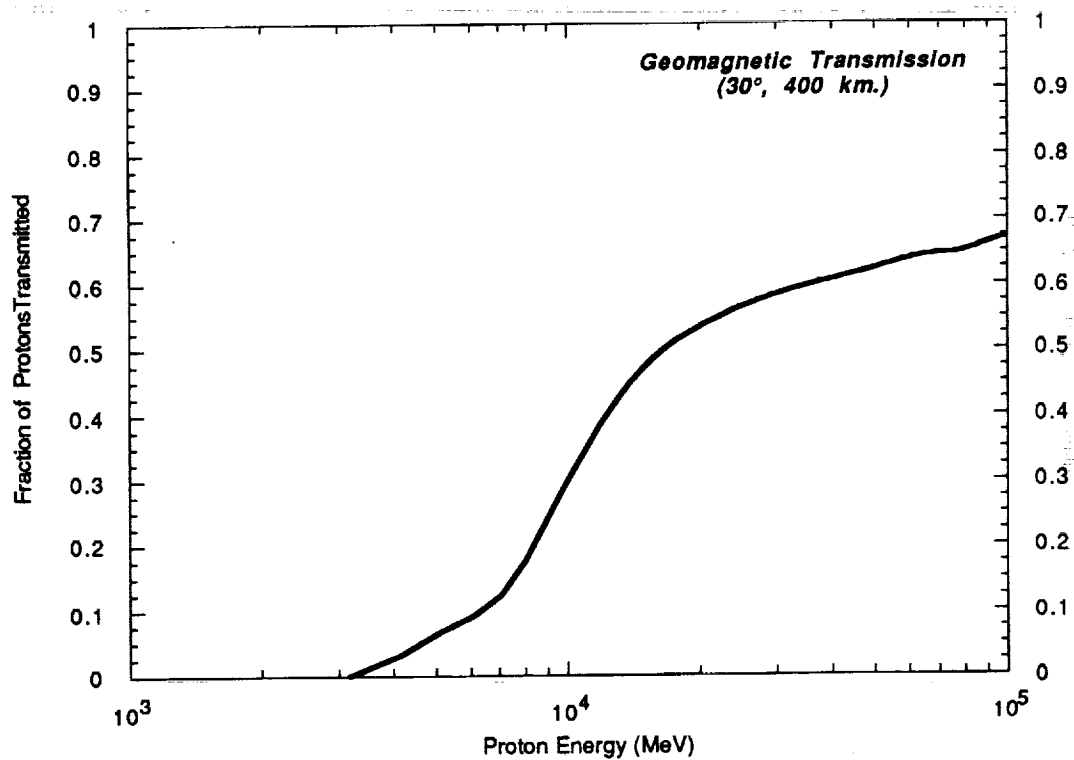


Fig. A-4. Transmission factor for galactic proton penetration of geomagnetic field; averaged over 30° inclination, circular orbit at 400 km. altitude (adapted from Adams, et al.⁶).

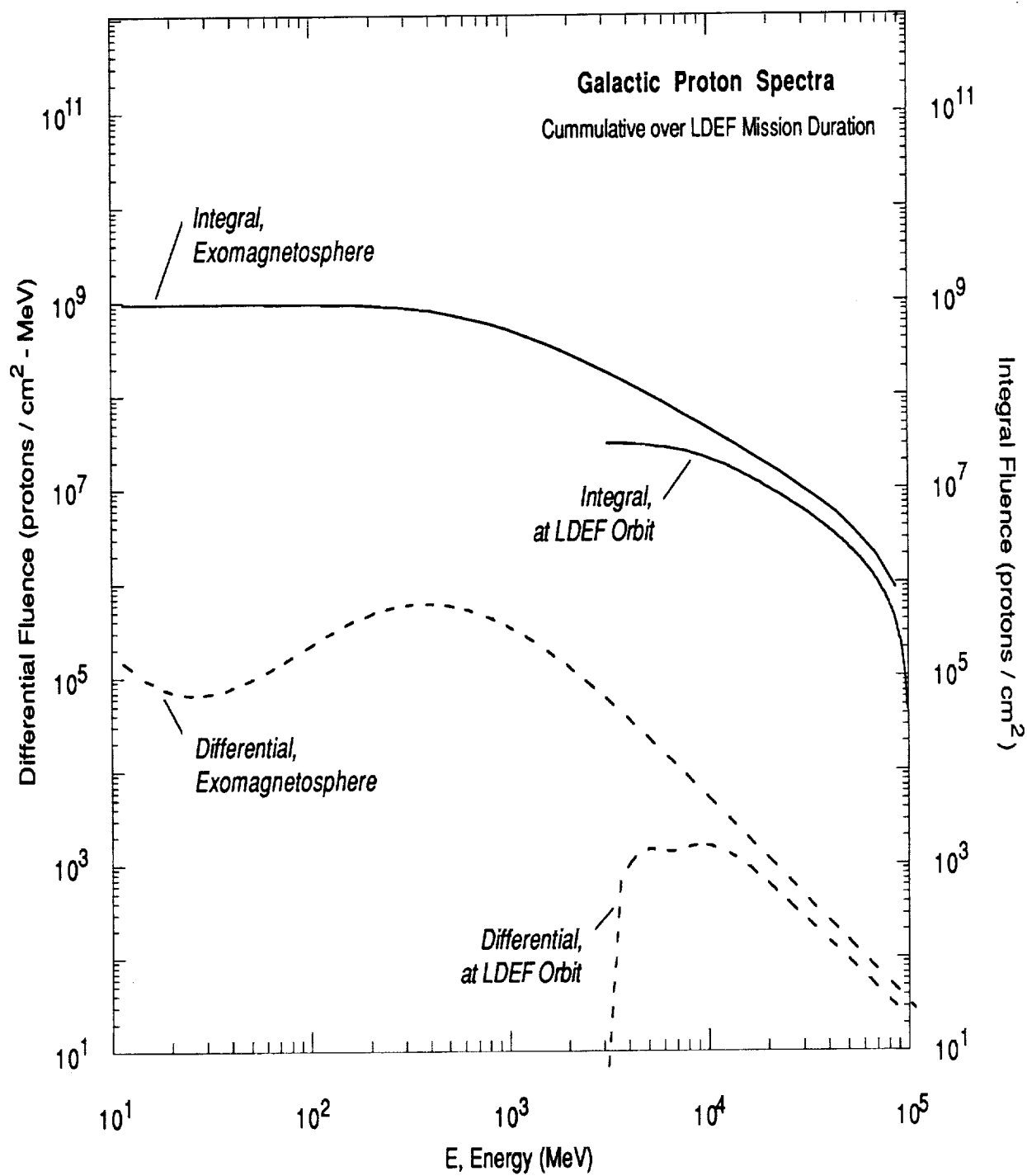


Fig. A-5. Cumulative galactic proton spectra over the duration of the LDEF mission.

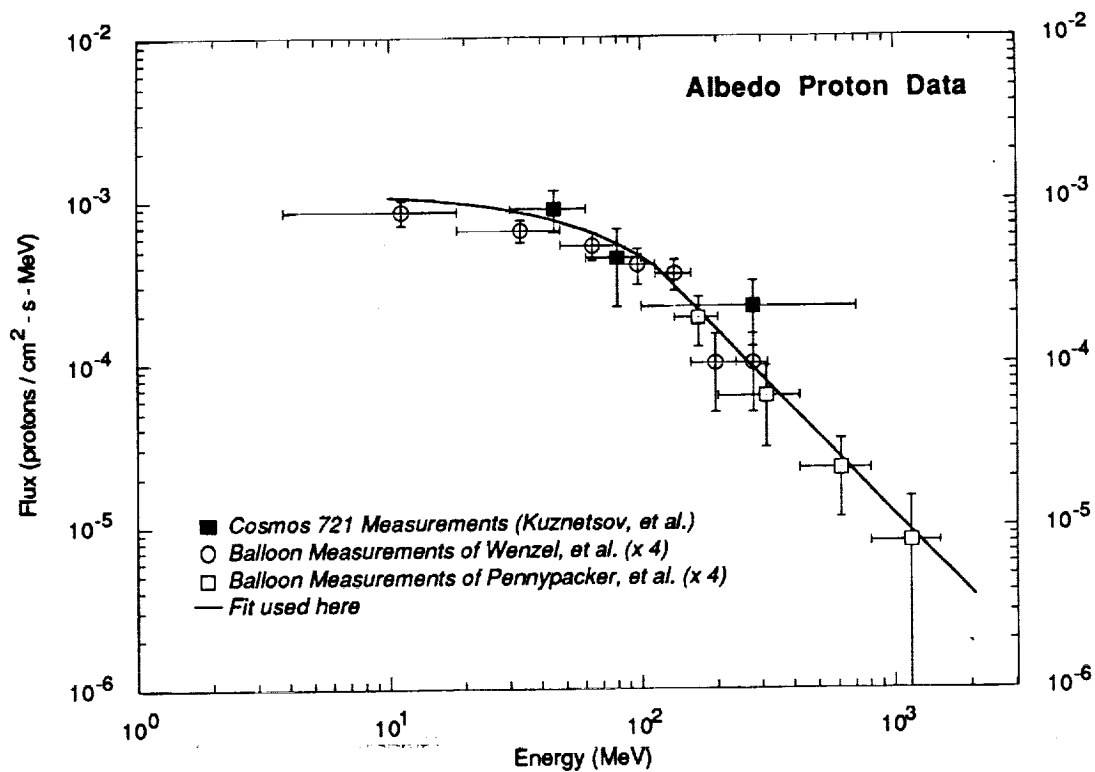


Fig. A-6. Measurements of the "splash" proton albedo spectrum at balloon^{7,8} and satellite⁹ altitudes. (The balloon data have been multiplied by a factor of four to get agreement with the magnitude of the satellite data.) Also shown is a fit to the data used here as input for the transport calculations.

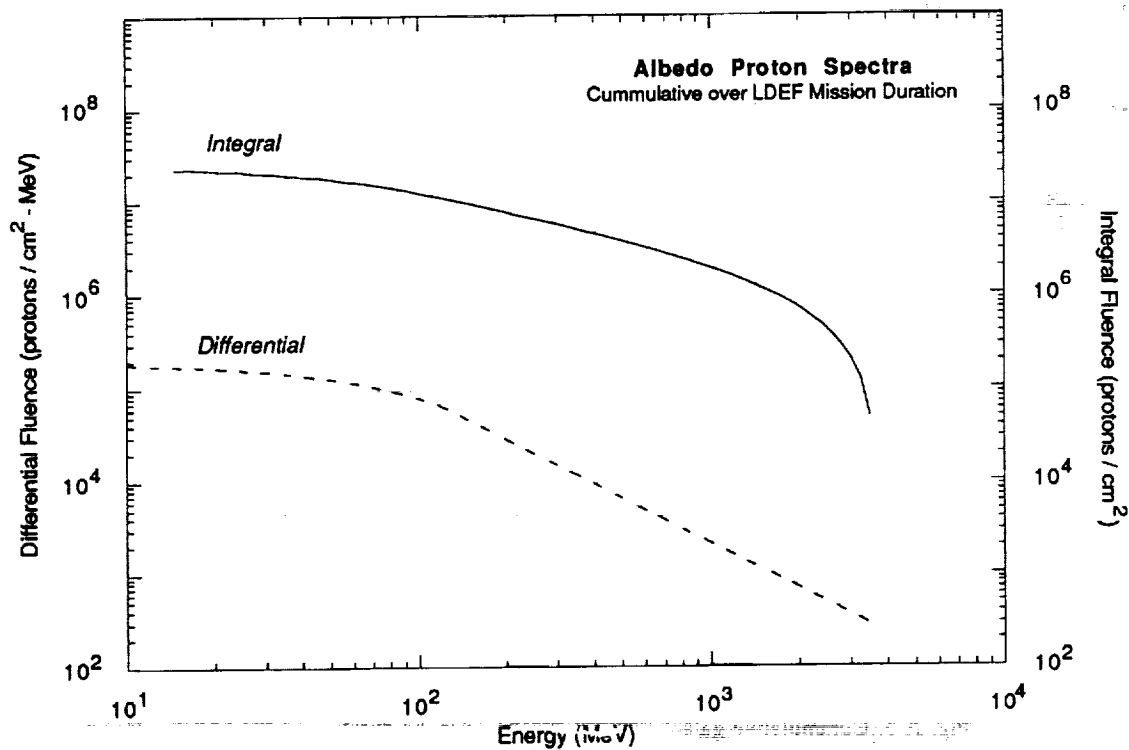


Fig. A-7. Cumulative albedo proton spectra over the duration of the LDEF mission.

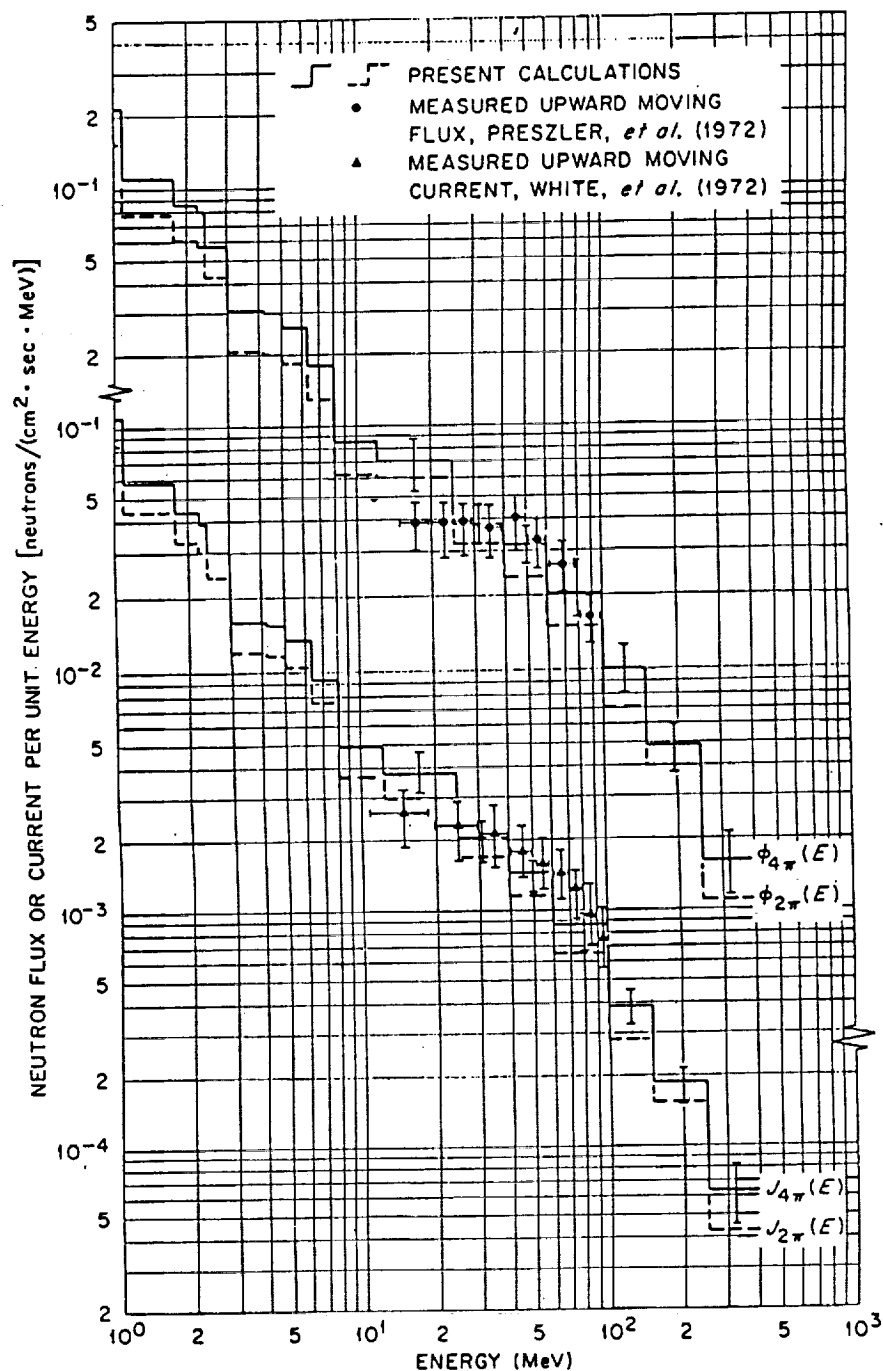


Fig. A-8. HETC code calculations of the neutron albedo spectra from cosmic-ray bombardment of the earth's atmosphere.¹¹ Shown are flux (ϕ) and current (J) spectra for the upward moving (2π) and omnidirectional (4π) neutrons at 5 g/cm^2 residual atmosphere, 42° N geomagnetic latitude, and solar minimum conditions. Also shown are data from balloon flight measurements by Preszler, et al.¹² and by White, et al.¹³

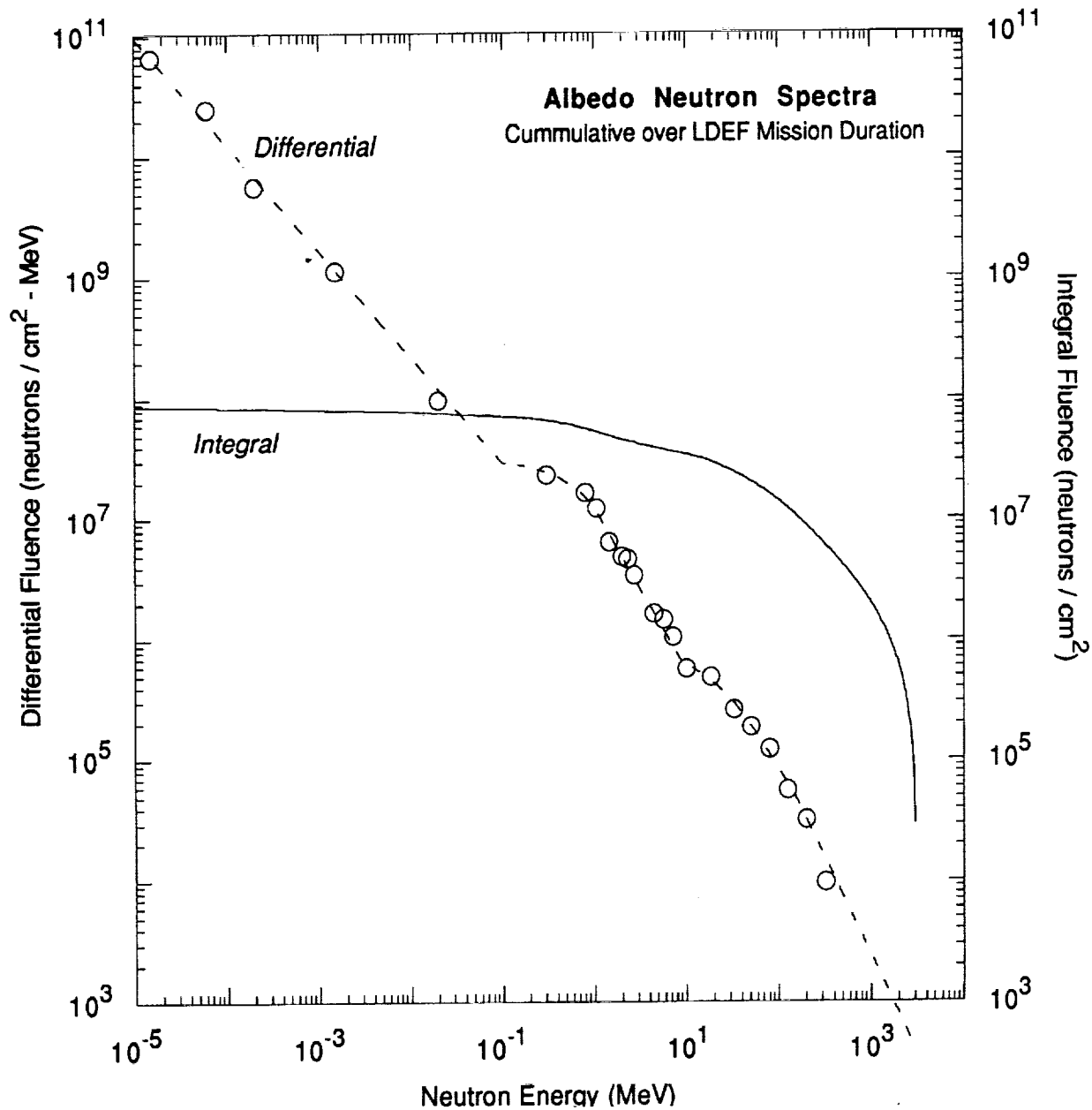


Fig. A-9. Cumulative neutron albedo spectra over the duration of the LDEF mission. The points (open circles) are from HETC code calculations of the differential spectrum at the top of the atmosphere (from Fig. A-8), which have been renormalized for the LDEF orbit.

Appendix B

Dose Response Functions

To estimate depth dependent doses the flux spectra at various depths from the transport calculations were folded with dose response functions. The response functions used (Figs. B-1 and B-2) are "surface doses" for protons or neutrons incident normally on a slab of tissue or silicon.

For protons incident on tissue, the response function was estimated using the stopping power approximation of Burrell¹ below 60 MeV and the transport calculation results of Zerby and Kinney² in the range from 60 to 400 MeV, Alsmiller, et al.³ from 400 MeV to 3 GeV, and Armstrong and Chandler⁴ from 3 GeV to 100 GeV. For neutrons incident on tissue, results from Irving, et al.⁵ were used below 60 MeV, from Alsmiller, et al.³ between 60 MeV and 3 GeV, and from Armstrong and Chandler⁴ between 3 GeV and 100 GeV.

For protons incident on silicon, the Burrell¹ stopping power approximation was used below 200 MeV with the HETC code kerma factor calculations of Zazula, et al.⁶ used above 200 MeV. The response to neutrons is based on the DLC-31 data library⁷ below 20 MeV and the Zazula, et al.⁶ calculations at higher energies.

References for Appendix B

1. Martin O. Burrell, "The Calculation of Proton Penetration and Dose Rates", NASA TM X-53063, August 1964.
2. C. D. Zerby and W. E. Kinney, Nucl. Instru. Meth. 36, 125 (1965).
3. R. G. Alsmiller, Jr., T. W. Armstrong, and W. A. Coleman, "The Absorbed Dose and Dose Equivalent from Neutrons in the Energy Range 60 to 3000 MeV and Protons in the Energy Range 400 MeV to 3000 MeV", Nucl. Sci. Engr., 42, 367 (1970).
4. T. W. Armstrong and K. C. Chandler, "Calculation of the Absorbed Dose and Dose Equivalent from Neutrons and Protons in the Energy Range from 3.5 GeV to 1.0 TeV", Health Phys. 24, 277 (1973).
5. D. C. Irving, R. G. Alsmiller, Jr., and H. S. Moran, "Tissue Current-to-Dose Conversion Factors for Neutrons from 0.5 to 60 MeV", ORNL-4432, August 1967.
6. J. M. Zazula, P. Cloth, D. Filges, and G. Sterzenbach, "Secondary Particle Yield and Energy Release Data from Intranuclear-Cascade-Evaporation Model Calculations of High Energy (20 - 1100 MeV) Neutron Interaction with Elements of Shielding and Biological Importance", Nucl. Instr. Meth. B16, 506 (1986).
7. DLC-31, "37 Neutron, 21 Gamma Ray Coupled Multigroup Library", Radiation Shielding Information Center, Data Library Collection DLC-31/(DPL-1/FEWG1), Oak Ridge National Laboratory, 1976.

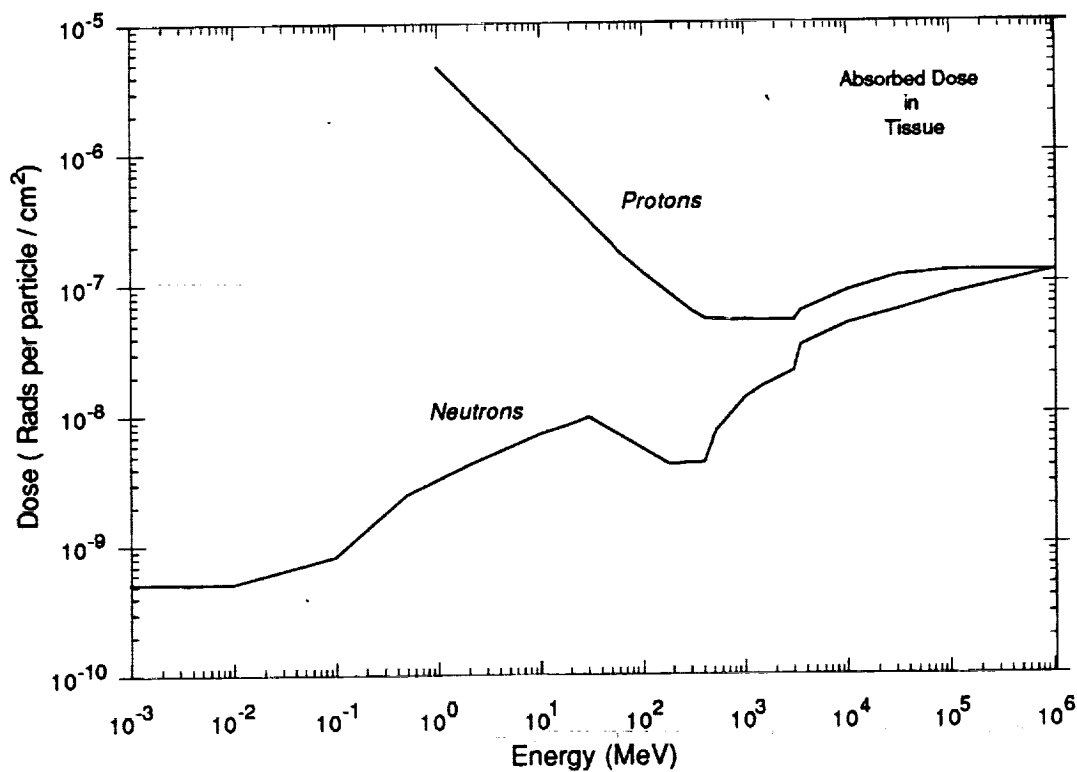


Fig. B-1. Flux-to-dose conversion factors used for absorbed dose in tissue.

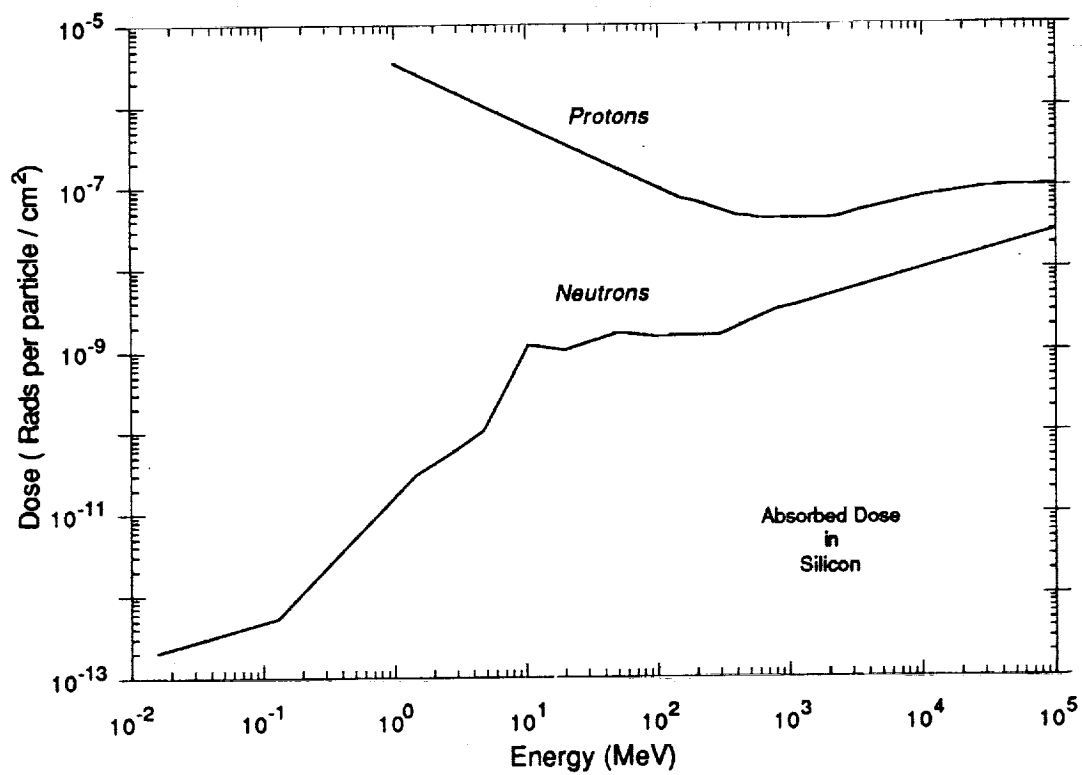


Fig. B-2. Flux-to-dose conversion factors used for absorbed dose in silicon.

Appendix C

Activation Cross Sections

Michel and co-workers (e.g., Ref. 1) have developed a set of activation cross sections for neutrons and protons incident on various elements by using a combination of experimental data, semi-empirical methods, and nuclear models. Predictions of the spatial dependence of radioisotope production in thick composite targets using the Michel, et al. cross section set folded with flux spectra calculated by the HETC transport code are in very good agreement with experimental data for high-energy proton irradiations². Thus, in these initial calculations we have used the Michel, et al.² activation cross sections shown in Figs. C-1 through C-3.

References for Appendix C

1. R. Michel and R. Stück, J. Geophys. Res. **89**, B673, (1984).
2. D. Aylmer, et al., "Monte Carlo Modelling and Comparison with Experiment of the Nuclide Production in Thick Stony Targets Isotropically Irradiated with 600 MeV Protons", CERN SC96 Experiment, Kernforschungsanlage Julich GMBH, Report Jul-2130, May 1987.

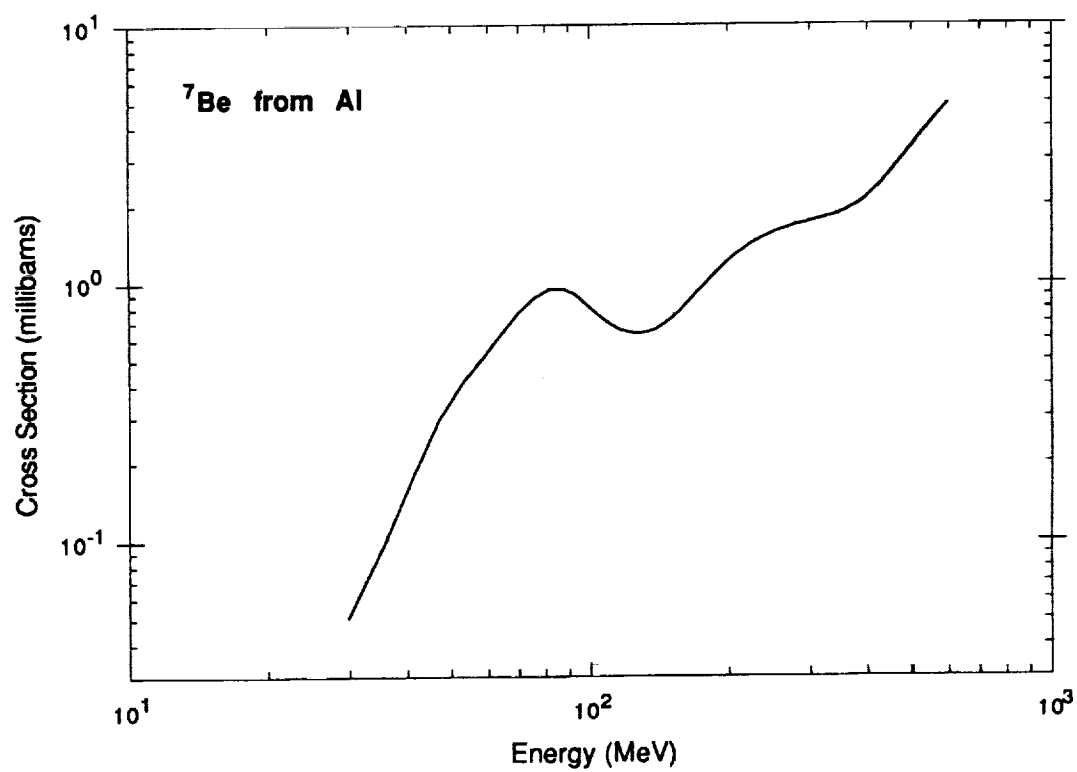
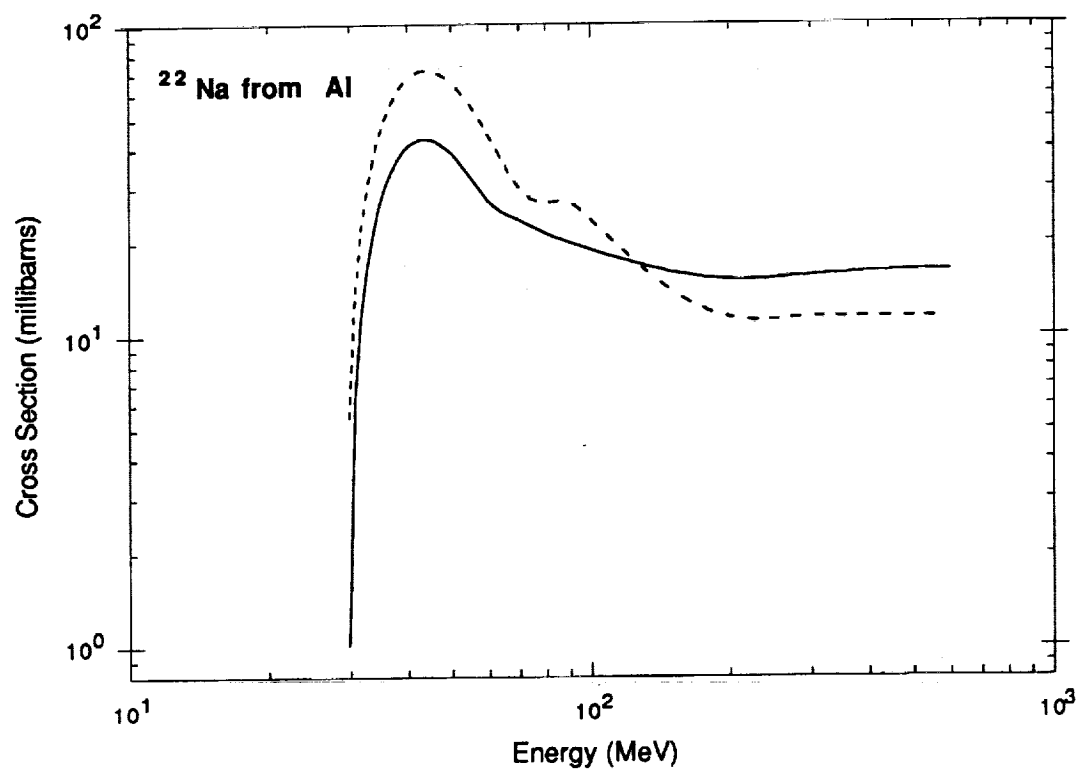


Fig. C-1. Cross sections for ^{22}Na and ^7Be production from aluminum; solid line by protons, dashed line by neutrons.

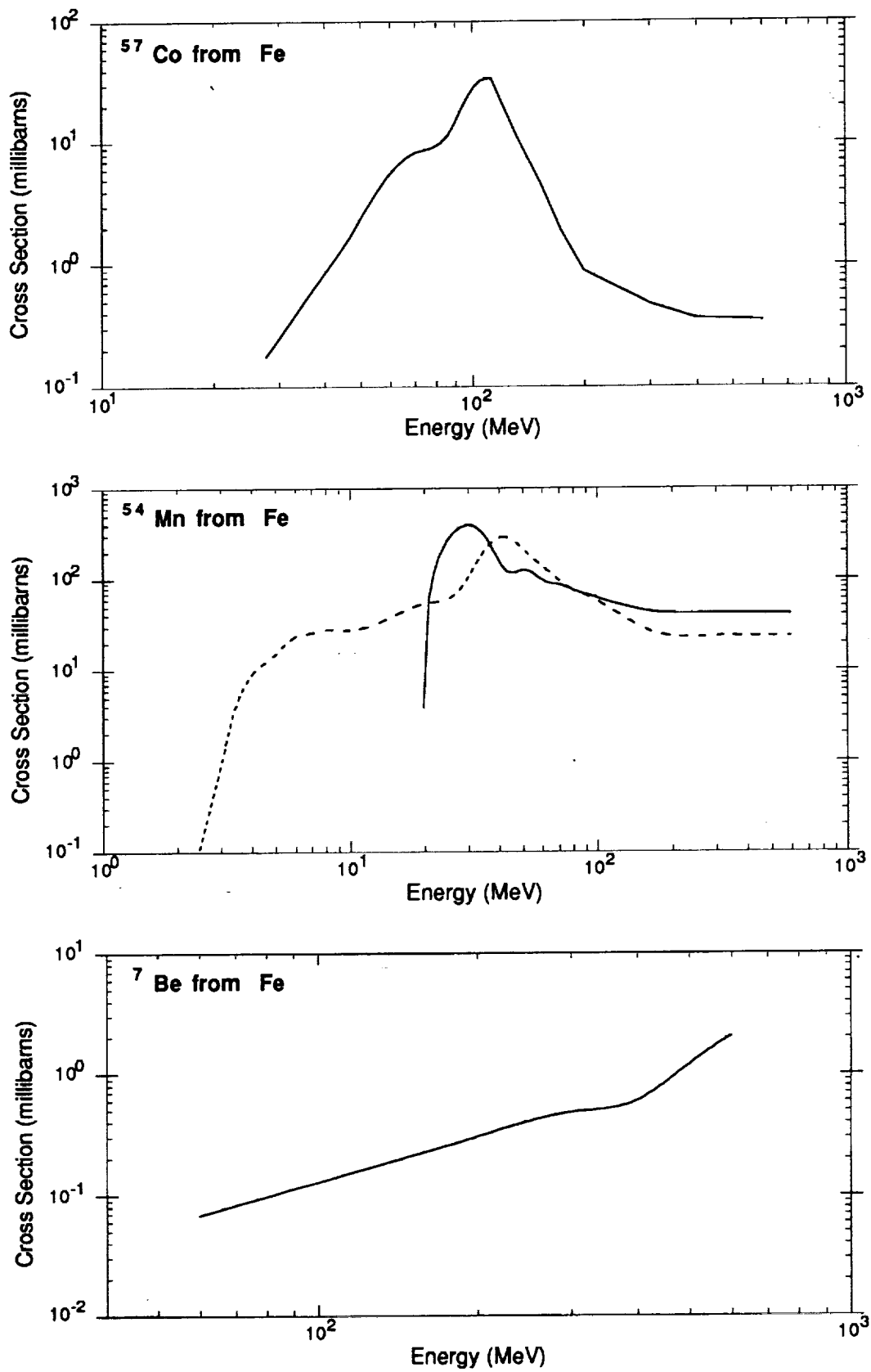


Fig. C-2. Cross sections for ^{57}Co , ^{54}Mn and ^7Be production from iron; solid line by protons, dashed line by neutrons.

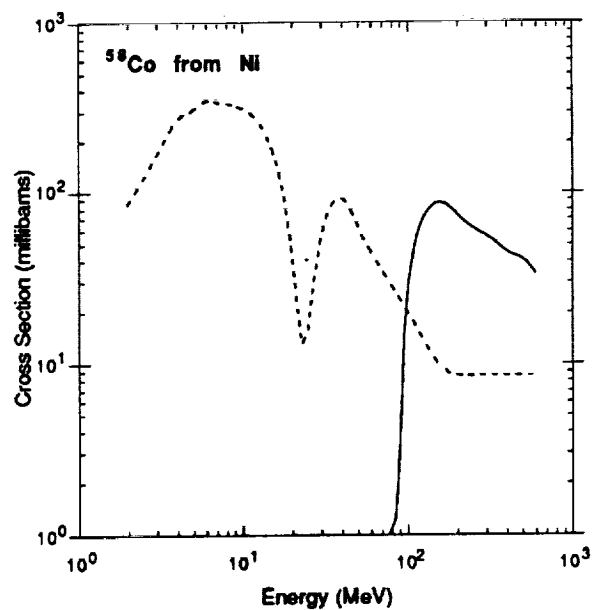
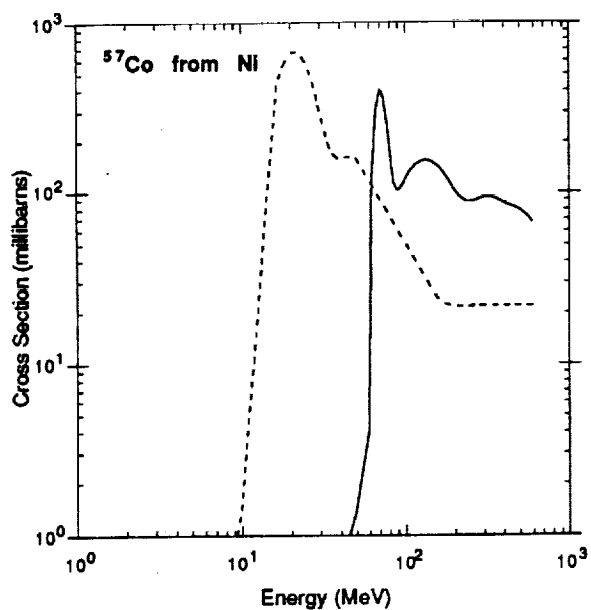
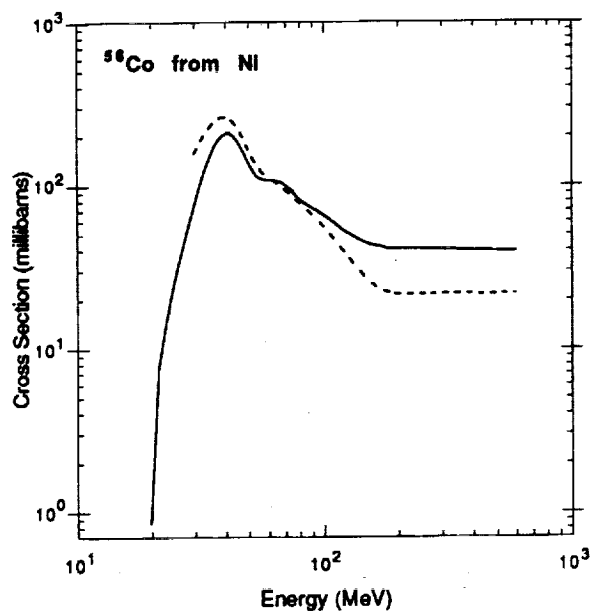
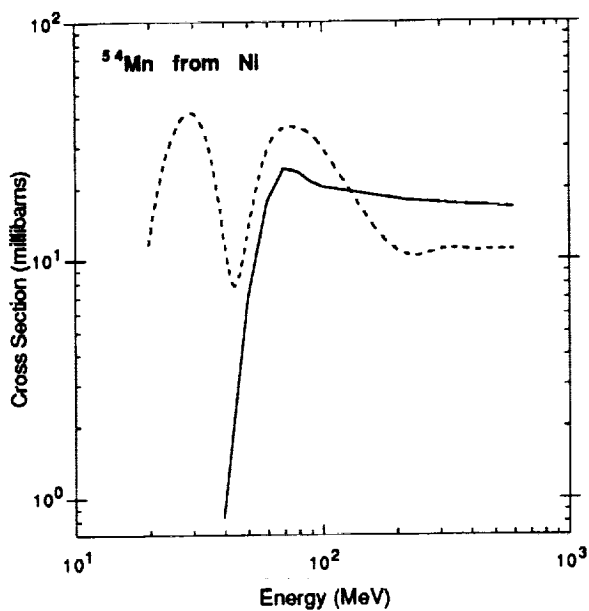


Fig. C-3. Cross sections for ^{54}Mn , ^{56}Co , ^{57}Co and ^{58}Co production from nickel; solid line by protons, dashed line by neutrons.

Appendix D

Additional Fluence Results

Figs. D-1 through D-4 compare the depth dependent fluences (over all energies) for primary and secondary particles for LDEF exposure to trapped proton, galactic proton, albedo proton, and albedo neutron sources.

Fluence spectra of protons and neutrons from all sources are compared for 10 and 50 g/cm² aluminum shielding depths in Figs. D-5 and D-6.

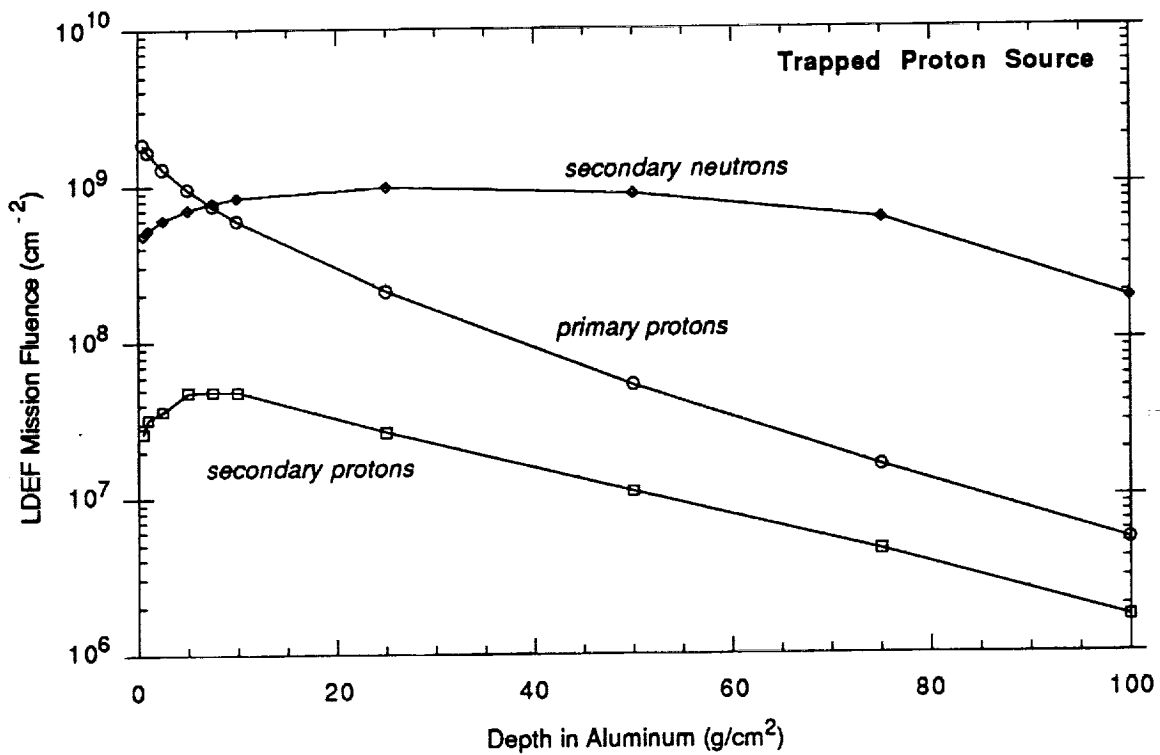


Fig. D-1. Secondary particle production for trapped proton source.

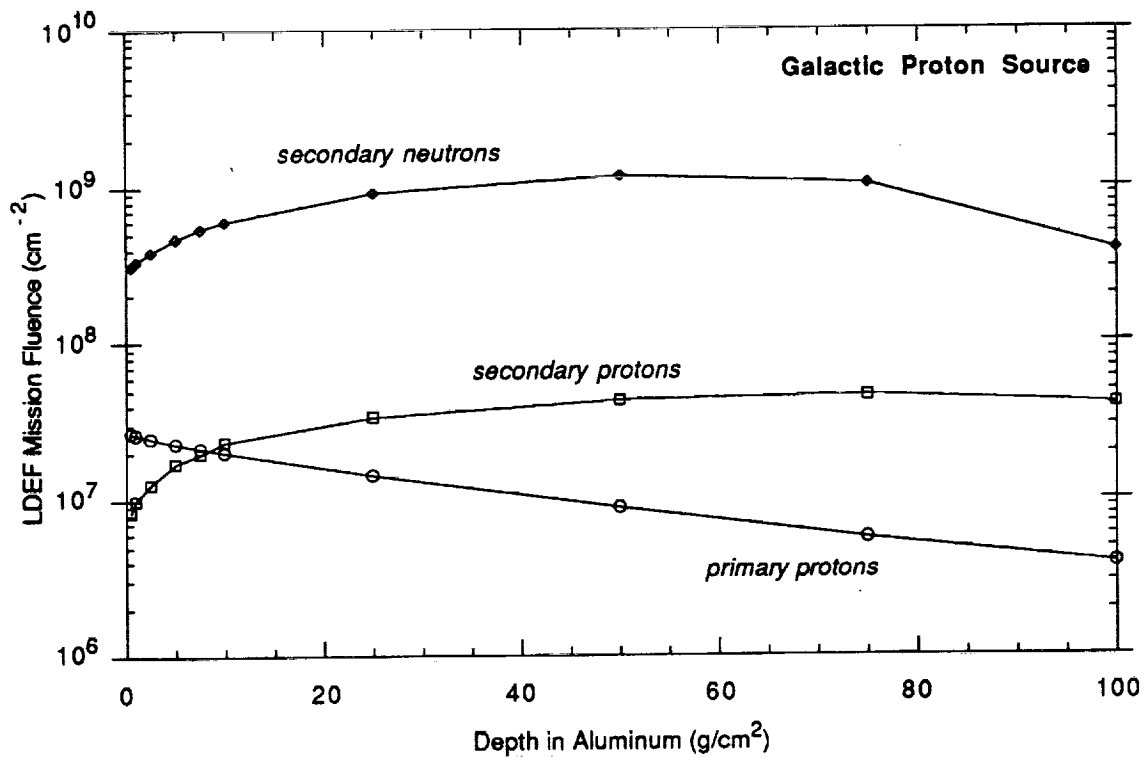


Fig. D-2. Secondary particle production for galactic proton source.

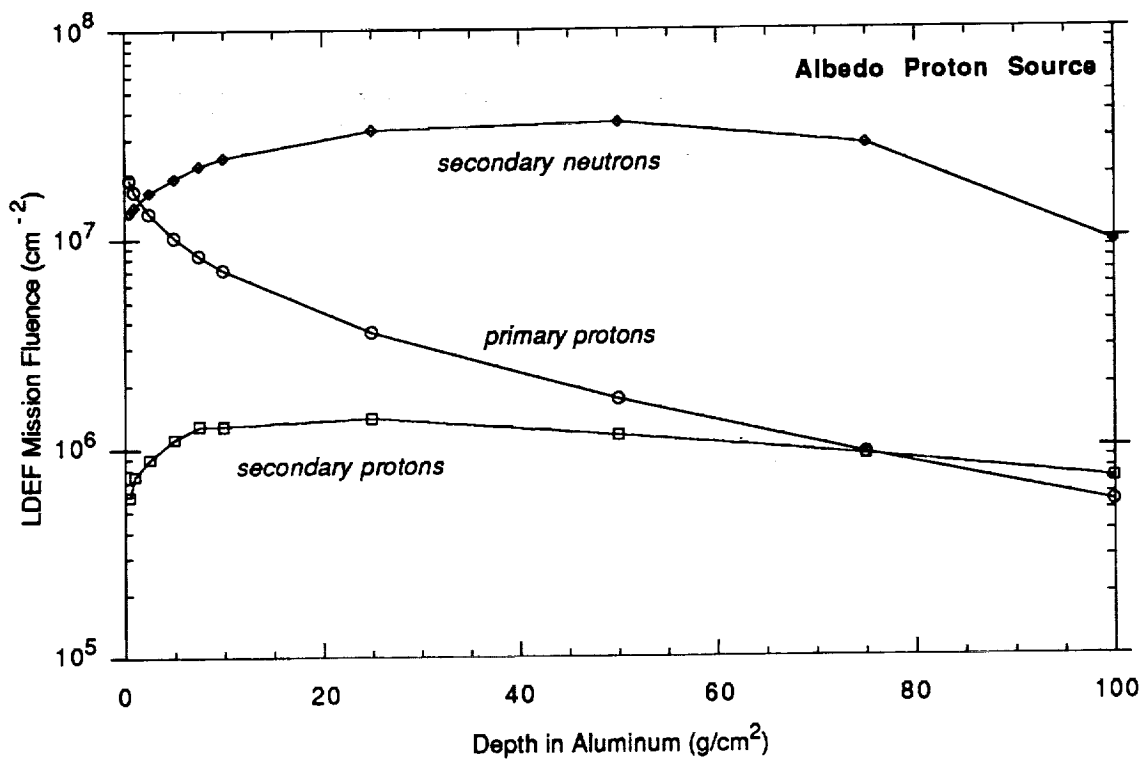


Fig. D-3. Secondary particle production for albedo proton source.

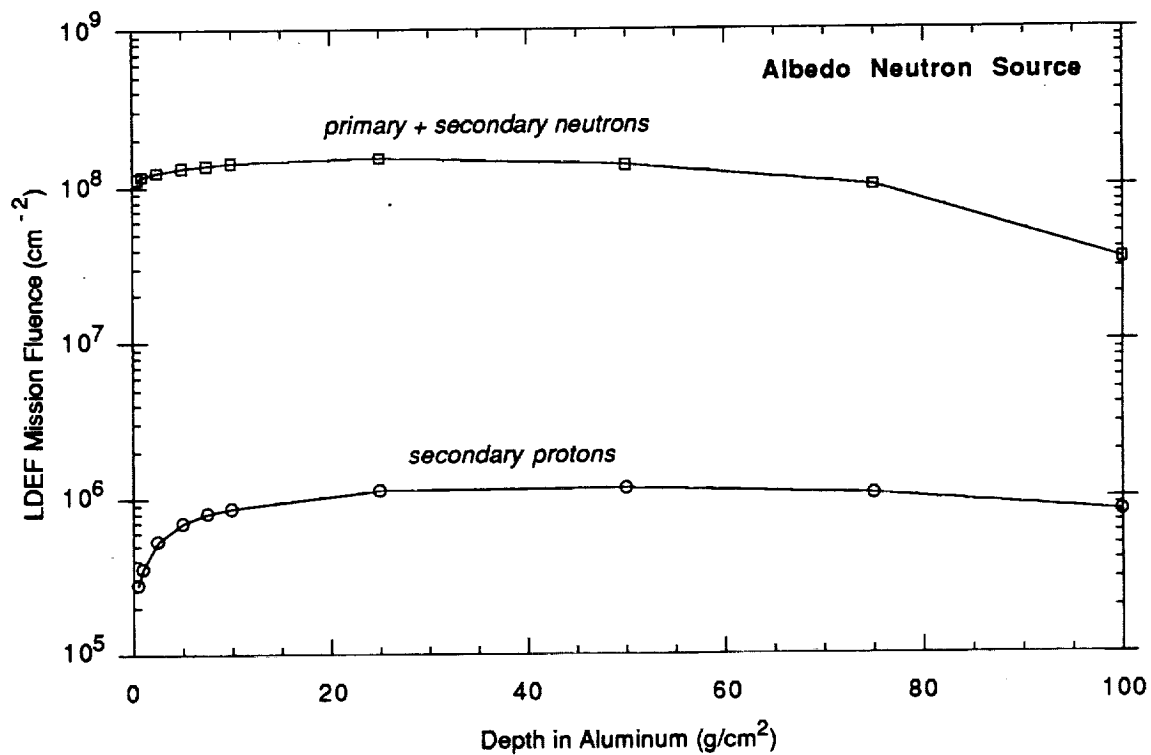


Fig. D-4. Secondary particle production for albedo neutron source.

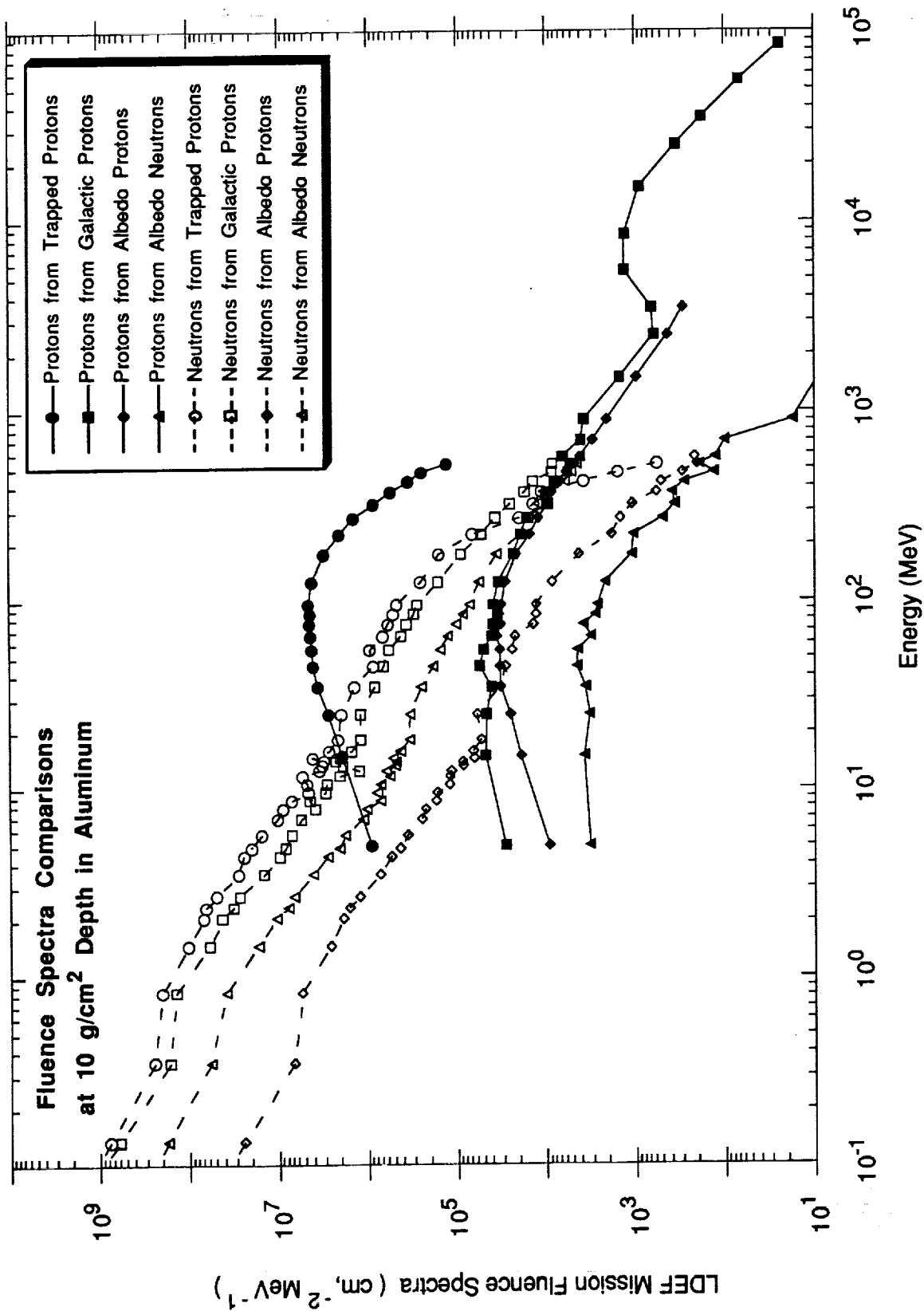


Fig. D-5. Comparison of fluence spectra at a depth of 10 g/cm² in aluminum from LDEF exposure to different ionizing radiation sources.

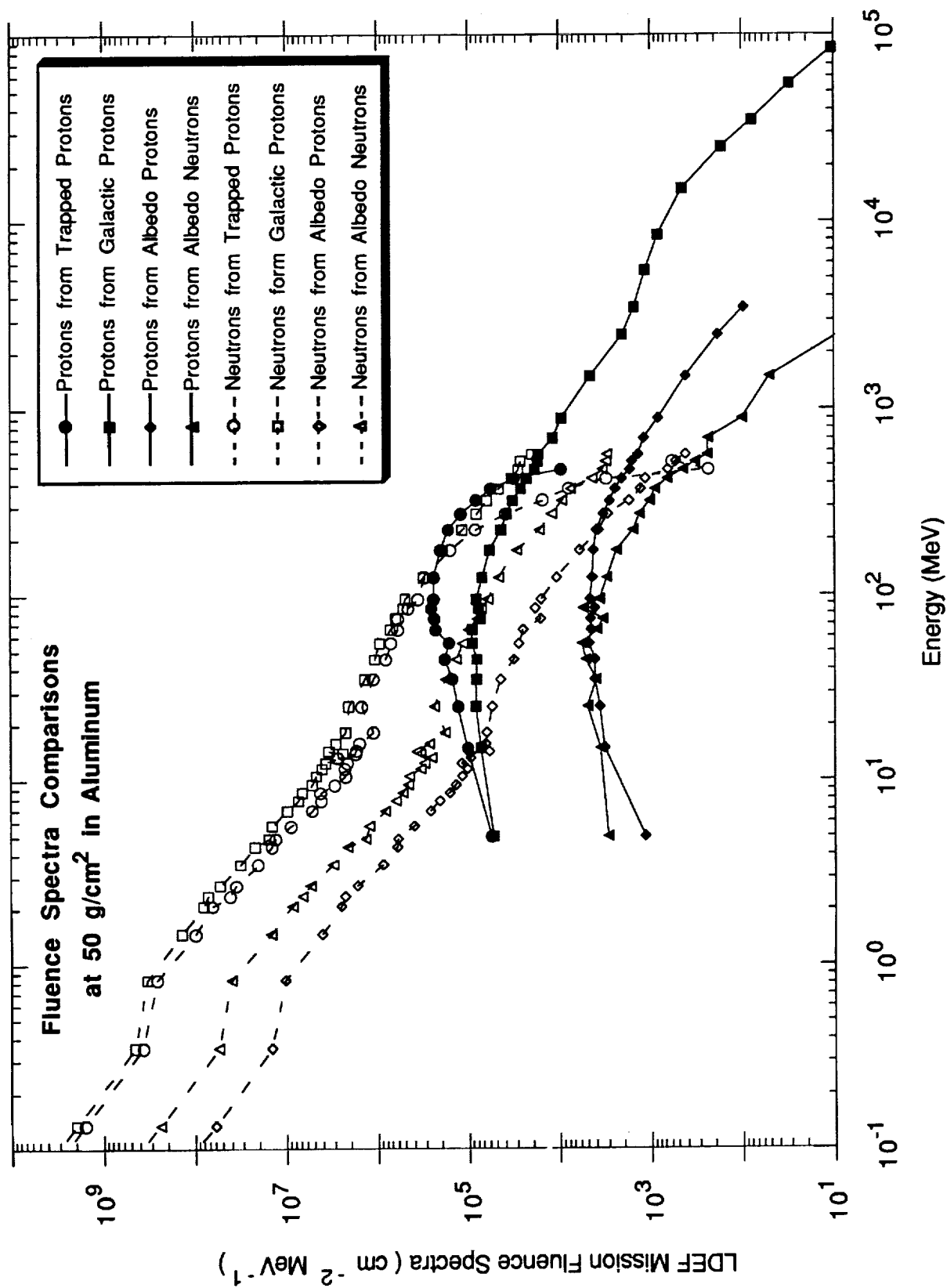
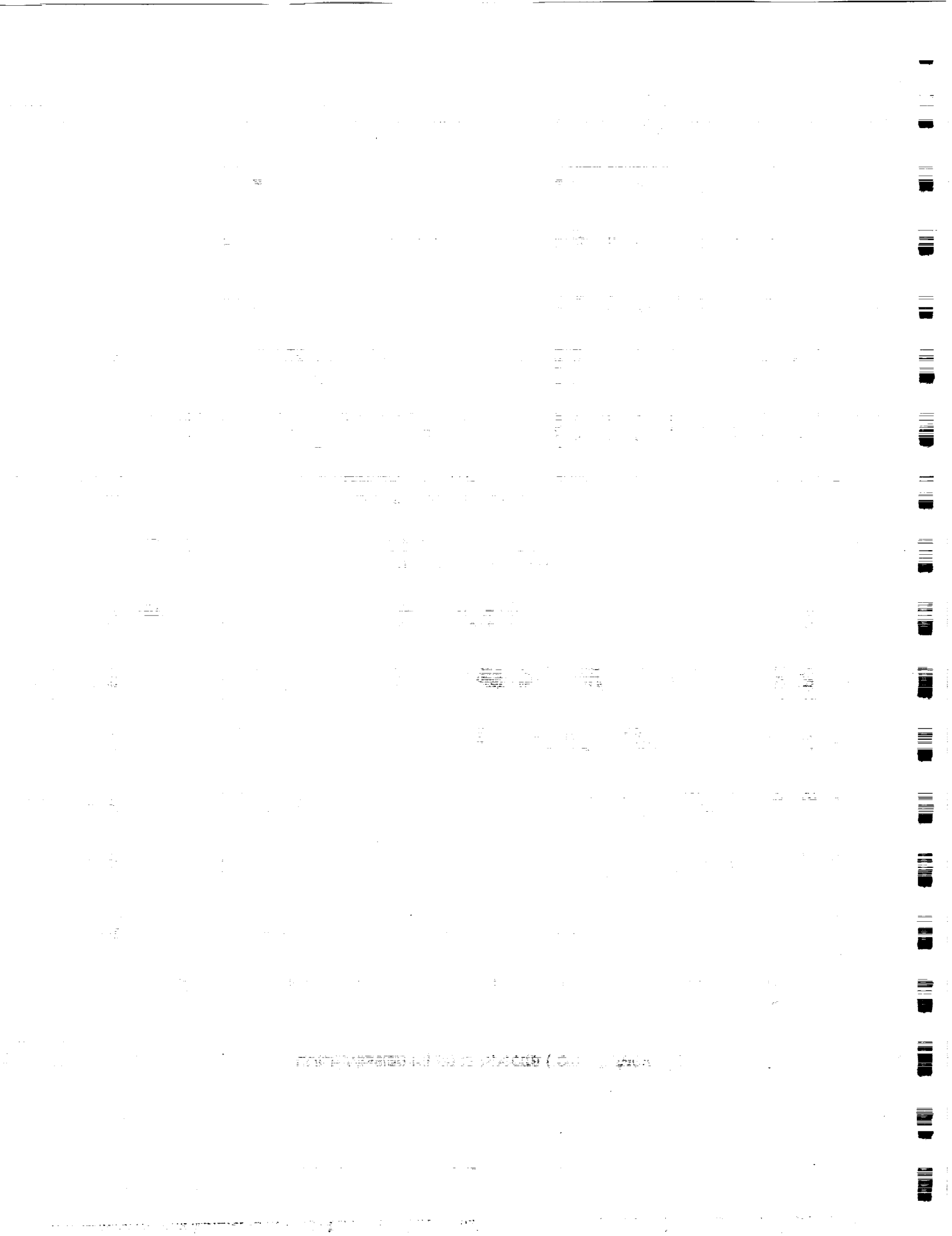


Fig. D-6. Comparison of fluence spectra at a depth of 50 g/cm² in aluminum from LDEF exposure to different ionizing radiation sources.



Appendix E

Additional Dose Results

Figs. D-1 through E-4 compare primary vs. secondary particle contributions to the absorbed dose in tissue for each of the LDEF exposure sources considered.

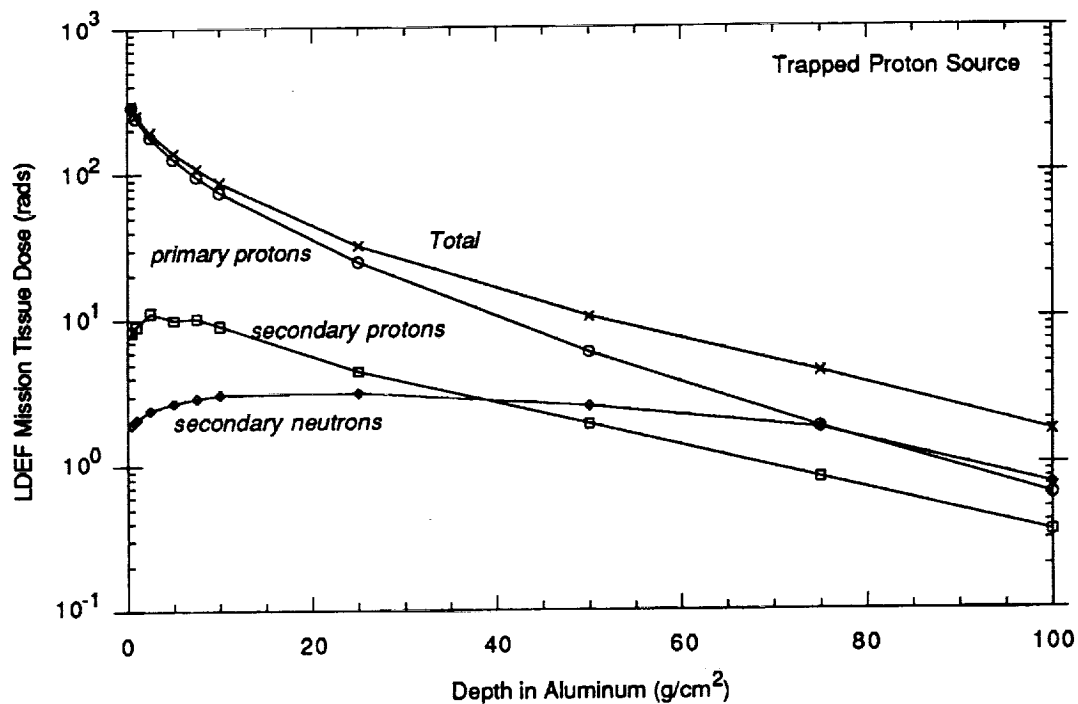


Fig. E-1. Secondary particle contribution to absorbed dose in tissue for trapped proton source.

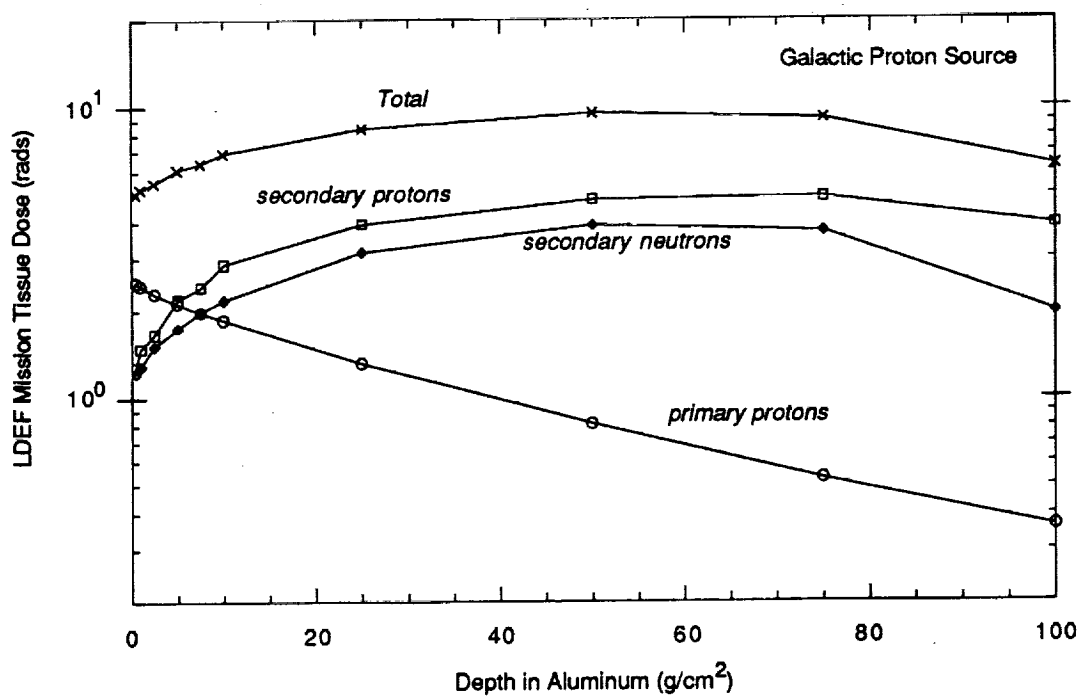


Fig. E-2. Secondary particle contribution to absorbed dose in tissue for galactic proton source.

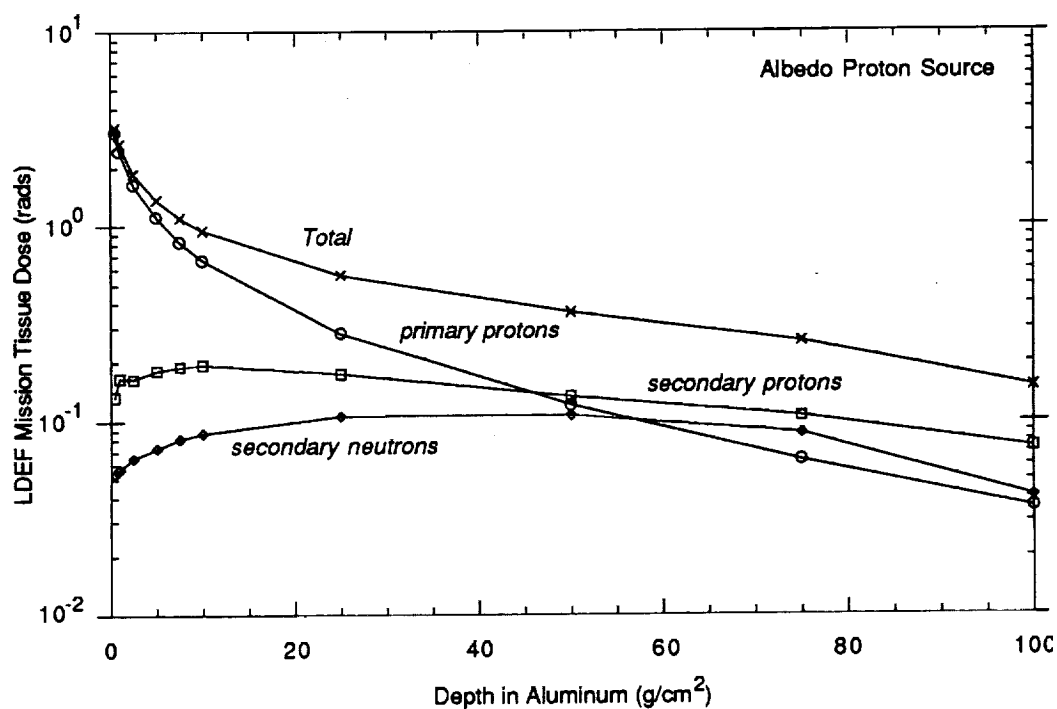


Fig. E-3. Secondary particle contribution to absorbed dose in tissue for albedo proton source.

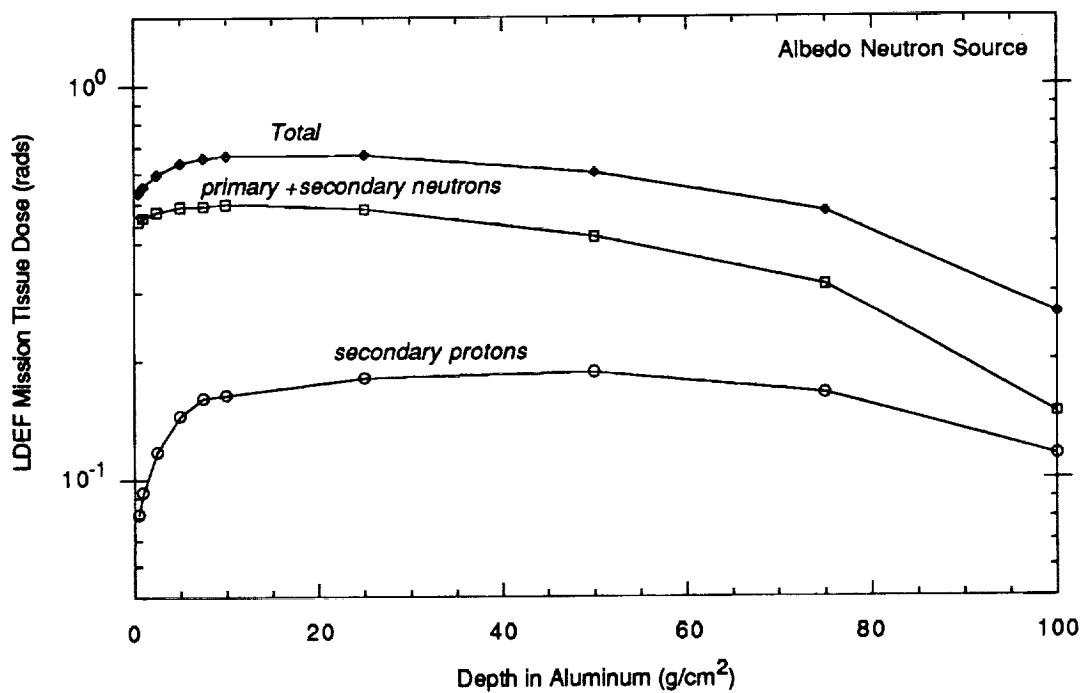


Fig. E-4. Secondary particle contribution to absorbed dose in tissue for albedo neutron source.

Appendix F

Results for Radioisotope Production from Stainless Steel

Induced radioactivity measurements are being made for several LDEF components which are made of stainless steel, and calculated results are given here for several radioisotopes produced in thin stainless steel samples behind varying thicknesses of aluminum shielding. The stainless steel composition used in the calculations (75.3% Fe, 15.4% Cr, and 4.3% Ni, by weight) is based on post-flight x-ray fluorescence measurements (made at MSFC, and provided by A. Harmon, MSFC/SSL) of segments of the LDEF trunion.

Figures F-1 through F-3 compare the contributions from different sources to each of the radioisotopes considered. Figures F-4 through F-8 compare the primary vs. secondary particle contributions to the production of each isotope for trapped proton and galactic sources.

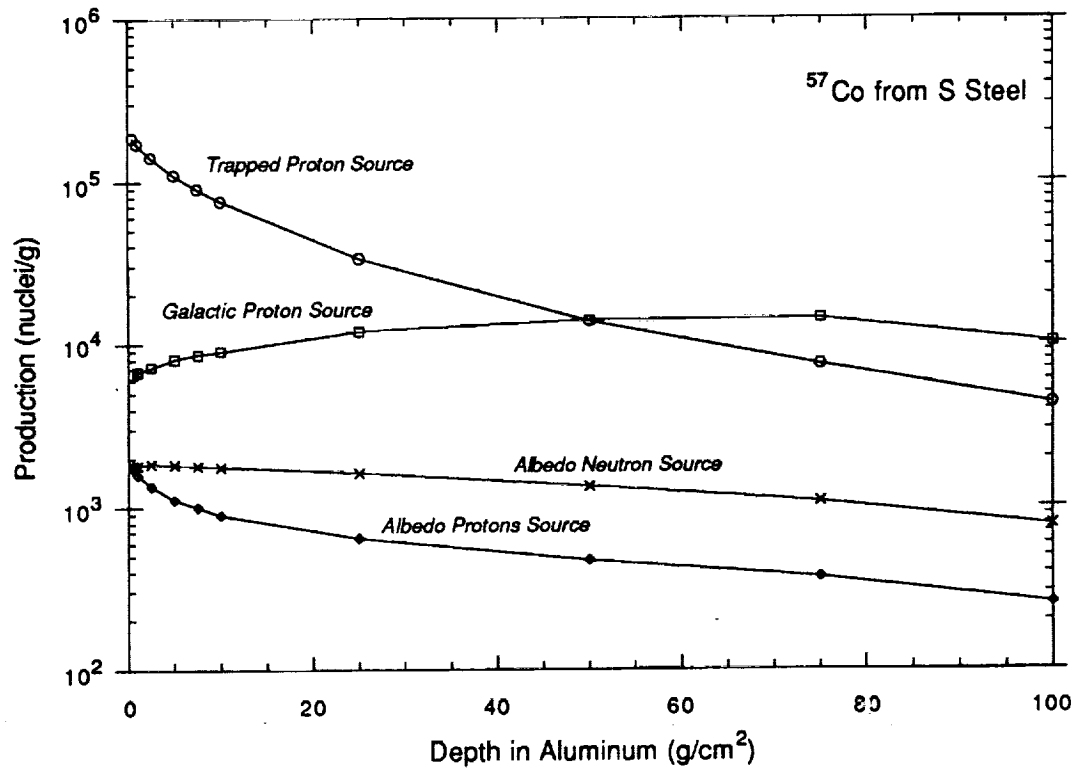
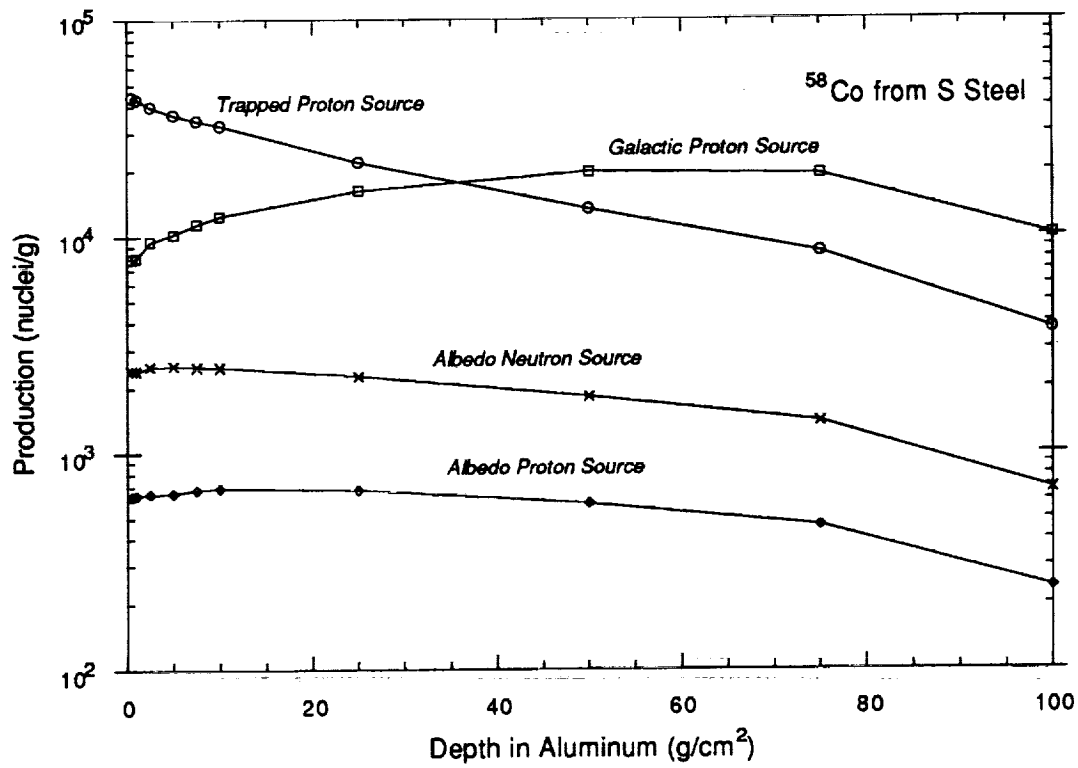


Fig. F-1. Contribution of various space radiation sources to the production of ⁵⁸Co (top graph) and ⁵⁷Co (bottom graph) from stainless steel, normalized for LDEF mission duration.

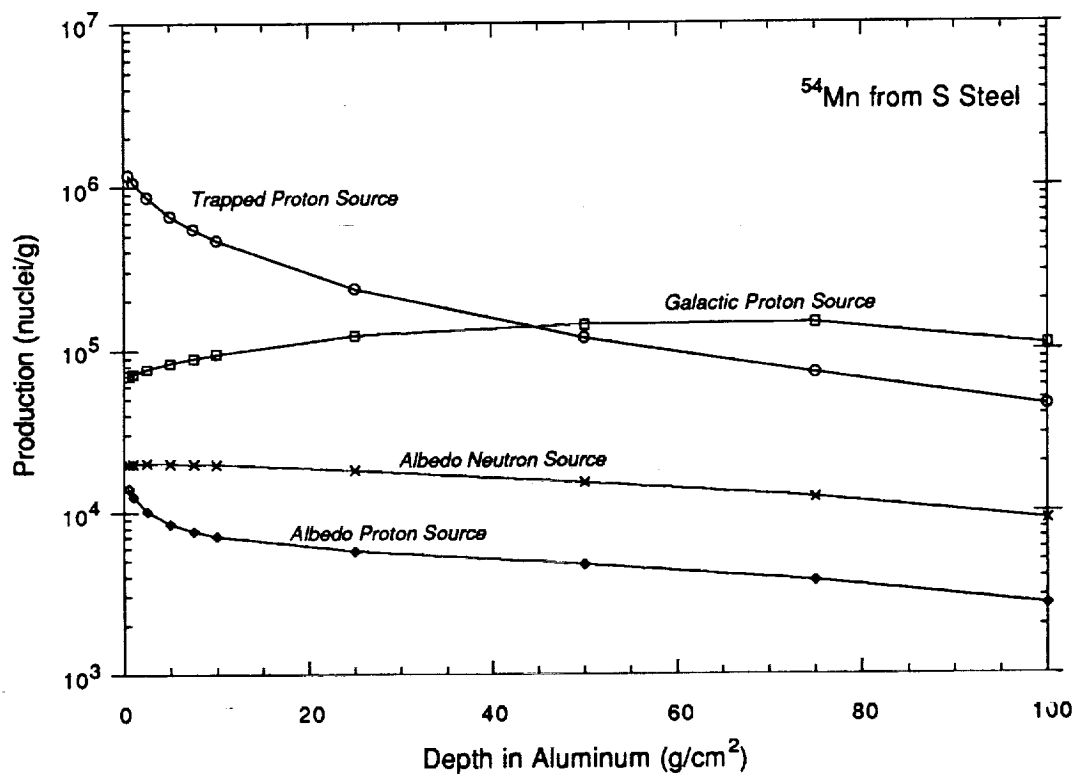
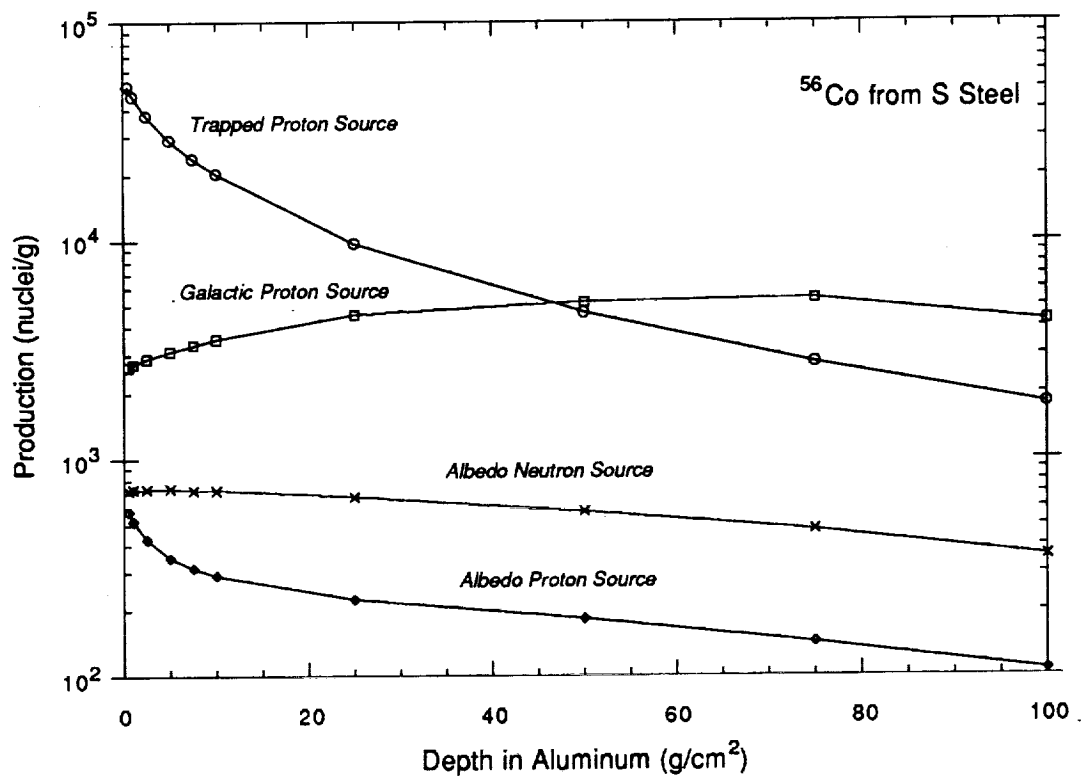


Fig. F-2. Contribution of various space radiation sources to the production of ⁵⁶Co (top graph) and ⁵⁴Mn (bottom graph) from stainless steel, normalized for LDEF mission duration.

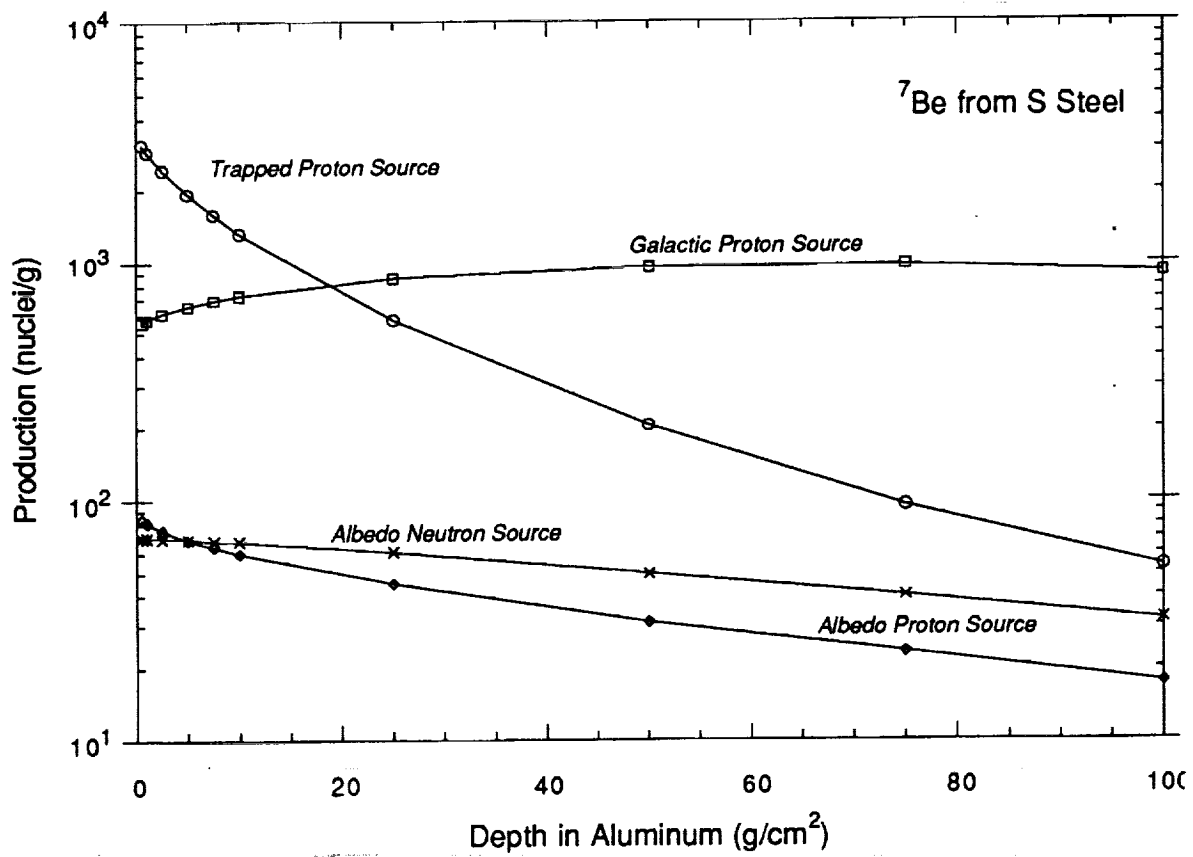


Fig. F-3. Contribution of various space radiation sources to the production of ⁷Be from stainless steel, normalized for LDEF mission duration.

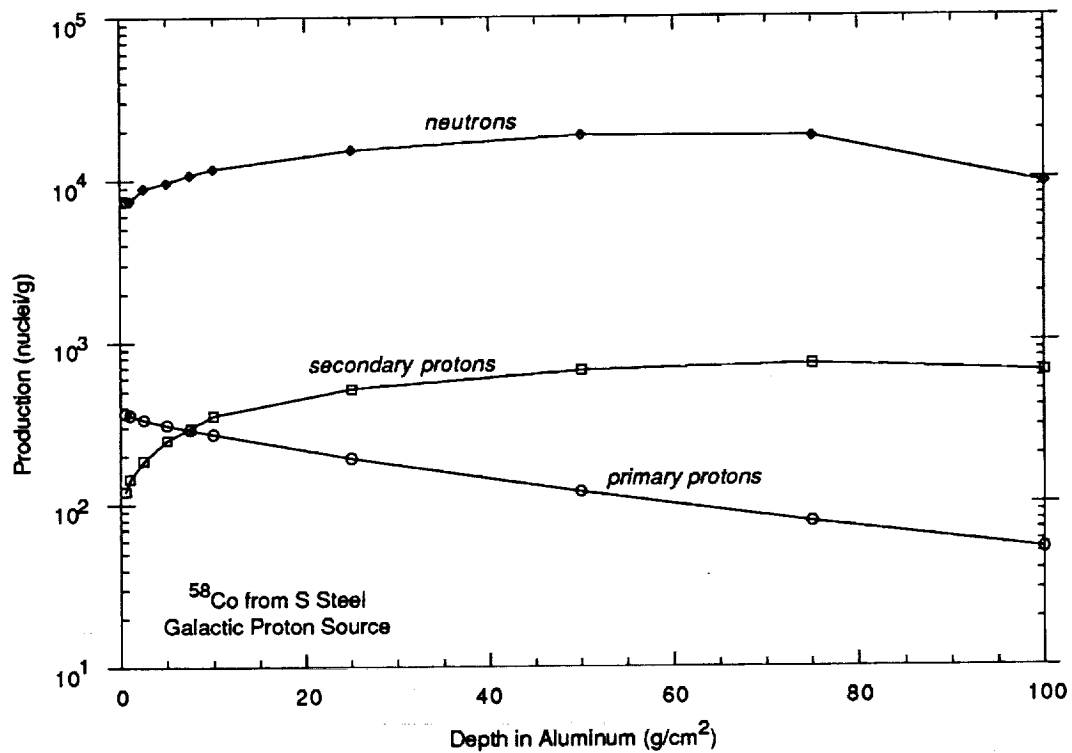
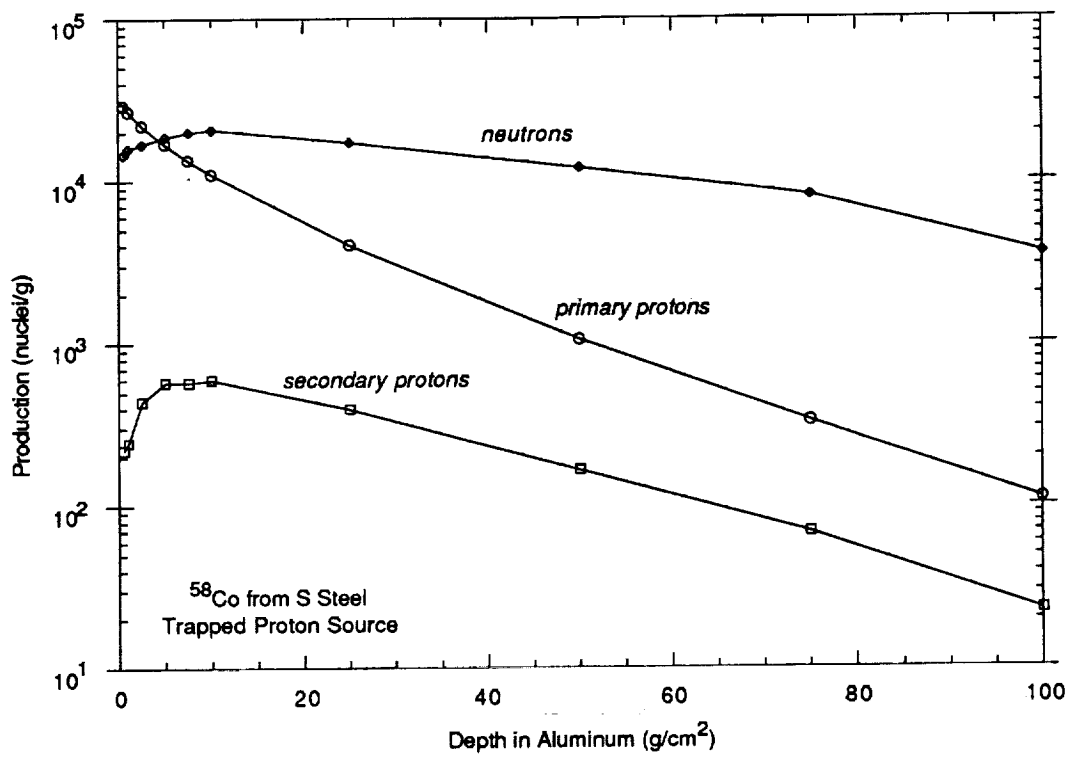


Fig. F-4. Secondary particle contribution to ^{58}Co production from stainless steel by trapped proton (top) and galactic proton (bottom) sources, normalized for LDEF mission duration.

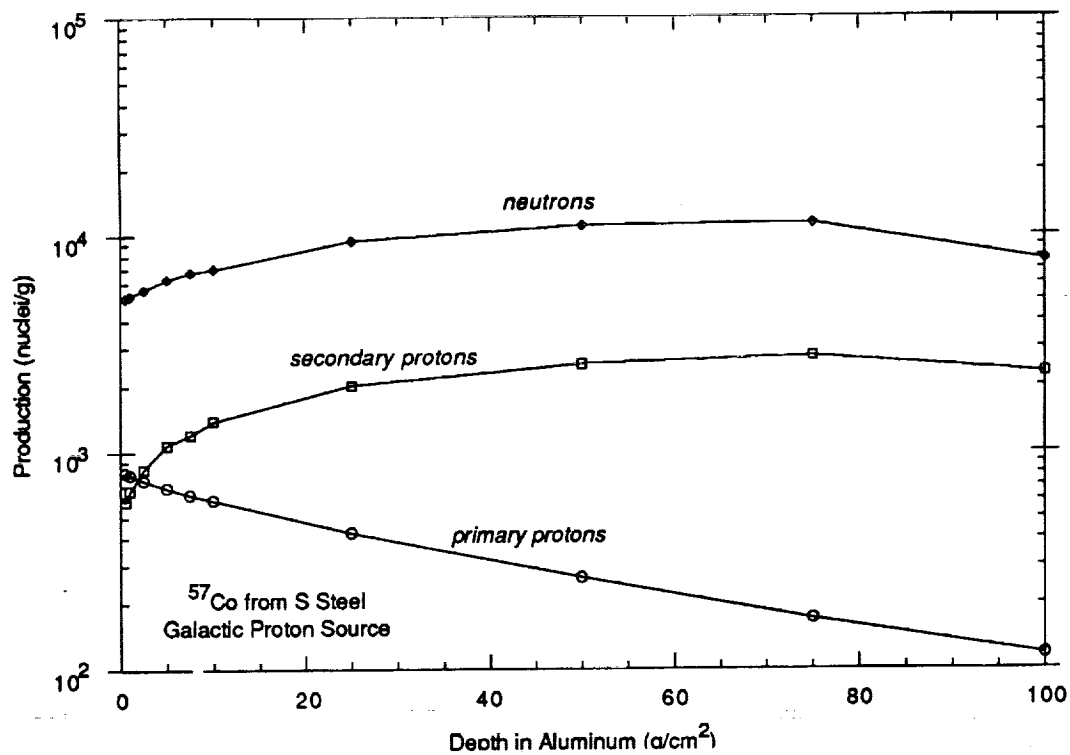
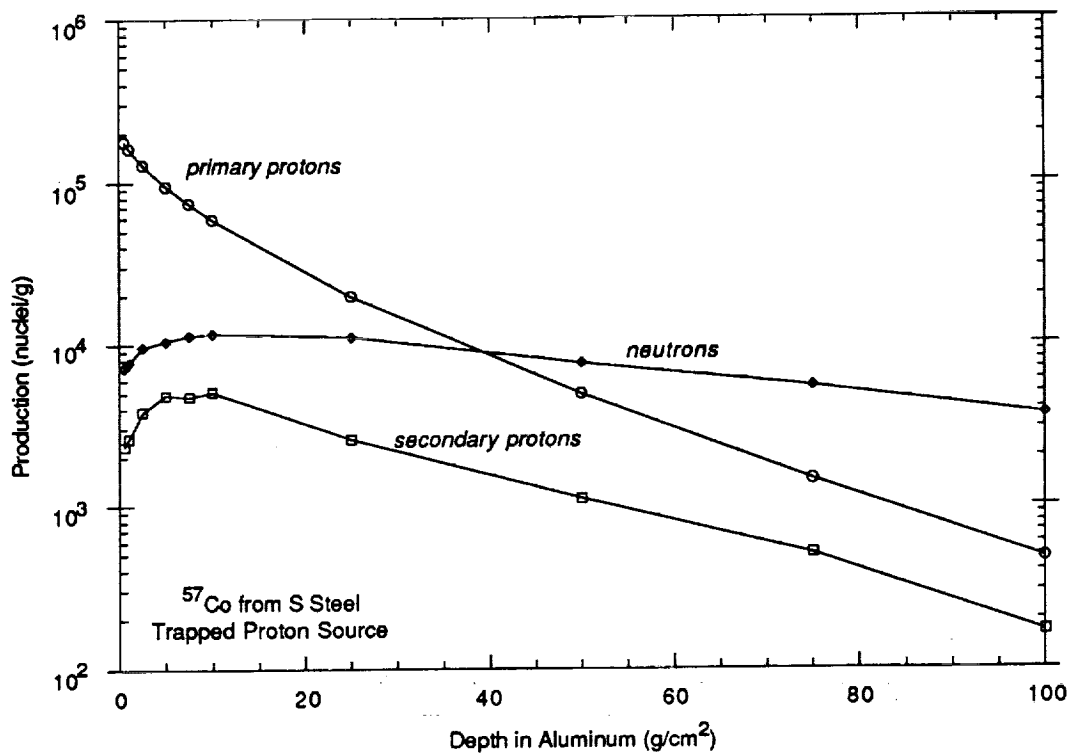


Fig. F-5. Secondary particle contribution to ^{57}Co production from stainless steel by trapped proton (top) and galactic proton (bottom) sources, normalized for LDEF mission duration.

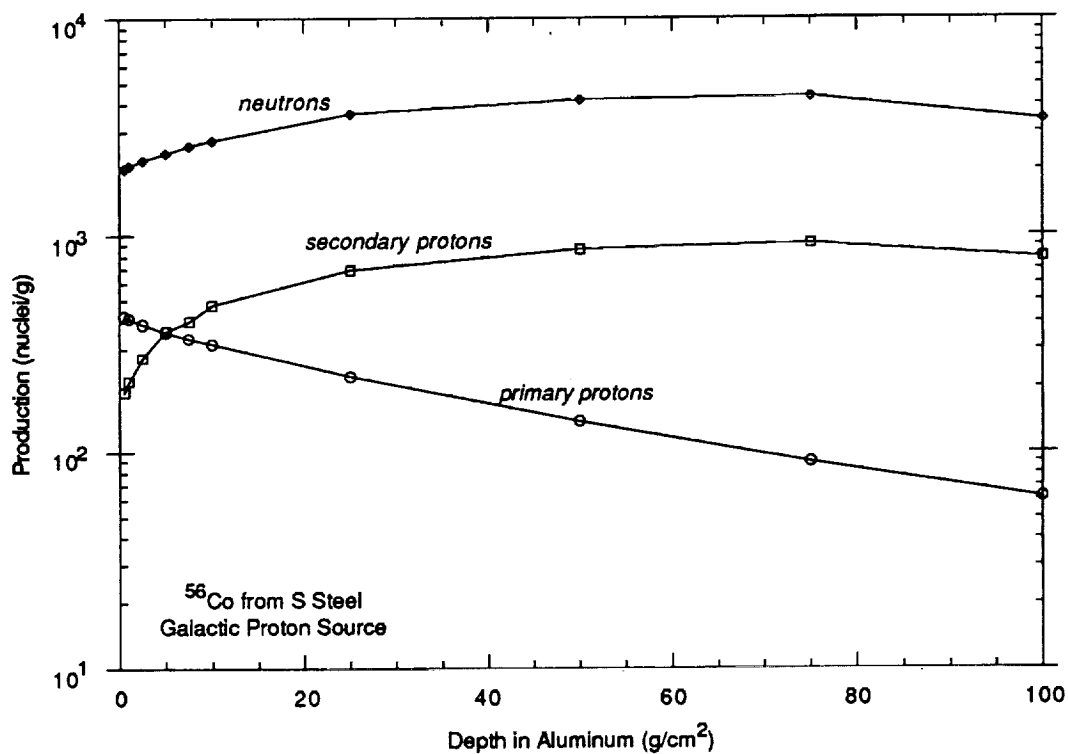
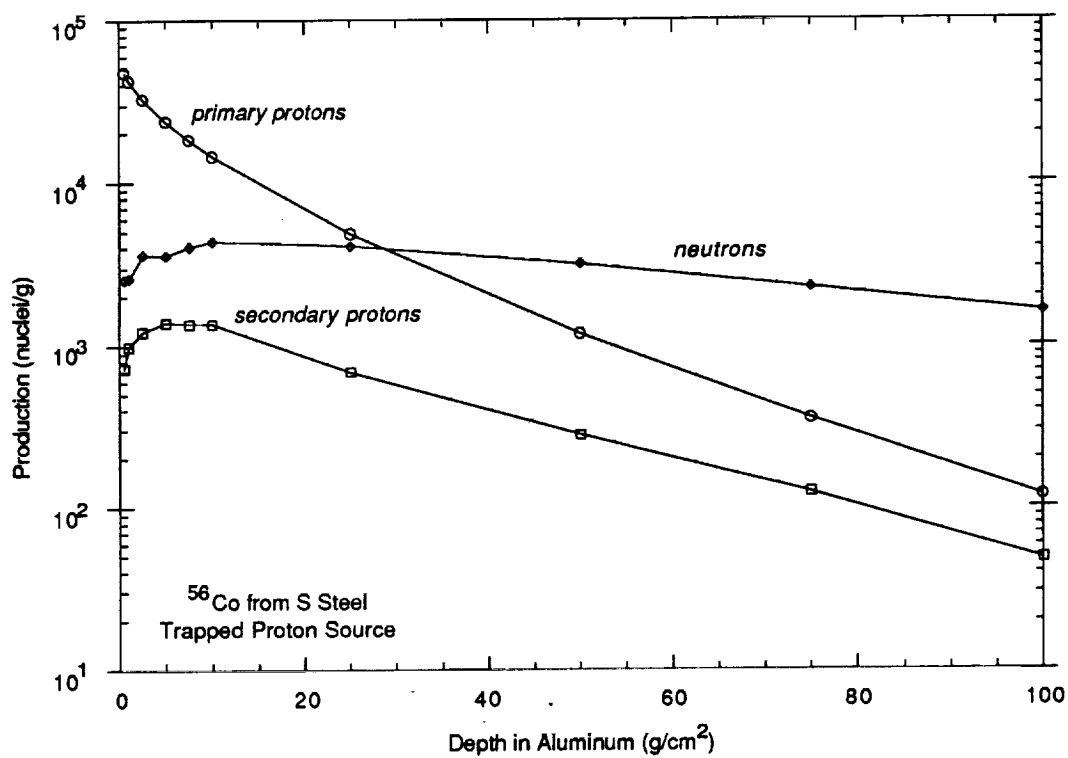


Fig. F-6. Secondary particle contribution to ^{56}Co production from stainless steel by trapped proton (top) and galactic proton (bottom) sources, normalized for LDEF mission duration.

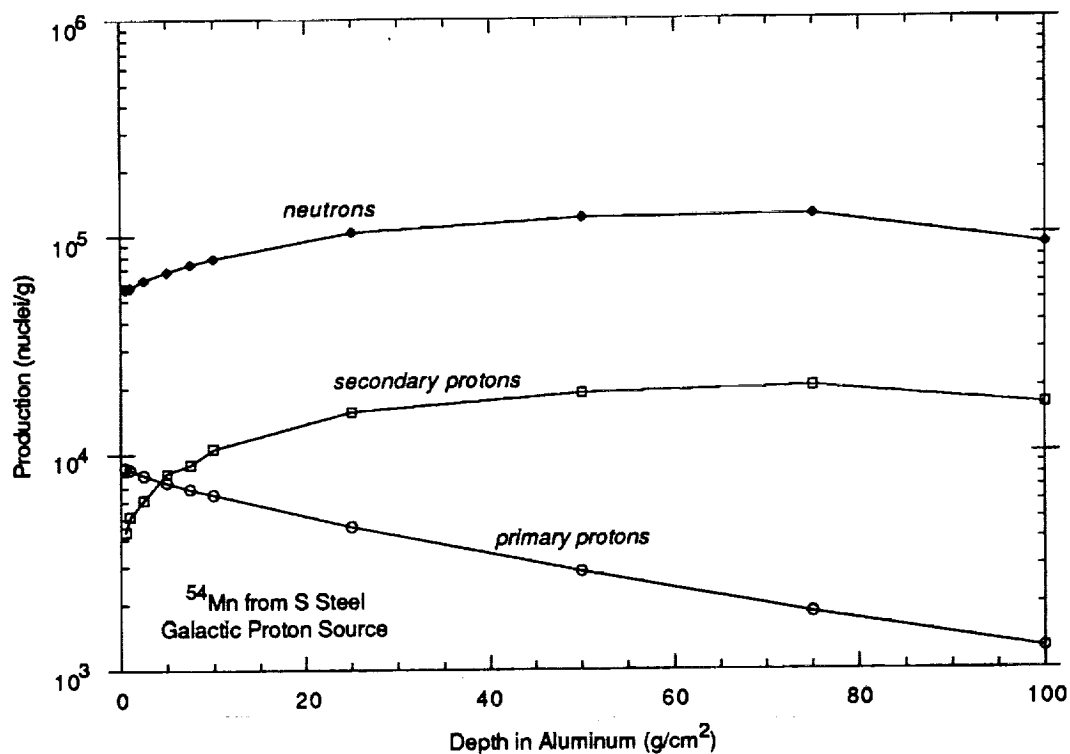
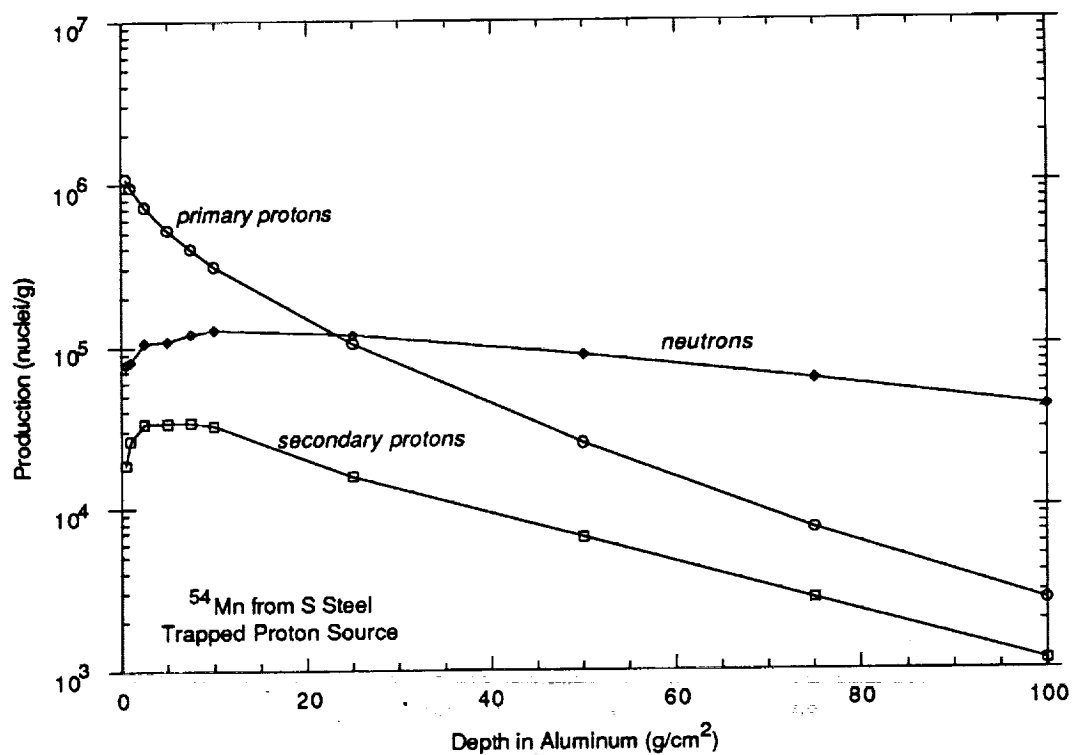


Fig. F-7. Secondary particle contribution to ^{54}Mn production from stainless steel by trapped proton (top) and galactic proton (bottom) sources, normalized for LDEF mission duration.

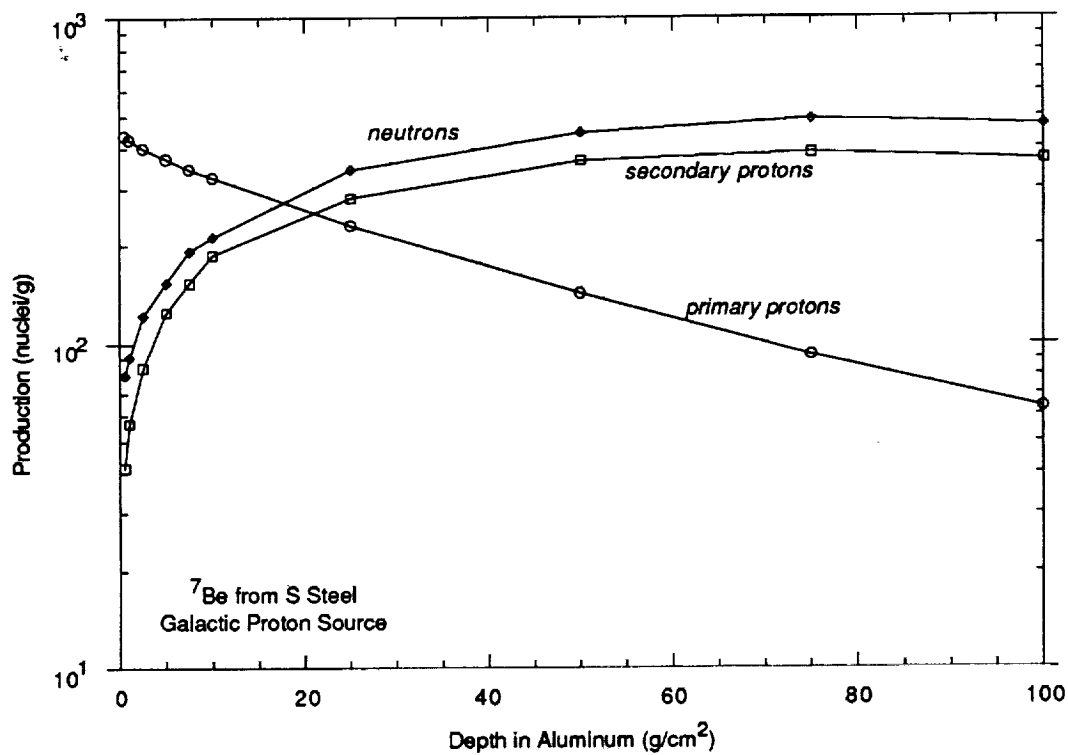
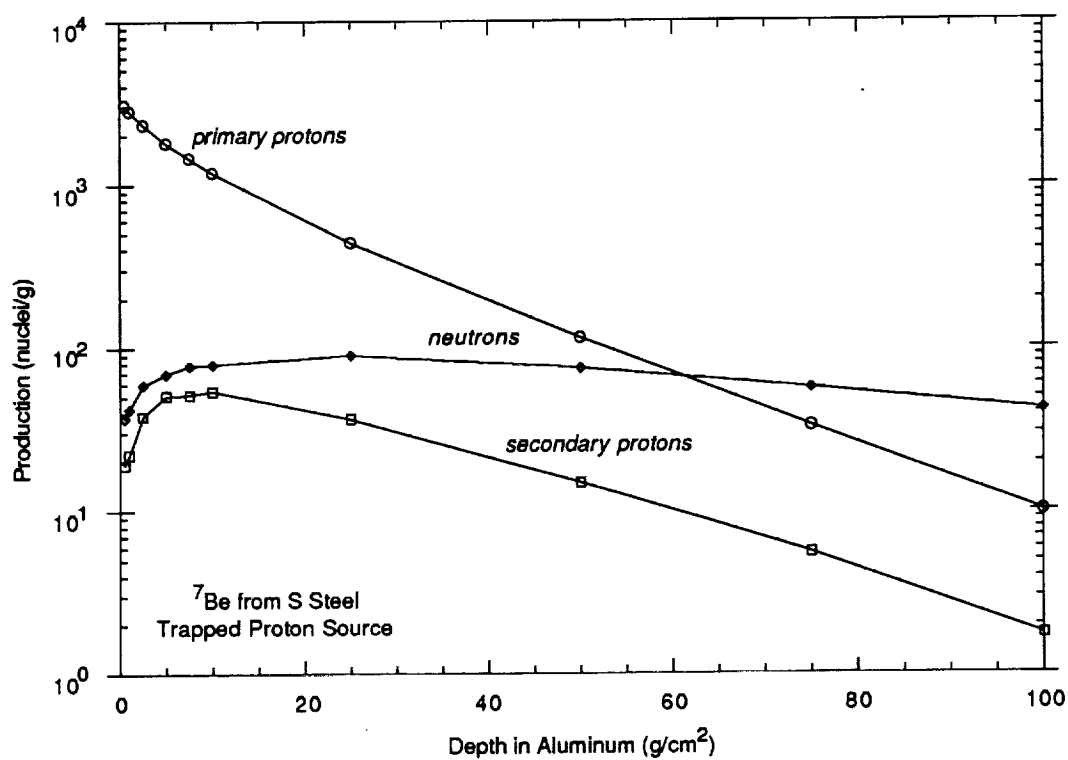


Fig. F-8. Secondary particle contribution to ^7Be production from stainless steel by trapped proton (top) and galactic proton (bottom) sources, normalized for LDEF mission duration.

